

NASA Technical Memorandum 102178

1N-12✓

8223

873

## Parametric Entry Corridors for Lunar/Mars Aerocapture Missions

Lisa Ling, Franco M. Baseggio,  
and Douglas P. Fuhry

April 1991

**NASA**

National Aeronautics and  
Space Administration

(NASA-TM-102178) PARAMETRIC ENTRY CORRIDORS  
FOR LUNAR/MARS AEROCAPTURE MISSIONS (NASA)  
73 p CSCL 22A

N91-21168

Unclas  
G3/12 0008223



100



• **1990** – **1991**

—

— 100 —



6-00000-9

11



▼

NASA Technical Memorandum 102178

Parametric Entry Corridors for Lunar/Mars Aerocapture  
Missions

Lisa Ling  
*Lyndon B. Johnson Space Center*  
*Houston, Texas*

Franco M. Baseggio  
Douglas P. Fuhry  
*The Charles Stark Draper Laboratory, Inc.*  
*Cambridge, Massachusetts*

National Aeronautics and Space Administration  
Lyndon B. Johnson Space Center  
Houston, Texas

April 1991



# CONTENTS

Section		Page
1	<u>INTRODUCTION</u> .....	1-1
2	<u>ENTRY CORRIDOR DEFINITION FOR AEROCAPTURE</u> .....	2-1
2.1	<u>BACKGROUND</u> .....	2-1
2.2	<u>CORRIDOR DETERMINATION</u> .....	2-2
3	<u>PARAMETRIC AEROCAPTURE CORRIDOR RESULTS</u> .....	3-1
3.1	<u>STUDY CONDITIONS</u> .....	3-1
3.2	<u>EARTH AEROCAPTURE CORRIDORS</u> .....	3-3
3.3	<u>MARS AEROCAPTURE CORRIDORS</u> .....	3-6
3.4	<u>EXAMPLES AND DISCUSSION OF DATA UTILIZATION</u> .....	3-6
4	<u>CONCLUSIONS</u> .....	4-1
5	<u>REFERENCES</u> .....	5-1
APPENDIX A	<u>USE OF AEROCAPTURE CORRIDORS AS A CONSTRAINT ON APPROACH NAVIGATION</u> .....	A-1
APPENDIX B	<u>EFFECT OF ADDED CONSTRAINTS ON AEROCAPTURE CORRIDOR WIDTH</u> .....	B-1
APPENDIX C	<u>EFFECT OF VEHICLE BALLISTIC COEFFICIENT ON AEROCAPTURE CORRIDOR WIDTH</u> .....	C-1
APPENDIX D	<u>G-LIMITS FOR ZERO CORRIDOR WIDTHS</u> .....	D-1

## TABLES

Table		Page
3-I	PARAMETER RANGES .....	3-1
3-II	SAMPLED VALUES OF $L/D$ , $V_{\infty}$ , AND $g$ -LOAD LIMIT .....	3-2
4-I	VARIATIONS IN ENTRY CORRIDOR WIDTHS DUE TO INCREASED MISSION CONSTRAINTS AND REQUIREMENTS .....	4-2

## FIGURES

Figure		Page
2-1	Profiles of open-loop aerocapture trajectories for corridor determination	
	(a) Altitude profiles .....	2-4
	(b) Aerodynamic load profiles .....	2-4
2-2	Example plot of corridor data .....	2-5
3-1	Ballistic coefficient versus lift-to-drag .....	3-8
3-2	Earth: $V_{\infty} = 1$ km/s with nominal atmosphere .....	3-9
3-3	Earth: $V_{\infty} = 4$ km/s with nominal atmosphere .....	3-9
3-4	Earth: $V_{\infty} = 7.56$ km/s with nominal atmosphere .....	3-10
3-5	Earth: $V_{\infty} = 10.61$ km/s with nominal atmosphere .....	3-10
3-6	Earth: $V_{\infty} = 14$ km/s with nominal atmosphere .....	3-11
3-7	Earth: $V_{\infty} = 18$ km/s with nominal atmosphere .....	3-11
3-8	Earth: $L/D = 0.1$ with nominal atmosphere .....	3-12
3-9	Earth: $L/D = 0.3$ with nominal atmosphere .....	3-12
3-10	Earth: $L/D = 0.5$ with nominal atmosphere .....	3-13
3-11	Earth: $L/D = 0.7$ with nominal atmosphere .....	3-13
3-12	Earth: $L/D = 1$ with nominal atmosphere .....	3-14
3-13	Earth: $L/D = 2$ with nominal atmosphere .....	3-14
3-14	Earth: $V_{\infty} = 1$ km/s with $\pm 30$ percent atmosphere dispersions .....	3-15
3-15	Earth: $V_{\infty} = 4$ km/s with $\pm 30$ percent atmosphere dispersions .....	3-15
3-16	Earth: $V_{\infty} = 7.56$ km/s with $\pm 30$ percent atmosphere dispersions .....	3-16
3-17	Earth: $V_{\infty} = 10.61$ km/s with $\pm 30$ percent atmosphere dispersions .....	3-16
3-18	Earth: $V_{\infty} = 14$ km/s with $\pm 30$ percent atmosphere dispersions .....	3-17
3-19	Earth: $V_{\infty} = 18$ km/s with $\pm 30$ percent atmosphere dispersions .....	3-17
3-20	Earth: $L/D = 0.1$ with $\pm 30$ percent atmosphere dispersions .....	3-18
3-21	Earth: $L/D = 0.3$ with $\pm 30$ percent atmosphere dispersions .....	3-18
3-22	Earth: $L/D = 0.5$ with $\pm 30$ percent atmosphere dispersions .....	3-19
3-23	Earth: $L/D = 0.7$ with $\pm 30$ percent atmosphere dispersions .....	3-19
3-24	Earth: $L/D = 1$ with $\pm 30$ percent atmosphere dispersions .....	3-20
3-25	Earth: $L/D = 2$ with $\pm 30$ percent atmosphere dispersions .....	3-20
3-26	Earth: Vacuum periapse corridor width to EI flight path angle corridor width conversion chart .....	3-21
3-27	Mars: $V_{\infty} = 2$ km/s with nominal atmosphere .....	3-22
3-28	Mars: $V_{\infty} = 4.71$ km/s with nominal atmosphere .....	3-22
3-29	Mars: $V_{\infty} = 6.97$ km/s with nominal atmosphere .....	3-23
3-30	Mars: $V_{\infty} = 10$ km/s with nominal atmosphere .....	3-23
3-31	Mars: $V_{\infty} = 12$ km/s with nominal atmosphere .....	3-24
3-32	Mars: $L/D = 0.1$ with nominal atmosphere .....	3-24
3-33	Mars: $L/D = 0.5$ with nominal atmosphere .....	3-25
3-34	Mars: $L/D = 1.0$ with nominal atmosphere .....	3-25
3-35	Mars: $L/D = 1.5$ with nominal atmosphere .....	3-26
3-36	Mars: $L/D = 2.0$ with nominal atmosphere .....	3-26
3-37	Mars: $V_{\infty} = 2$ km/s with + 100 percent and -50 percent atmosphere dispersions .....	3-27
3-38	Mars: $V_{\infty} = 4.71$ km/s with + 100 percent and -50 percent atmosphere dispersions .....	3-27

Figure		Page
3-39	Mars: $V_{\infty} = 6.97$ km/s with +100 percent and -50 percent atmosphere dispersions	3-28
3-40	Mars: $V_{\infty} = 10$ km/s with +100 percent and -50 percent atmosphere dispersions	3-28
3-41	Mars: $V_{\infty} = 12$ km/s with +100 percent and -50 percent atmosphere dispersions	3-29
3-42	Mars: $L/D = 0.1$ with +100 percent and -50 percent atmosphere dispersions	3-29
3-43	Mars: $L/D = 0.5$ with +100 percent and -50 percent atmosphere dispersions	3-30
3-44	Mars: $L/D = 1.0$ with +100 percent and -50 percent atmosphere dispersions	3-30
3-45	Mars: $L/D = 1.5$ with +100 percent and -50 percent atmosphere dispersions	3-31
3-46	Mars: $L/D = 2.0$ with +100 percent and -50 percent atmosphere dispersions	3-31
3-47	Mars: Vacuum periapse corridor width to EI flight path angle corridor width conversion chart	3-32
A-1	Optical navigation performance at EI (3 $\sigma$ ) measurements suspended 1 hour prior to EI	A-3
A-2	Examples of Mars approach navigation performance	A-4
B-1	Earth: Maximum convective heating rate for $V_{\infty} = 1$ km/s	B-4
B-2	Earth: Maximum convective heating rate for $V_{\infty} = 4$ km/s	B-4
B-3	Earth: Maximum convective heating rate for $V_{\infty} = 7.56$ km/s	B-5
B-4	Earth: Maximum convective heating rate for $V_{\infty} = 10.61$ km/s	B-5
B-5	Earth: Maximum convective heating rate for $V_{\infty} = 14$ km/s	B-6
B-6	Earth: Maximum convective heating rate for $V_{\infty} = 18$ km/s	B-6
B-7	Mars: Maximum convective heating rate for $V_{\infty} = 2$ km/s	B-7
B-8	Mars: Maximum convective heating rate for $V_{\infty} = 4.71$ km/s	B-7
B-9	Mars: Maximum convective heating rate for $V_{\infty} = 6.97$ km/s	B-8
B-10	Mars: Maximum convective heating rate for $V_{\infty} = 10$ km/s	B-8
B-11	Mars: Maximum convective heating rate for $V_{\infty} = 12$ km/s	B-9
B-12	Earth: Apsidal rotation for $V_{\infty} = 7.56$ km/s	B-9
B-13	Mars: Apsidal rotation for $V_{\infty} = 10$ km/s	B-10
C-1	Earth: Ballistic coefficient sensitivity with $V_{\infty} = 7.56$ km/s	C-2
D-1	Earth: g-limits for 0° corridors at $V_{\infty} = 1$ km/s	D-2
D-2	Earth: g-limits for 0° corridors at $V_{\infty} = 4$ km/s	D-2
D-3	Earth: g-limits for 0° corridors at $V_{\infty} = 7.56$ km/s	D-3
D-4	Earth: g-limits for 0° corridors at $V_{\infty} = 10.61$ km/s	D-3
D-5	Earth: g-limits for 0° corridors at $V_{\infty} = 14$ km/s	D-4
D-6	Earth: g-limits for 0° corridors at $V_{\infty} = 18$ km/s	D-4
D-7	Mars: g-limits for 0° corridors at $V_{\infty} = 2$ km/s	D-5
D-8	Mars: g-limits for 0° corridors at $V_{\infty} = 4.71$ km/s	D-5
D-9	Mars: g-limits for 0° corridors at $V_{\infty} = 6.97$ km/s	D-6
D-10	Mars: g-limits for 0° corridors at $V_{\infty} = 10$ km/s	D-6
D-11	Mars: g-limits for 0° corridors at $V_{\infty} = 12$ km/s	D-7



## ACRONYMS AND SYMBOLS

AFE	Aeroassist Flight Experiment
$C_B$	ballistic coefficient
$C_D$	drag coefficient
COSPAR	[International] Committee on Space Research
DSN	Deep Space Network
EI	entry interface
$g$	load factor
$g_0$	Earth gravitational acceleration
HEI	Human Exploration Initiative
JSC	Lyndon B. Johnson Space Center
L/D	lift-to-drag ratio
LMSC	Lockheed Missiles and Space Company, Inc.
MEV	Mars Excursion Vehicle
MMC	Martin Marietta Company
MRSR	Mars Rover Sample Return
MTV	Mars Transfer Vehicle
$V_\infty$	hyperbolic excess velocity



## SECTION 1 INTRODUCTION

The current NASA Human Exploration Initiative (HEI) environment has spawned many proposals for missions involving aerocapture into both Earth and Mars orbits. Aerocapture is sometimes seen as the cure-all for high launch mass ailments due to its potential for large reductions in required planetary capture orbit injection propellant. However, improper design or overly optimistic assumptions can lead to misunderstandings concerning the range of missions over which aerocapture is indeed possible. In addition, it can be difficult to get a handle on vehicle performance requirements for satisfaction of key aerocapture mission requirements and constraints. These difficulties point to the desirability of a consistent set of guidelines which lends insight not only into whether aerocapture is feasible in a given mission design, but also into the trade-offs possible between mission and vehicle design parameters and constraints.

It has long been realized that atmospheric entry corridors can be used to bound acceptable planetary approach trajectory ranges for aerocapture subject to various constraints. This report presents parametric atmospheric entry corridor data for Earth and Mars aerocapture. Parameter ranges for this study were dictated by the range of mission designs currently envisioned as possibilities for HEI. These data, while not providing a means for exhaustive evaluation of aerocapture performance, should prove to be a useful aid to preliminary mission design and evaluation.

Entry corridors are expressed as ranges of allowable vacuum periapse altitude of the planetary approach hyperbolic orbit, with charts provided for conversion to an approximate flight path angle corridor at entry interface (EI) (125 km altitude). The corridor boundaries are defined by open-loop aerocapture trajectories which satisfy boundary constraints while utilizing the full aerodynamic control capability of the vehicle (i.e., full lift-up or full lift-down); thus, the corridor essentially defines the physical limitations of a given vehicle design and does not include the effects of a specific aerocapture guidance algorithm. Parameters examined were limited to those of greatest importance from an aerocapture trajectory performance standpoint, including the approach orbit hyperbolic excess velocity ( $V_{\infty}$ ), the vehicle lift-to-drag ratio ( $L/D$ ), the maximum aerodynamic load factor limit, and the apoapse of the target orbit. The impact of atmospheric density bias uncertainties is also included.

The corridor data are presented in graphical form, and examples of the utilization of these graphs for mission design and evaluation are included.



## SECTION 2

### ENTRY CORRIDOR DEFINITION FOR AEROCAPTURE

#### 2.1 BACKGROUND

In the absence of uncertainties and dispersions, the flyability of a given planetary approach trajectory for aerocapture can be determined by a single parameter - the vacuum periapse altitude (or, equivalently, the flight path angle at a given altitude prior to atmospheric entry). For unguided ballistic trajectories, this parameter essentially determines the depth of atmospheric penetration for a given vehicle and, therefore, the aerodynamic loads and total energy depletion which will occur during the aeropass. A corridor of acceptable approach periapse altitudes can be determined by bounding the range over which trajectory constraints will not be violated. These constraints may include a maximum aerodynamic loading limit, maximum heat rate, minimum penetration altitude, or skipout avoidance. The total corridor width can be thought of as the amount of margin which is available to handle dispersions in the approach periapse altitude.

For this study, the aerocapture vehicle is defined parametrically by two quantities, the lift-to-drag ratio ( $L/D$ ) and ballistic coefficient ( $C_B$ ). The  $C_B$  is defined as

$$C_B = \frac{m}{C_D A_{ref}}$$

where  $m$  is the vehicle mass,  $C_D$  the drag coefficient, and  $A_{ref}$  the aerodynamic reference area. Given a lifting vehicle, the atmospheric trajectory can be modified by modulating the lift vector about the atmosphere-relative velocity vector. The impact of maximum control inputs (i.e., full lift-up or full lift-down trajectories) can be incorporated into the vacuum periapse corridor boundaries with the goal of bounding the physical performance capability of the vehicle. This is done with the realization that guided trajectories will be limited to control inputs lying in the range from lift-up to lift-down.

Parametric entry corridor data can be very useful in preliminary design of missions involving aerocapture in several ways. First of all, such data can provide mission designers with a rough idea of what vehicle performance capability (i.e.,  $L/D$ ) will be required for aerocapture from a given interplanetary trajectory. Since the vehicle weight and complexity (and, hence, cost) tend to increase with  $L/D$ , it is useful to be able to predict the minimum value necessary to satisfy preliminary mission requirements. Secondly, these data provide quick insight into design trade-offs between such factors as  $L/D$ , atmospheric entry speed, acceptable levels of atmospheric density knowledge uncertainties, and constraints (such as acceptable g-load levels). Since many mission requirements and design parameters are highly interdependent, comprehensive data showing the relationships between the important ones will provide insight into possible design compromises for total cost reduction. Thirdly, a convenient method for performing rough feasibility checks of proposed missions is provided.

While the parametric entry corridor data presented here are useful in preliminary mission design and evaluation, they are by no means exhaustive in determining aerocapture performance for a given mission. Aerocapture performance is also significantly impacted by many other factors, including the performance of onboard closed-loop guidance and navigation during the aeropass, navigated state vector uncertainties, and dynamic atmospheric density dispersions. In addition, these corridors only include a single final orbital constraint, the apoapse altitude. Additional target constraints, such as the orientation of the final orbit plane (longitude of the ascending node and inclination) or the final orientation of the orbital line-of-apsides, will add to the trajectory control

capability (i.e., L/D) required. While it is impossible to examine all factors in detail for preliminary mission design, the qualitative impact of many of these factors is well understood. The impact of navigation errors, which will be of greater concern for Mars aerocapture, is discussed in further detail in appendix A, and the impact of additional trajectory constraints is discussed qualitatively in appendix B.

## 2.2 CORRIDOR DETERMINATION

The primary constraints used in the definition of the aerocapture corridor in this study are skipout (upper or shallow corridor boundary) and the maximum allowable aerodynamic load factor (lower or steep corridor boundary). The aerodynamic load factor is defined as

$$g_{\oplus} = \frac{|a_{aero}|}{g_{0\oplus}}$$

where:  $a_{aero}$  is the aerodynamic acceleration vector

$g_{0\oplus} = 9.8066 \text{ m/s}^2$  is the reference sea level Earth gravitational acceleration

Skipout is defined to occur when the atmospheric exit orbit is hyperbolic or elliptic with an apoapse that is higher than the target value. As was mentioned previously, the intent here is to bound the physical performance limitations of the vehicle; thus, the lower bound of the entry corridor is defined using a full lift-up trajectory (since a guided steep trajectory would be flown lift-up until the peak loading point is passed in order to provide the highest level of load relief) and the upper bound using a full lift-down trajectory (since a guided shallow trajectory would be flown lift-down in order to increase atmospheric penetration depth). Figure 2-1(a) illustrates example altitude profiles for two open-loop aerocapture trajectories corresponding to these constraints. Figure 2-1(b) shows the corresponding aerodynamic load profiles over these trajectories. (Note the definite peak in aerodynamic loading which occurs during the aeropass. This is a general characteristic of single-pass aerobraking trajectories.) The "lift-down/skipout" trajectory in figure 2-1(a) corresponds to the approach vacuum periapse altitude above which the vehicle will skip out even if a full lift-down control profile is flown. The "lift-up/max g-load" trajectory corresponds to the approach vacuum periapse altitude below which the maximum allowable g-load will be exceeded even if a full lift-up control profile is flown up to the peak loading point. It is the difference in periapse altitude for these two trajectories (lift-up/max g-load and lift-down/skipout) that defines the corridor width for a given L/D and entry speed. The maximum allowable g-load is one of the parameters varied in this analysis.

The minimum value of the g-load limit for a lift-up trajectory is constrained by the energy depletion requirement over the aeropass. The ultimate purpose of aerocapture is to provide sufficient energy reduction to allow capture into a closed planetary orbit. If a lift-up profile is flown on a steep trajectory in order to provide maximum load relief (as is done here in the definition of the lower corridor boundary), then the vehicle must have the capability to generate enough downward lift after peak aerodynamic loading (that is, after active control of aerodynamic loading is no longer necessary) to counteract the centrifugal force and allow sufficient energy depletion for capture. If the peak g-load is too low, then the vehicle will not have enough downward lift capability to prevent skipout. Thus, a trajectory flown with full lift-up between entry and peak aerodynamic loading with an immediate switch to lift-down after peak loading will indicate whether sufficient lift capability exists. The limiting case (i.e., the minimum value of the g-load limit) will occur at the steepest trajectory above which such a control profile results in atmospheric skipout. In effect, this trajectory defines the minimum corridor width for the particular corridor definition used in this study. An

example of such a limiting trajectory is shown in figure 2-1(a), with the corresponding aerodynamic load profile shown in figure 2-1(b). If the approach periapse altitude of the lift-up/ max g-load trajectory is lower than this limiting value, then the vehicle has enough lifting capability to successfully capture from the full lift-up trajectory.

In addition to the constraint on minimum g-load limit, a constraint on the minimum apoapse altitude of the final post-aeropass orbit is also included. This is roughly a constraint on the amount of energy removed from the orbit during the aeropass, and reflects the desire to ensure that the final apoapse is not significantly lower than the target, thereby resulting in a large post-aeropass propulsive maneuver requirement for correction. This constraint is implemented parametrically by including extreme low and high values of potential target orbits at Earth and Mars. For Mars aerocapture trajectories, the effect of a minimum altitude limit of 25 km for terrain avoidance is also included. Note that these additional constraints effectively apply only to the steep corridor boundary.

Figure 2-2 provides an example of how corridor widths and corridor constraints are plotted in this report as functions of  $L/D$  and  $V_{\infty}$ . Each solid line on this figure provides the corridor width for a given maximum g-load constraint. The corridor width is defined as the difference in the entry ballistic periapse altitudes between a full lift-down shallow trajectory that achieves an apoapse lower than or equal to the target value, and a full lift-up steep trajectory that achieves the desired maximum g-load constraint. The dotted line in the example figure defines the lift-up/lift-down skipout trajectory which constrains the minimum allowable value for the g-load limit at full lift-up till peak loading. At each point along this curve a trajectory will be defined that just skips out (i.e., beyond the target apoapse) and is lift-up till peak g-loading followed by lift-down until exit. Therefore, in this report, all portions of the solid lines falling below the lift-up/lift-down skipout trajectory curve will be removed since, from the above discussion, the deleted data corresponds to uncontrollable skipout cases for full lift-up trajectories. The dashed lines in figure 2-2 are used to define the lift-up apoapse constraints, which constrain the maximum allowable value for the g-load limit on the lift-up steep corridor boundary. Each vehicle along these lines just achieves the apoapse constraint on a lift-up trajectory. Therefore, although the g-loads must vary along each dashed apoapse constraint curve, the intersection of a dashed line and a solid corridor definition line indicates that the given  $L/D$ , g-load limit, and entry speed will achieve the target apoapse on a full lift-up trajectory. If a solid line were between the two dashed apoapse constraint lines, then the lift-up trajectory will achieve an apoapse between the two apoapse limits. Therefore, a dashed apoapse line serves as a boundary between full lift-up trajectories that exit above and below the target apoapse condition. The dashed-dotted line seen on the plots for Mars aerocapture is the 25-km minimum altitude constraint curve. Any solid line or portion of a solid line appearing above this curve corresponds to a case where the aerobraking vehicle will violate the 25-km minimum altitude constraint during the full lift-up steep side corridor aeropass.

All corridor boundaries in this study were found to the nearest kilometer in approach periapse altitude. All constraint boundaries are shown in the graphical results in order to show the relative impact of each individual constraint on corridor width and provide an indication of corridor sensitivity to changing constraints.

National Aeronautics and  
Space Administration

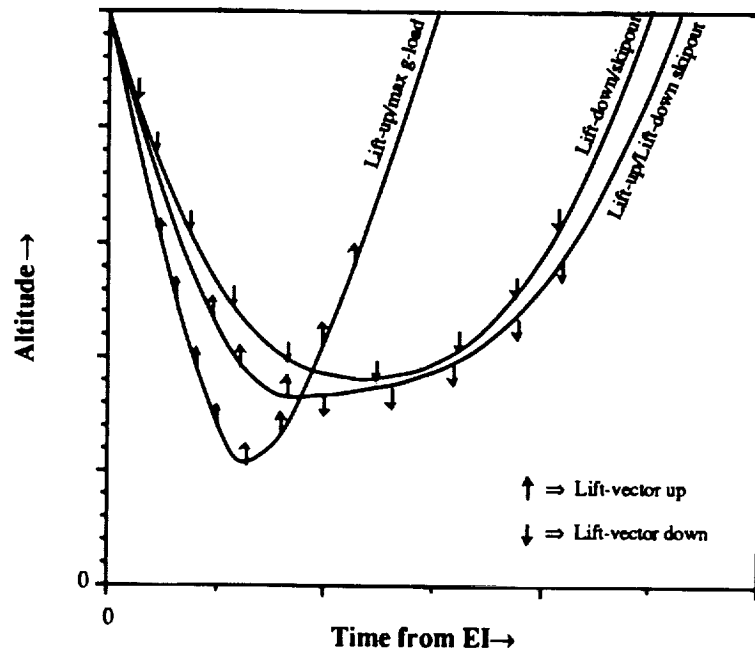
## REPORT DOCUMENTATION PAGE

1. Report No. TM102178	2. Government Accession No.	3. Recipient's Catalog No.	
4. Title and Subtitle  Parametric Entry Corridors for Lunar/Mars Aerocapture Missions		5. Report Date January 22, 1991	
7. Author(s) Lisa M. Ling Franco M. Baseggio * Douglas P. Fuhry *		6. Performing Organization Code ET4	
9. Performing Organization Name and Address  NASA/Johnson Space Center ET4/Performance Analysis Branch Houston, TX 77058		8. Performing Organization Report No. S-628	
12. Sponsoring Agency Name and Address  NASA/Johnson Space Center ET4/Performance Analysis Branch Houston, TX 77058		10. Work Unit No.	
		11. Contract or Grant No.	
		13. Type of Report and Period Covered Technical Memorandum	
		14. Sponsoring Agency Code	
15. Supplementary Notes  * Charles Stark Draper Laboratory, Inc.			
16. Abstract This report presents parametric atmospheric entry corridor data for Earth and Mars aerocapture. Parameter ranges for this study were dictated by the range of mission designs currently envisioned as possibilities for the Human Exploration Initiative (HEI). This data, while not providing a means for exhaustive evaluation of aerocapture performance, should prove to be a useful aid for preliminary mission design and evaluation. Entry corridors are expressed as ranges of allowable vacuum periapse altitude of the planetary approach hyperbolic orbit, with charts provided for conversion to an approximate flight path angle corridor at entry interface (EI, 125 km altitude). The corridor boundaries are defined by open-loop aerocapture trajectories which satisfy boundary constraints while utilizing the full aerodynamic control capability of the vehicle (i.e., full lift-up or full lift-down). Parameters examined were limited to those of greatest importance from an aerocapture trajectory performance standpoint, including the approach orbit hyperbolic excess velocity ( $V_{\infty}$ ), the vehicle lift-to-drag ratio (L/D), maximum aerodynamic load factor limit, and the apoapse of the target orbit. The impacts of atmospheric density bias uncertainties are also included.  The corridor data is presented in graphical format, and examples of the utilization of these graphs for mission design and evaluation are included.			
17. Key Words (Suggested by Author(s)) Aerobrake Aerocapture Corridor Lunar/Mars		18. Distribution Statement Unlimited - Unclassified Subject Category - 12	
19. Security Classification (of this report)  Unclassified	20. Security Classification (of this page)  Unclassified	21. No. of pages	22. Price

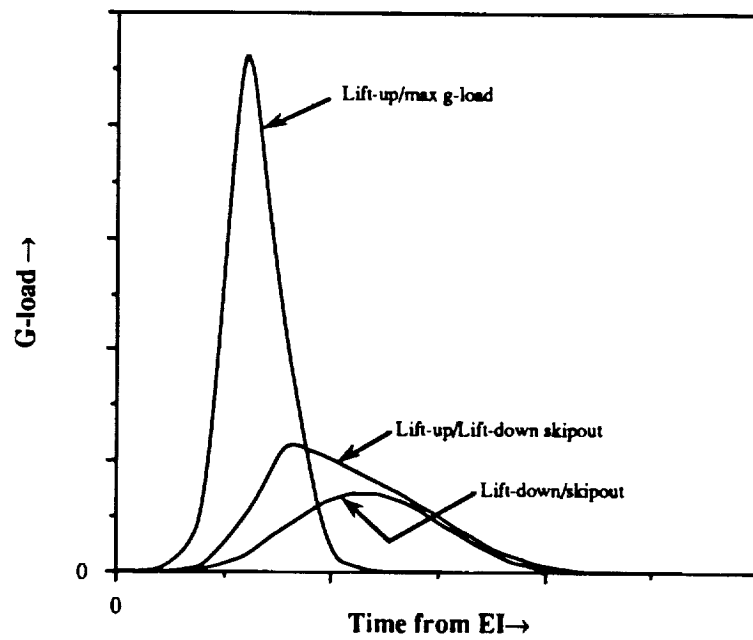
For sale by the National Technical Information Service, Springfield, VA 22161-2171

23 A.





(a) Altitude profiles.



(b) Aerodynamic load profiles.

Figure 2-1. Profiles of open-loop aerocapture trajectories for corridor determination.

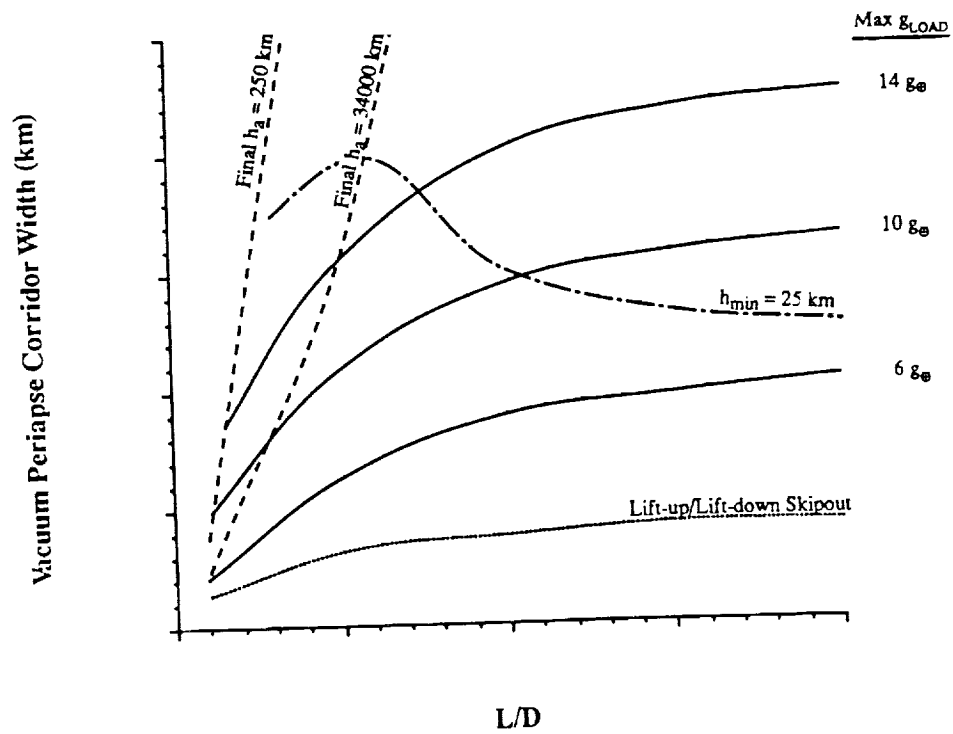


Figure 2-2. Example plot of corridor data.

SECTION 3  
PARAMETRIC AEROCAPTURE CORRIDOR RESULTS

3.1 STUDY CONDITIONS

In the aerocapture corridor definition study, both Earth and Mars were modeled as spherical planets. The 1962 Standard Atmosphere model was used for Earth, while the [International] Committee on Space Research (COSPAR) Northern Hemisphere Mean atmosphere profile (ref. 1) was employed for Mars. Atmospheric entry was initialized at 125 km, and the simulations assumed perfect navigation.

A matrix of vacuum periapse corridors was generated for a wide range of manned and robotic vehicle constraints and mission requirements. Table 3-I lists the parameter ranges.

TABLE 3-I. PARAMETER RANGES

Parameter	Range for Earth	Range for Mars
L/D	0.1 to 2.0	0.1 to 2.0
$V_{\infty}$ (km/s)	1 to 18	2 to 12
g-load limit (Earth g's)	2 to 14	2 to 14
Target apoapse altitude (km)	400, 142 500	250, 34 000
Atmosphere density bias	$\pm 30\%$	- 50%, + 100%
Minimum altitude limit (km)	none	25
Atmosphere model	1962 Standard	COSPAR Northern Hemisphere Mean

The specific values of L/D,  $V_{\infty}$ , and g-load limit that were sampled are listed in table 3-II.

TABLE 3-II. SAMPLED VALUES OF L/D,  $V_{\infty}$ , AND g-LOAD LIMIT

Parameter	Sampled Values for Earth	Sampled Values for Mars
L/D	0.1, 0.3, 0.5, 0.7, 1, 2	0.1, 0.5, 1.0, 1.5, 2.0
$V_{\infty}$ (km/s)	1, 4, 7.56, 10.61, 14, 18	2, 4.71, 6.97, 10, 12
g-load limit (Earth g's)	2, 5, 8, 14	2, 4, 6, 10, 14

The rationale for choosing the specific parameter ranges listed in table 3-I are discussed as follows. The specific range of L/Ds for both Earth and Mars was chosen to reflect the various L/Ds of proposed aerobraking vehicles (i.e., Aeroassist Flight Experiment (AFE), aerobraking vehicles from Mars Rover Sample Return (MRSR) studies, etc.). The low  $V_{\infty}$  of 1 km/s for Earth aerocapture approximates lunar return missions where approach velocities are small. The high  $V_{\infty}$  of 18 km/s for Earth aerocapture was chosen to encompass Mars return missions belonging in the opposition class under worst case phasing conditions. A low  $V_{\infty}$  of 2 km/s for Mars aerocapture is observed for near-Hohmann transfers from Earth. The high  $V_{\infty}$  of 12 km/s for Mars aerocapture is essential for a mission from Earth during the worst synodic period when arrival at Mars occurs near perihelion. The g-load limits ranging from 2g to 14g for both Earth and Mars are chosen to cover both manned and robotic missions. In selecting the target apoapse altitudes, the Space Station orbital altitude of 400 km was designated the low exit target altitude for Earth aerocapture. The high exit target altitude of 142 500 km for Earth aerocapture may be desired for return missions having high approach velocities. A higher exit apoapse altitude requires less dissipation of energy during the aerobrake and is favorable for treating problems in heating and maximum g-load. The high target altitude is also desirable for missions requiring large plane changes. The high target altitude was chosen to be 142 500 km which has a 60-hr period and is slightly less than half the distance to the Moon. A low exit target altitude seen in current studies involving Mars aerocapture is typically at 500 km. However, a more conservative value of 250 km was chosen for this analysis. Also in the current studies involving Mars aerocapture, the high exit target altitude of 34 000 km had been the conventional apoapse altitude for an elliptic one sol orbit ( $34\ 000 \times 250$  km) and was therefore chosen for this analysis. The atmosphere density bias of  $\pm 30$  percent was applied to Earth aerocapture trajectories. Knowledge of the Earth's atmosphere from past observation allows the  $\pm 30$  percent bias to be sufficient for predicting the potential variations in the Earth's atmosphere. However, a decrease of confidence in the martian atmosphere requires application of higher atmosphere biases of  $-50$  percent and  $+100$  percent. A minimum altitude during aerobraking is not essential at Earth since all aerobraking will be performed over the oceans. However, a minimum altitude of 25 km is required at Mars to take into consideration the existing volcanoes and ridges.

The nominal  $C_B$  corresponding to a particular L/D was calculated using the following equations:

$$C_B = \begin{cases} 904 (L/D) - 294 \text{ kg/m}^2 & \text{for } L/D > 0.6 \\ 333 (L/D) + 50 \text{ kg/m}^2 & \text{for } L/D \leq 0.6 \end{cases}$$

These equations are valid for both Earth and Mars. This formula was determined by plotting  $C_B$  versus L/D of existing or proposed aerobraking and atmospheric entry vehicles and curve fitting the data points to obtain an average  $C_B$  versus L/D curve as shown in figure 3-1. These aerospace vehicles include the Apollo, AFE, Mars Excursion Vehicle (MEV) (ref. 5), Mars Transfer Vehicle (MTV) (ref. 5), and vehicles from the MRSR studies of the Lyndon B. Johnson Space Center (JSC)

(ref. 2), Lockheed Missile and Space Company (LMSC) (ref. 3), Martin Marietta Company (MMC) (ref. 4), and TRW.

### 3.2 EARTH AEROCAPTURE CORRIDORS

The entry corridors for Earth aerocapture are given in figures 3-2 to 3-25. The plots include nominal trajectories and cases with  $\pm 30$  percent atmosphere density biases. The corridor widths are plotted as functions of  $L/D$  and  $V_\infty$ . Curves are given for the g-load constraints, the exit apoapse conditions for full lift-up trajectories, and the lift-up/lift-down skipout trajectories (minimum g-load trajectories). These curves are simply curve fits of the corridor widths determined for the sampled values of  $L/D$  or  $V_\infty$  listed in table 3-II.

It is seen in several of the figures (i.e., figures 3-2 and 3-3) that the corridor width boundaries for the g-load constraints and the lift-up/lift-down skipout trajectory curves "split" into two curves. This is due to the sensitivity of the full lift-down trajectories to the vacuum periapse altitude. In most of the Earth aerocapture cases, a hyperbolic exit orbit was separated from a crash case by a mere difference of 1 km in the vacuum periapse altitude for a full lift-down trajectory. For these cases, the lowest vacuum periapse altitude yielding a hyperbolic exit orbit in a full lift-down trajectory was used as the upper bound of the corridor for both exit apoapse altitude conditions. Consequently, only one corridor width for both exit apoapse altitude conditions was calculated for each g-load constraint. However, in several of the low  $V_\infty$  flights (i.e.,  $V_\infty = 1$  and 4 km/s), the full lift-down flights were less sensitive to the vacuum periapse altitude. For such cases, the highest vacuum periapse altitude resulting in an exit apoapse altitude lower than the target altitude in a full lift-down trajectory was used for the corresponding target apoapse altitude condition. If this meant a crash case for the 400-km target altitude, then the lowest vacuum periapse altitude without yielding a crash case was used. Therefore, two corridor widths as functions of the exit apoapse altitude conditions were calculated for each maximum g-load constraint. For such cases, if the difference between the two corridor widths for a constraint were less than or equal to 4 km, then only the conservative value is plotted simply for improving the readability of the graphs. Else if the difference between the two corridor widths for a constraint were greater than 4 km, then both data points would remain plotted, one for each exit apoapse altitude condition. An example of a plot displaying two corridor widths for a constraint curve is seen on the  $V_\infty = 1$  km/s plot with nominal atmosphere (fig. 3-2). For each of the 5g and 8g constraint curves, the corridor widths for the two exit apoapse conditions had differences of 5 km at a low  $L/D$  of 0.3. Therefore two data points were plotted. However, at higher  $L/D$ s, the corridor widths for the two exit apoapse conditions were either identical or had differences of less than or equal to 4 km. Therefore, for this portion only one curve was required, and a maximum error of + 4 km is possible for the high exit apoapse condition. This caused the "split-ends" on the 5g and 8g constraint curves. The higher corridor widths at the split-ends are applicable to the 142 500-km target apoapse altitude, while the lower corridor widths are for the 400-km target apoapse condition.

Similar to the full lift-down trajectories, the lift-up/lift-down skipout trajectories could be very sensitive to the vacuum periapse altitude. For cases where the lift-up/lift-down skipout trajectories were less sensitive to the vacuum periapse altitude (i.e., low  $V_\infty$  and  $L/D$  cases), two vacuum periapse altitudes, one for each exit apoapse altitude condition, were obtained as the lower bounds of the corridors. Consequently, the corridors of lift-up/lift-down skipout trajectories could possibly have two vacuum periapse altitudes for the lower bound (resulting from the lift-up/lift-down skipout trajectory) as well as two vacuum periapse altitudes for the upper bound (resulting from the lift-down trajectory). By matching the appropriate upper and lower bounds for each exit apoapse condition, two corridor widths were calculated, one for each exit apoapse condition. Subsequently, the method used for plotting the corridor data points as mentioned in the previous paragraph was then applied to the lift-up/lift-down skipout trajectories. An example is found in the  $V_\infty = 4$  km/s plot (fig. 3-3) where

the lift-up/lift-down skipout trajectory displayed a split-end. The higher corridor width at the split-end corresponds to the 400-km target apoapse condition, and the lower corridor width is for the 142 500-km target altitude (opposite of the g-load curves). For the single curve portion of the lift-up/lift-down skipout trajectory, a maximum error of  $\pm 4$  km is possible for the low exit apoapse condition. For the  $V_{\infty} = 1$  km/s plot, the corridor width differences for the lift-up/lift-down skipout trajectory were consistently greater than 4 km. Therefore, two separate curves were essential for the lift-up/lift-down skipout trajectory.

The lift-up/lift-down skipout trajectory curve is applicable as a constraint only for the full lift-up trajectories (see Corridor Determination, sec. 2.2). An example is given in the  $V_{\infty} = 12$  km/s plot (fig. 3-31) for Mars aerocapture. On the graph, the 6g constraint curve was removed from the plot since it was located below the lift-up/lift-down skipout trajectory curve. Therefore, a vehicle with an approach velocity of 12 km/s would not be able to perform a full lift-up aerocapture without violating a 6g constraint. In other words, a vehicle with a 6g constraint will skip out if flying at the lower boundary of the corridor at full lift-up. However, this does not imply that guided trajectories with maximum g-loads of 6g or less will also skip out. It is possible for a vehicle to bound the maximum g-load to 6g or less during the aerocapture without skipping out by flying a guided trajectory (incorporating lift-down) and entering the atmosphere with a higher vacuum periapse altitude than that of the full lift-up trajectory. Since a higher entry vacuum periapse altitude will be required for the lower boundary of the corridor, the corridor width will hence be reduced. Therefore, for Mars aerocapture with an approach velocity of 12 km/s, a reduced corridor width may exist for a 6g or less constraint. In general, there is a reduction in all existing corridor widths falling below a lift-up/lift-down skipout trajectory curve; however, the reduced corridor width cannot be determined with the method used in this analysis.

The lift-up/lift-down skipout trajectory curves do not represent constant g-load lines. The maximum g-load tends to increase along the curve as the L/D increases on a  $V_{\infty}$  plot. For Earth aerocapture with low  $V_{\infty}$ 's (i.e.,  $V_{\infty} = 1$  and 4 km/s), the gradient of the maximum g-load along the lift-up/lift-down skipout trajectory curve is on the order of less than one-g throughout the range of L/Ds analyzed. At a higher  $V_{\infty}$  such as  $V_{\infty} = 18$  km/s, the gradient of the maximum g-load greatly increases to approximately 15g for the range of L/Ds analyzed. For an L/D plot, the maximum g-load also increases along the curve as the  $V_{\infty}$  increases.

To calculate the corridor widths of the exit apoapse altitude condition curves for the full lift-up trajectories, one upper bound from the full lift-down trajectories and one lower bound from the full lift-up trajectories were determined for each exit apoapse condition. As discussed previously, the upper-bound vacuum periapse altitudes for the two exit apoapse conditions may or may not coincide. Regardless of whether the upper bounds for the two exit apoapse conditions coincide or not, the appropriate upper and lower bounds were matched for a particular exit apoapse condition, and the corridor width was then calculated. Therefore, a unique curve was displayed for each exit apoapse altitude condition.

As discussed in the Corridor Determination section (sec. 2.2), the exit apoapse altitude condition curves are meaningful as constraints only for full lift-up trajectories. The exit apoapse altitude constraint curves are not applicable to the guided trajectories flown inside the entry corridor. Given a vehicle with an L/D of 0.7, a g-load limit of 5g, a  $V_{\infty}$  of 5.8 km/s for Earth aerocapture, and an entry corridor of 30 km, an exit target altitude of 142 500 km for a full lift-up trajectory was obtained from figure 3-11. This means that an exit target altitude of 142 500 km is feasible when performing an aerocapture with any vacuum periapse altitude falling within the corridor. For example, the target altitude is achieved by simply flying a full lift-up trajectory at the lower corridor boundary, a full lift-down trajectory at the upper corridor boundary, or a guided trajectory inside the entry corridor. However, the given vehicle would not be restricted to flying only trajectories with a 142 500-km exit

altitude. The vehicle could be guided to achieve any exit altitude desired but with certain restrictions. Theoretically, at the upper bound which was determined by the full lift-down trajectory, exit altitudes lower than 142 500 km would not be possible since the vehicle is already saturated with full lift-down. A lower exit altitude is obtainable only if a lower vacuum periapse altitude were flown. Therefore, the capability of the vehicle to achieve an exit altitude lower than 142 500 km improves as the entry vacuum periapse altitude is decreased from that of the upper bound. Similarly, at the lower bound which was determined by the full lift-up trajectory, exit altitudes higher than 142 500 km would not be possible. The capability of the vehicle to achieve an exit altitude higher than 142 500 km improves as the entry vacuum periapse altitude deviates from the lower bound. In summary, as long as the entry vacuum periapse altitude falls within the entry corridor for a given exit target altitude, the vehicle can be guided to achieve that specific exit target condition without violating the given g-load constraint. Furthermore, the vehicle can also be guided to achieve any other exit apoapse altitude desired, regardless of whether it is above or below the given exit target altitude of the corridor. However, the capability of the guided vehicle to perform such a task will deteriorate as the vacuum periapse altitude approaches the lower or upper bound values of the corridor.

In several of the low  $L/D$  flights (i.e.,  $L/D = 0.1$ ), data did not exist at low  $V_\infty$ 's for certain high g-load constraint curves. Such cases occurred since the vehicle would simply crash in lift-up trajectories without ever violating the high g-load limits. In the high  $L/D$  flights (i.e.,  $L/D = 0.7, 1$ , and  $2$ ), the low exit apoapse altitude curves had large corridor widths and, therefore, were outside the range of the plots.

Note that the g-load constraint curves tend to level out at higher  $L/D$ s (i.e.,  $L/D \geq 1.3$ ). The g-load is defined as

$$g_{LOAD} = (Lift^2 + Drag^2)^{1/2} / g_{0\oplus}$$

where *Lift* and *Drag* are the lift and drag accelerations. This equation can also be written as

$$g_{LOAD} = Drag [(L/D)^2 + 1]^{1/2} / g_{0\oplus}$$

This equation demonstrates that for vehicles with low  $L/D$ , the g-load constraint is primarily a function of the atmospheric drag encountered along the trajectory. This is, in turn, controlled principally by the ballistic entry interface flight path angle or orbit periapse. For a given vehicle a steeper EI flight path entails higher drag and therefore g-loading on a lift-up trajectory. For lower  $L/D$ s, as the  $L/D$  increases, the achieved minimum altitude is raised enabling a steeper EI flight path to achieve a fixed g-load constraint. However, as  $L/D$  increases past approximately 1.3, the  $L/D$  characteristics significantly modify the sensed vehicle g-load, as the factor  $[(L/D)^2 + 1]^{1/2}$  becomes significant. This effect reduces the effect of  $L/D$  in raising the lift-up minimum altitude and causes the entry corridor width for a g-load constraint curve to remain fairly constant as the  $L/D$  is increased for high  $L/D$  vehicles.

The vacuum periapse altitudes which define the boundaries of an entry corridor will increase for a denser atmosphere and decrease for a lighter atmosphere. In terms of corridor widths, the entry corridors showed only second-order sensitivity to the constant atmosphere dispersions. A denser atmosphere resulted in a slight decrease in the corridor width, while a lighter atmosphere caused an increase, with a few exceptions in which the opposite actually occurred. However, to reduce the amount of data presented in this report, the data for cases with the + 30 percent and - 30 percent atmosphere biases were combined to produce only one set of vacuum periapse corridor widths. This was accomplished by using the vacuum periapse altitudes of lift-down trajectories (upper boundary of corridor) in the light atmosphere and the vacuum periapse altitudes of lift-up trajectories (lower

boundary of corridor) in the heavy atmosphere to calculate the corridor widths. This method yielded the most narrow corridor widths possible. The atmosphere density dispersions decreased the corridor widths by a maximum of 8 km.

The vacuum periaapse corridor widths can be easily converted to EI flight path angle corridor widths. The conversion chart for Earth aerocapture is given in figure 3-26. The conversion factors given are accurate to  $\pm 0.1^\circ$  in the EI flight path angle corridor widths.

### 3.3 MARS AEROCAPTURE CORRIDORS

The entry corridors for Mars aerocapture are given in figures 3-27 to 3-46. The plots include nominal trajectories and cases with +100 percent and -50 percent atmosphere density biases. The corridor widths are plotted as functions of  $L/D$  and  $V_\infty$ . Curves are given for the g-load constraints, the exit apoapse conditions for full lift-up trajectories, the lift-up/lift-down skipout trajectories, and the minimum altitude constraint.

A discussion of the corridor width plots for nominal trajectories and cases with atmosphere density biases is presented in the Earth Aerocapture Corridor section (sec. 3.2). The atmosphere density dispersions decreased the corridor widths by a maximum of 40 km for Mars aerocapture. One factor which caused the much larger reduction of the corridor widths for Mars aerocapture than for Earth aerocapture was the larger atmosphere dispersions placed on Mars aerocapture.

The chart for converting the vacuum periaapse corridor widths to EI flight path angle corridor widths for Mars aerocapture is given in figure 3-47. The EI flight path angle corridor widths calculated from the chart have an accuracy of  $\pm 0.1^\circ$ .

### 3.4 EXAMPLES AND DISCUSSION OF DATA UTILIZATION

As discussed in the Background section (sec. 2.1), the entry corridor data can be used in the preliminary design of missions involving aerocapture. Examples are given in this section for (1) the determination of minimum vehicle  $L/D$  required for aerocapture, (2) the trade-offs between design parameters such as the vehicle  $L/D$  and the approach velocity, and (3) a feasibility check of proposed mission designs.

For a given interplanetary trajectory, the entry corridor data can be used to indicate the minimum vehicle  $L/D$  required for aerocapture. For example, the baseline entry velocity (at 122 km altitude) for the lunar/Mars study is approximately 12.5 km/s for Earth aerocapture (ref. 6). This corresponds to a  $V_\infty$  of 5.8 km/s. In addition, a maximum g-load constraint of approximately 5g is placed on the vehicle (ref. 6). By interpolating between the  $V_\infty = 4$  km/s and the  $V_\infty = 7.56$  km/s plots (figs. 3-3 and 3-4) or by examining the  $L/D$  plots, it can be seen that a large range of vehicle  $L/D$ s will satisfy the mission requirements. A maximum corridor width of approximately 41 km is possible for the 2.0  $L/D$  (see fig. 3-13); a corridor width of 29 km exists for the 0.7  $L/D$  (see fig. 3-11), and so forth. However, the  $L/D = 0.1$  plot (fig. 3-8) shows that the 5g constraint curve falls below the lift-up/lift-down skipout trajectory curve for the 400-km exit apoapse condition. This indicates that a vehicle with a maximum  $L/D$  of 0.1 will not be able to successfully capture and burn off enough energy to exit into a 400-km target altitude in a trajectory that maintains full lift-up till periapse. However, the same 5g constraint curve lies above the lift-up/lift-down skipout trajectory curve for the 142 500-km exit apoapse condition. Therefore, for a full lift-up trajectory the 142 500-km target altitude as well as other target altitudes falling between 400 km and 142 500 km are feasible for the 0.1  $L/D$  vehicle with a 5g constraint.



The entry corridor plots are useful in providing the trade-offs between design parameters. For example, given a  $V_\infty$  of 6.97 km/s with a 50-km corridor width requirement and a 4g limit for Mars aerocapture, figure 3-29 shows that no L/D will meet the 4g constraint. If the g-load limit were raised to 6g, then an L/D of 1.7 or greater would be required. Else, if the  $V_\infty$  were lowered to 4.71 km/s (fig. 3-28), then an L/D of 1.0 or greater would be required.

Lastly, the entry corridor plots are useful for performing feasibility checks of proposed mission designs. For example, suppose a design team proposes an Earth return aerocapture mission with an approach trajectory  $V_\infty$  of 10.61 km/s. Their proposed aerocapture vehicle has an L/D of 0.7. The question arises as to the resultant aerodynamic loads experienced during aerocapture and the maximum corridor width available to handle dispersions in the planetary approach trajectory. Figure 3-5 indicates that a maximum g-load of 8g will result if a 25-km corridor width is required to cover dispersions. Note that this would probably be unacceptable for manned aerocapture. Figure 3-5 illustrates that the maximum g-load would decrease somewhat if the vehicle L/D were increased; however, a minimum value of roughly 6g ( $L/D = 2.0$ ) is still high and might point to the necessity of decreasing the entry speed.

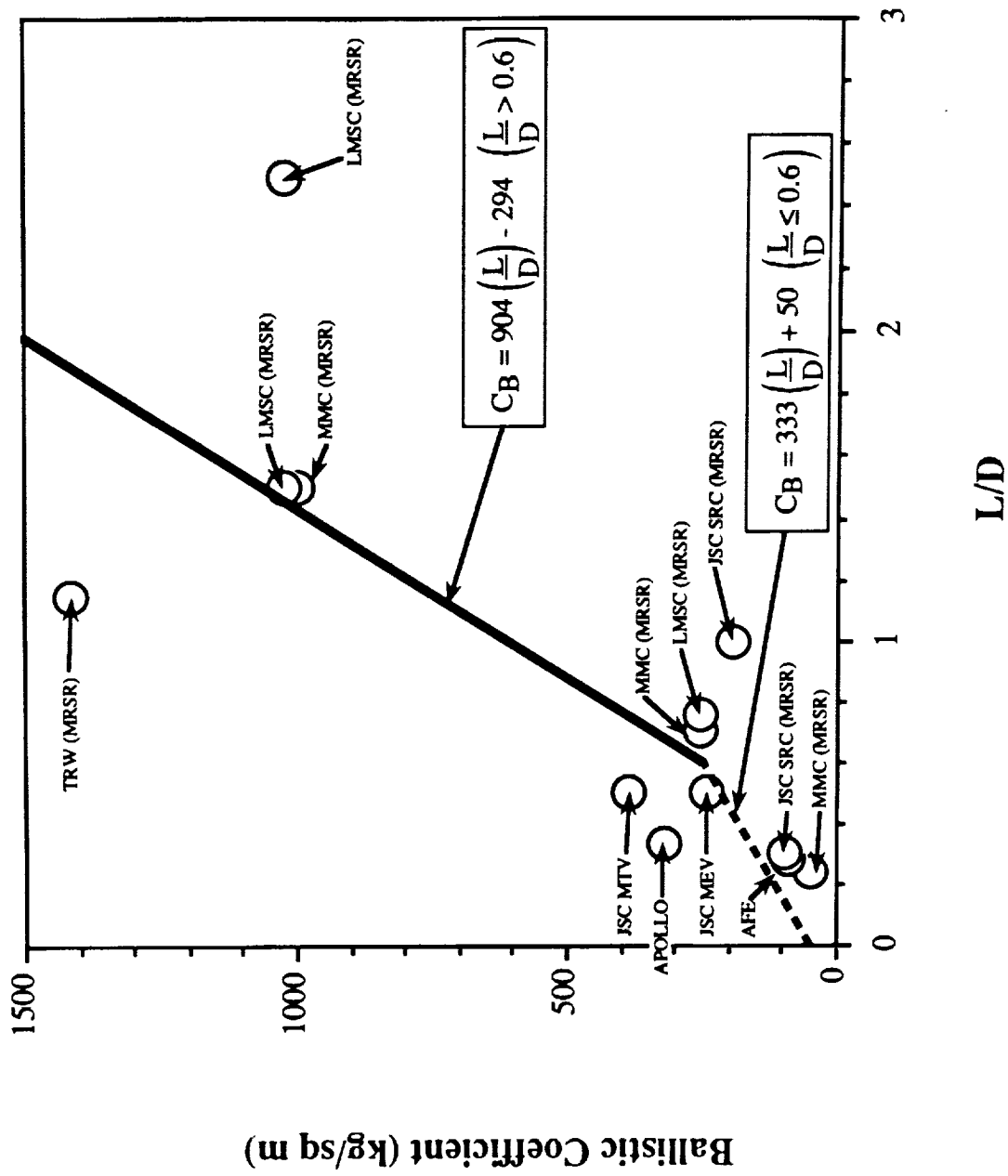


Figure 3-1. Ballistic coefficient versus lift-to-drag.

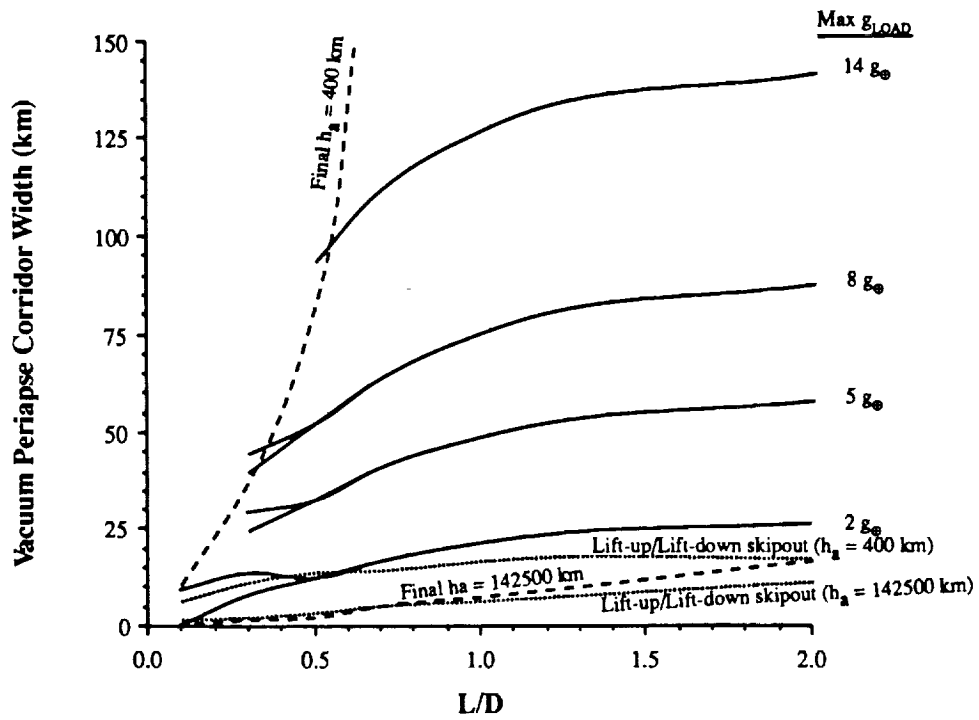


Figure 3-2. Earth:  $V_{\infty} = 1$  km/s with nominal atmosphere.

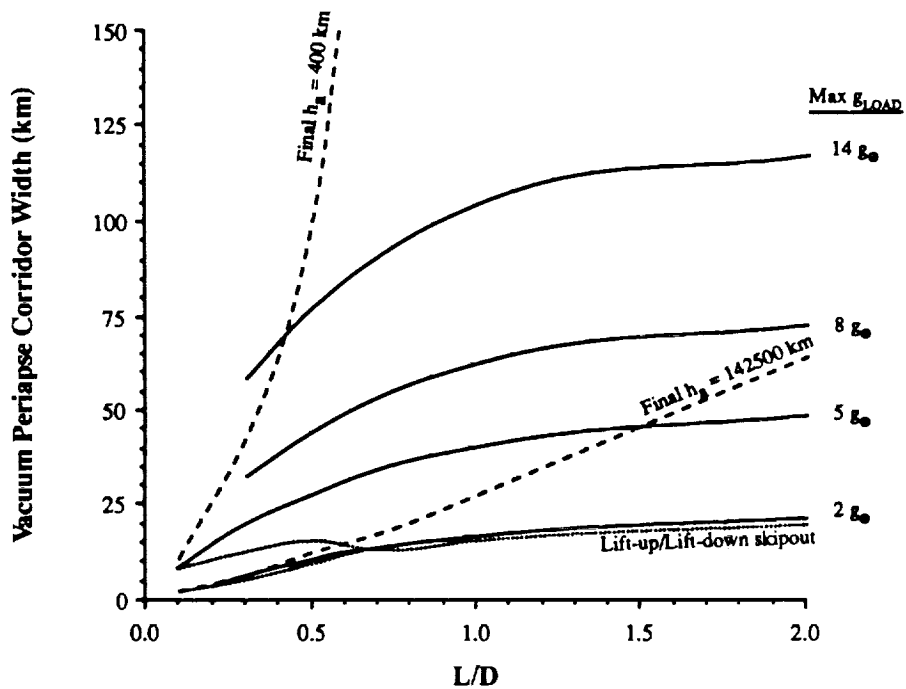


Figure 3-3. Earth:  $V_{\infty} = 4$  km/s with nominal atmosphere.

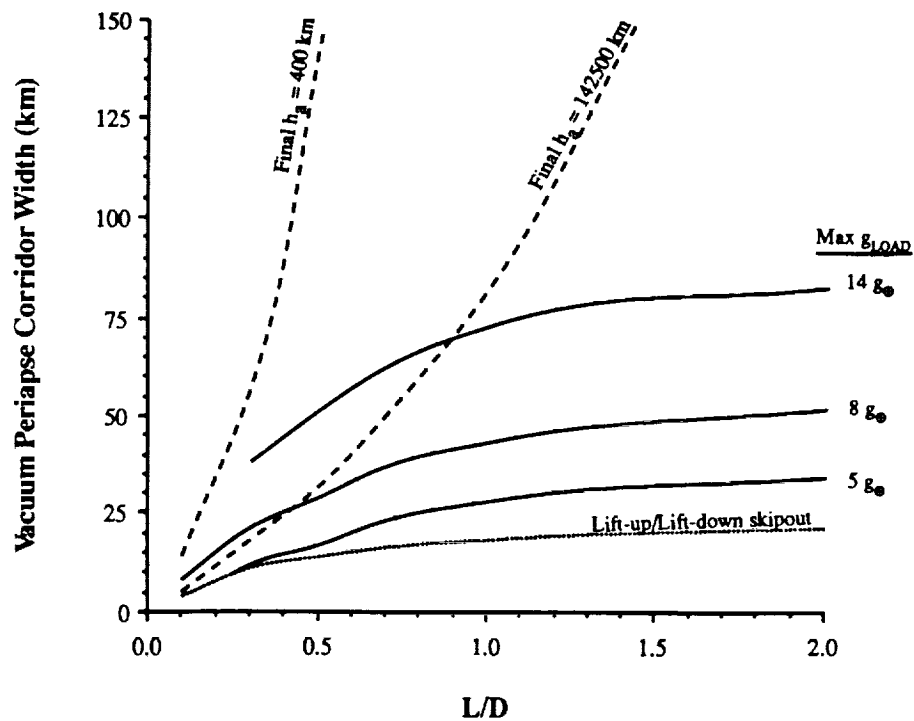


Figure 3-4. Earth:  $V_\infty = 7.56$  km/s with nominal atmosphere.

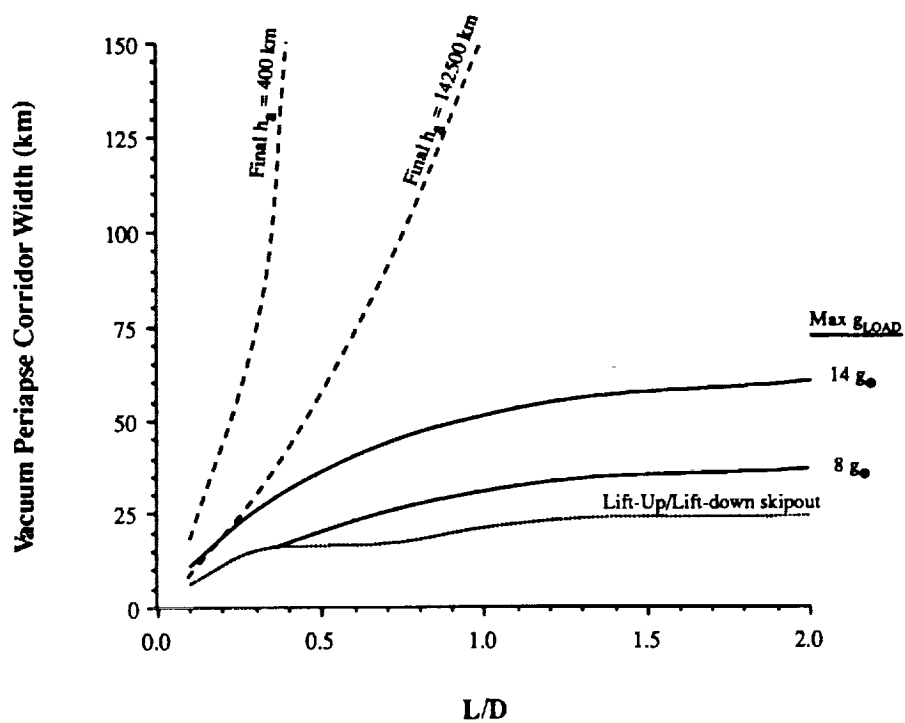


Figure 3-5. Earth:  $V_\infty = 10.61$  km/s with nominal atmosphere.

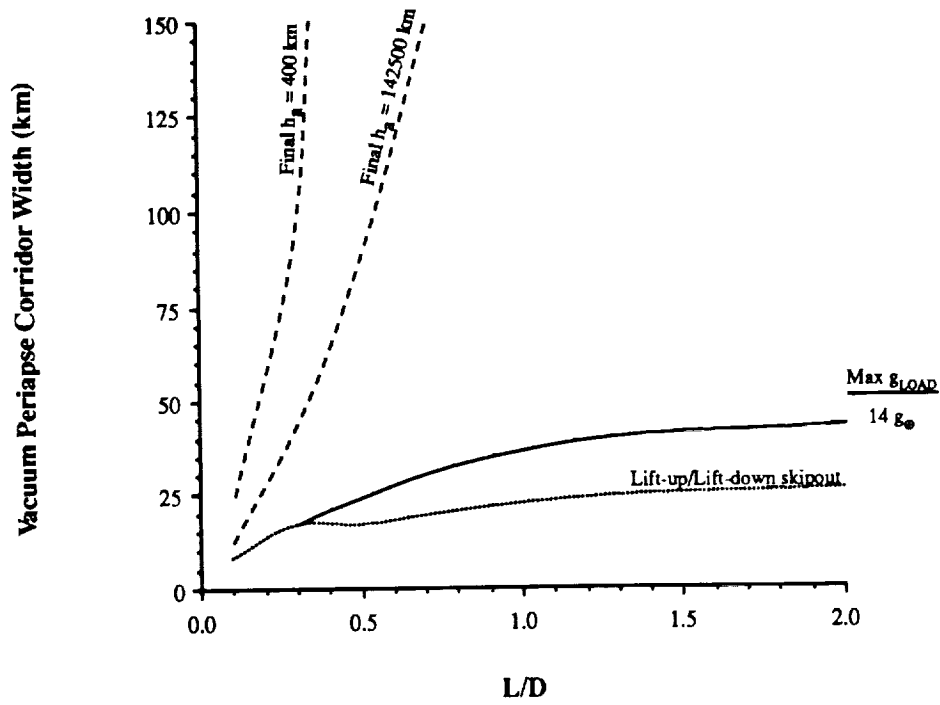


Figure 3-6. Earth:  $V_\infty = 14 \text{ km/s}$  with nominal atmosphere.

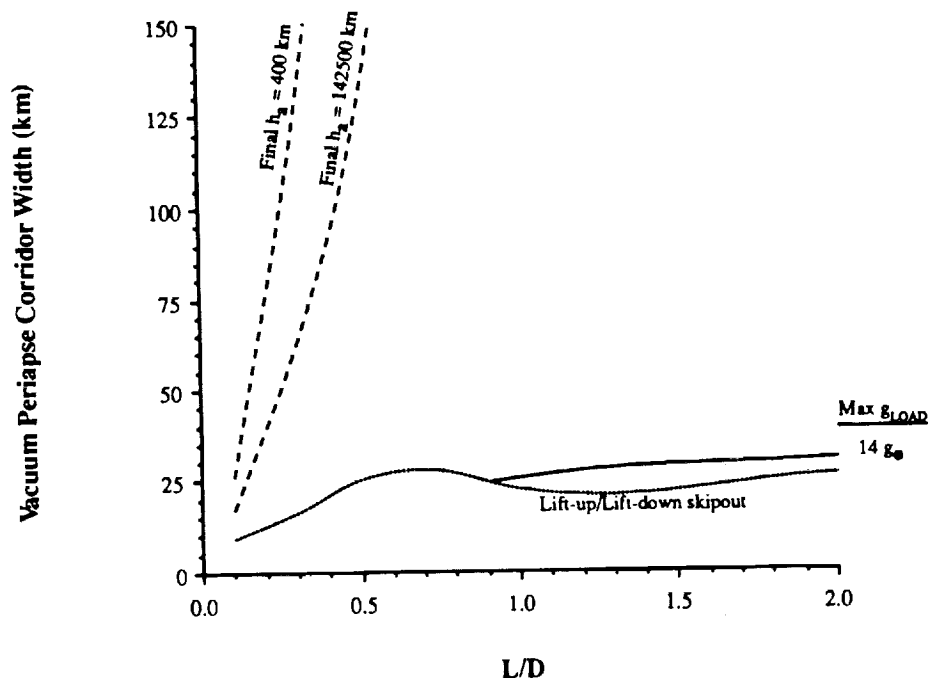


Figure 3-7 Earth  $V_\infty = 18 \text{ m/s}$  with nominal atmosphere.

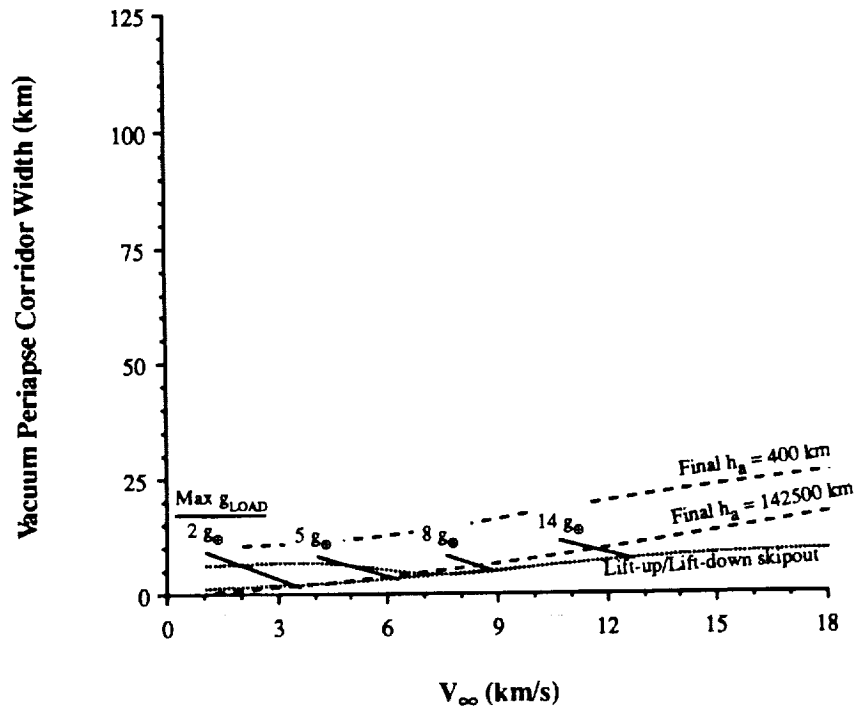


Figure 3-8. Earth:  $L/D = 0.1$  with nominal atmosphere.

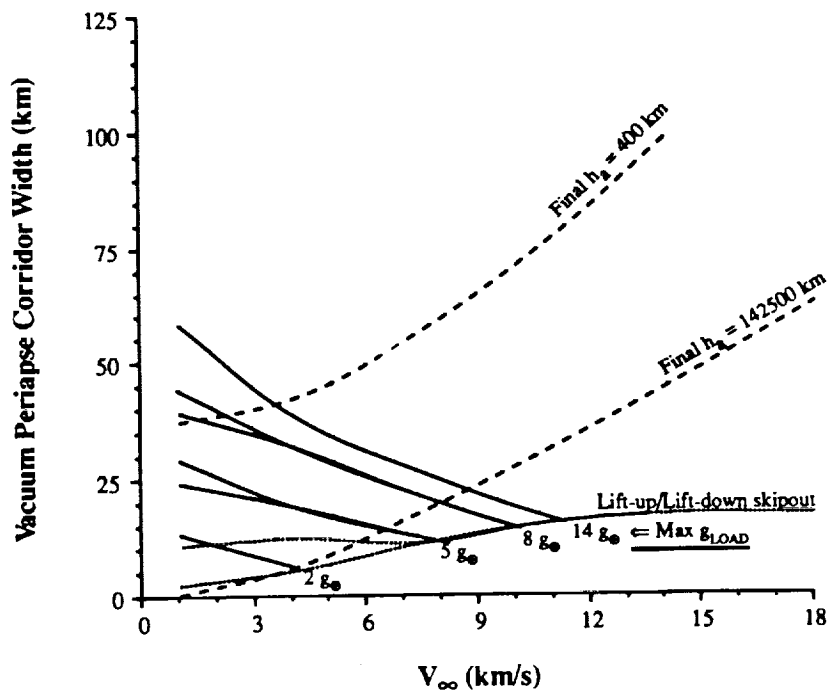


Figure 3-9. Earth  $L/D = 0.3$  with nominal atmosphere.

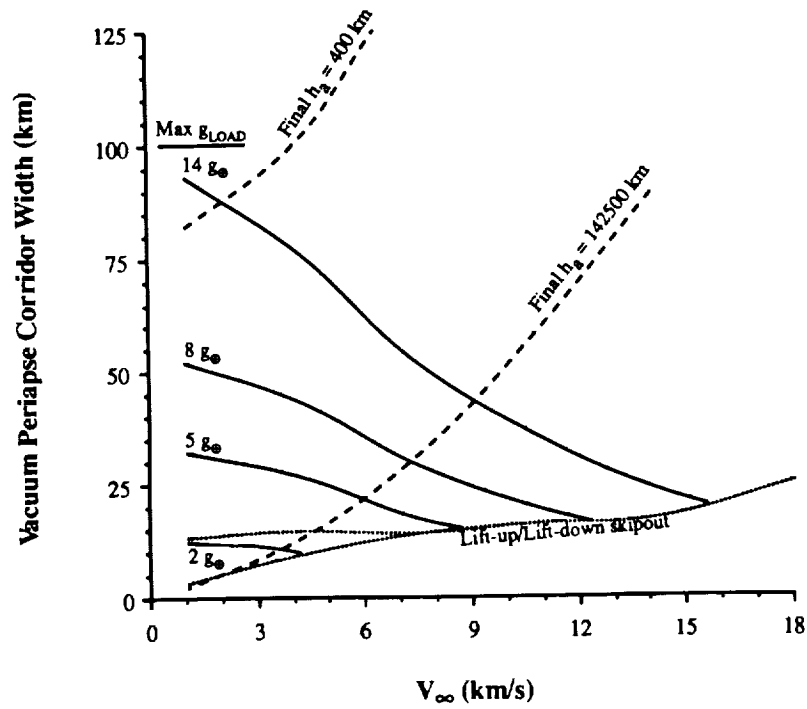


Figure 3-10. Earth:  $L/D = 0.5$  with nominal atmosphere.

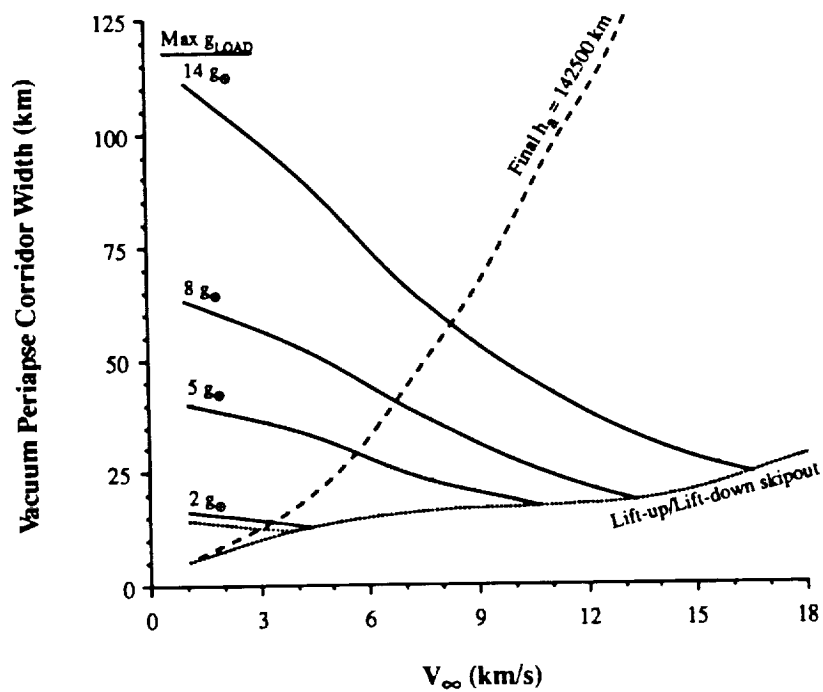


Figure 3-11. Earth:  $L/D = 0.7$  with nominal atmosphere.

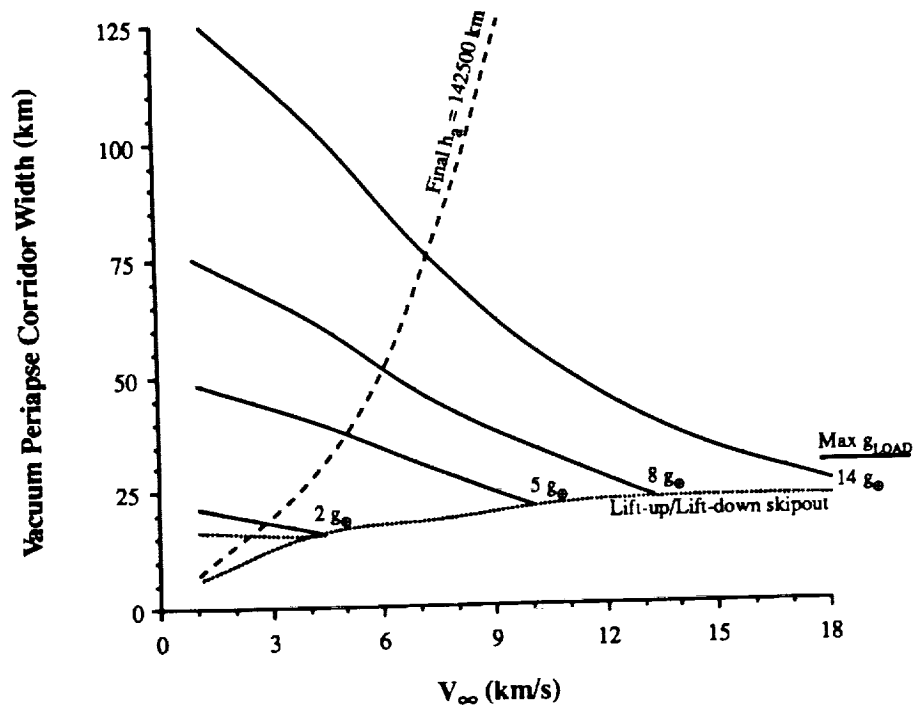


Figure 3-12. Earth:  $L/D = 1$  with nominal atmosphere.

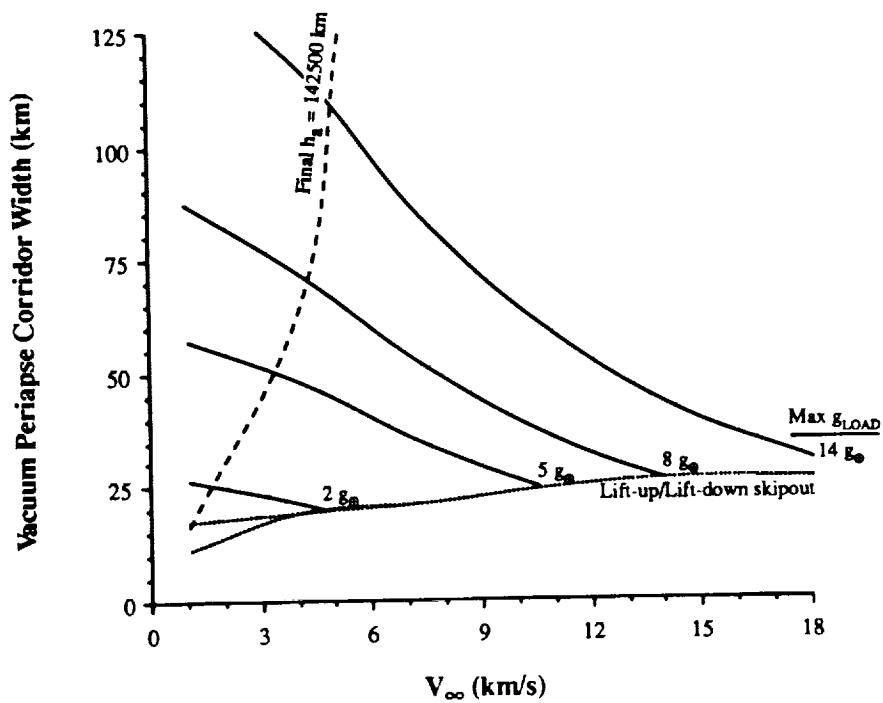


Figure 3-13 Earth  $L/D = 2$  with nominal atmosphere.



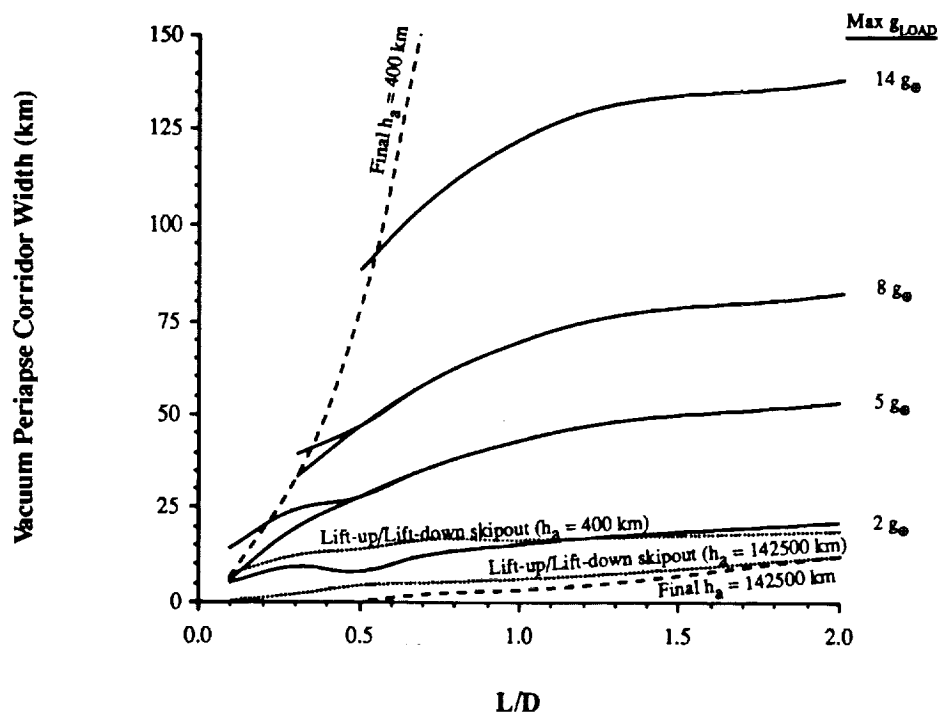


Figure 3-14. Earth:  $V_{\infty} = 1$  km/s with  $\pm 30$  percent atmosphere dispersions.

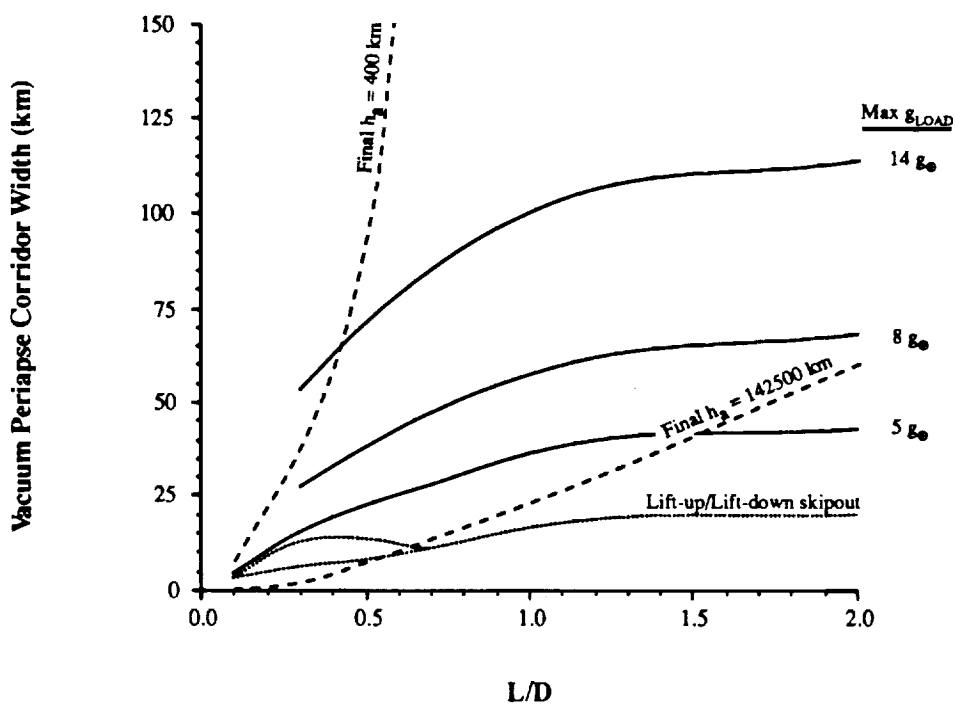


Figure 3-15. Earth:  $V_{\infty} = 4$  km/s with  $\pm 30$  percent atmosphere dispersions.

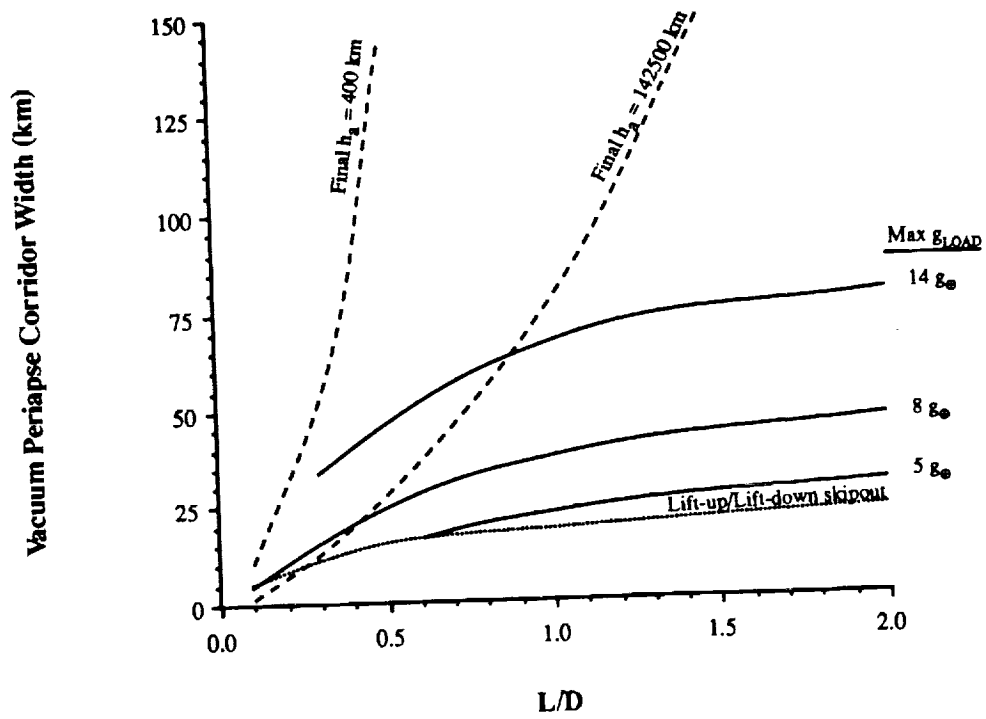


Figure 3-16. Earth:  $V_{\infty} = 7.56$  km/s with  $\pm 30$  percent atmosphere dispersions.

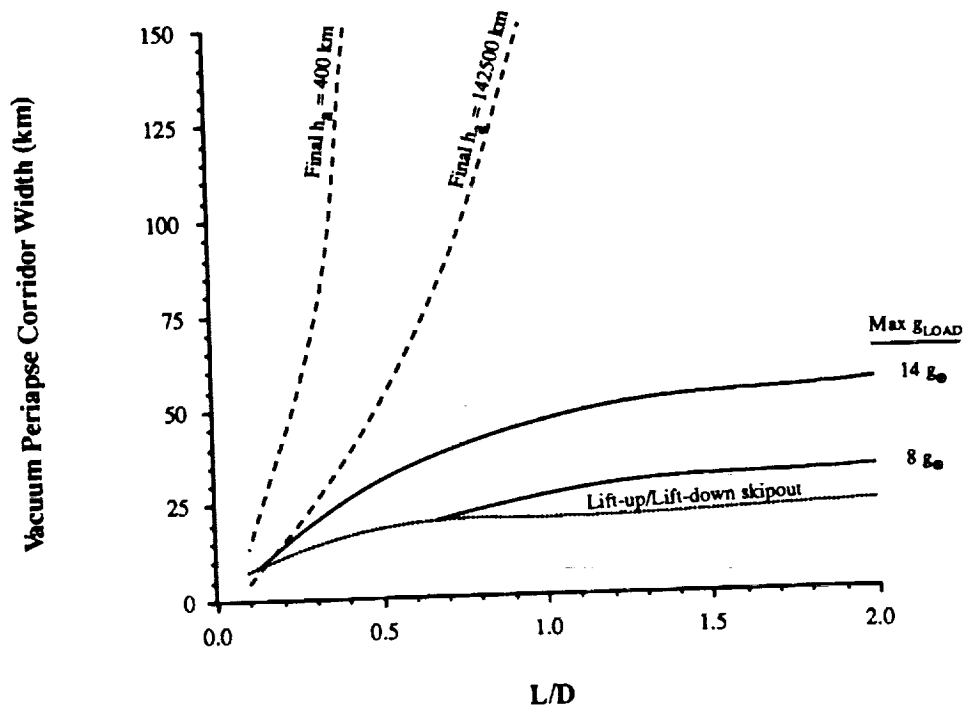


Figure 3-17. Earth:  $V_{\infty} = 10.61$  km/s with  $\pm 30$  percent atmosphere dispersions.

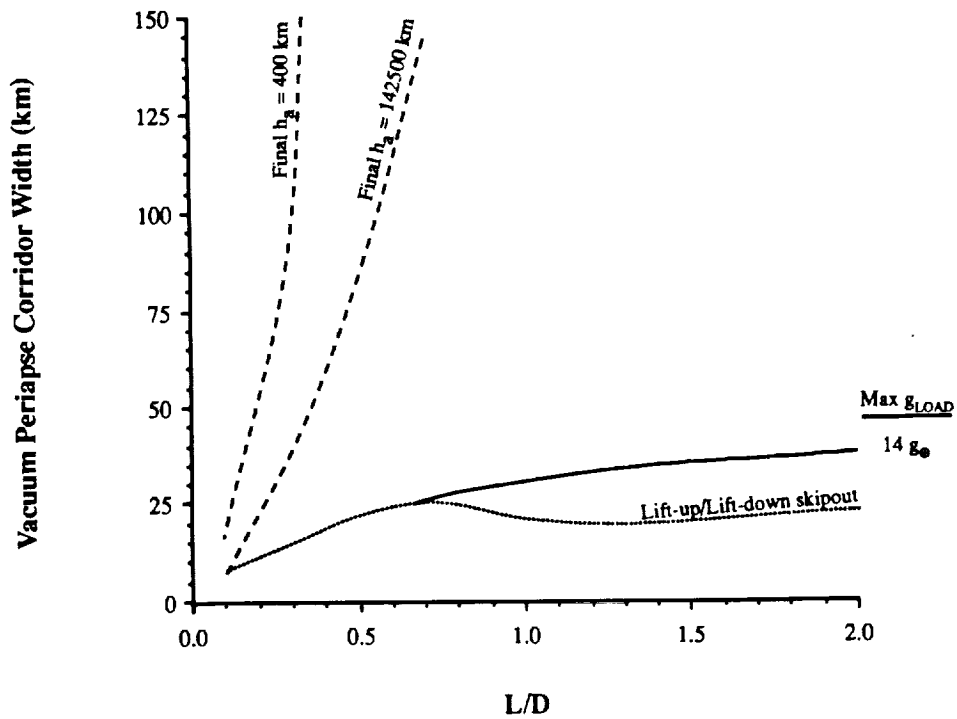


Figure 3-18. Earth:  $V_{\infty} = 14 \text{ km/s}$  with  $\pm 30$  percent atmosphere dispersions.

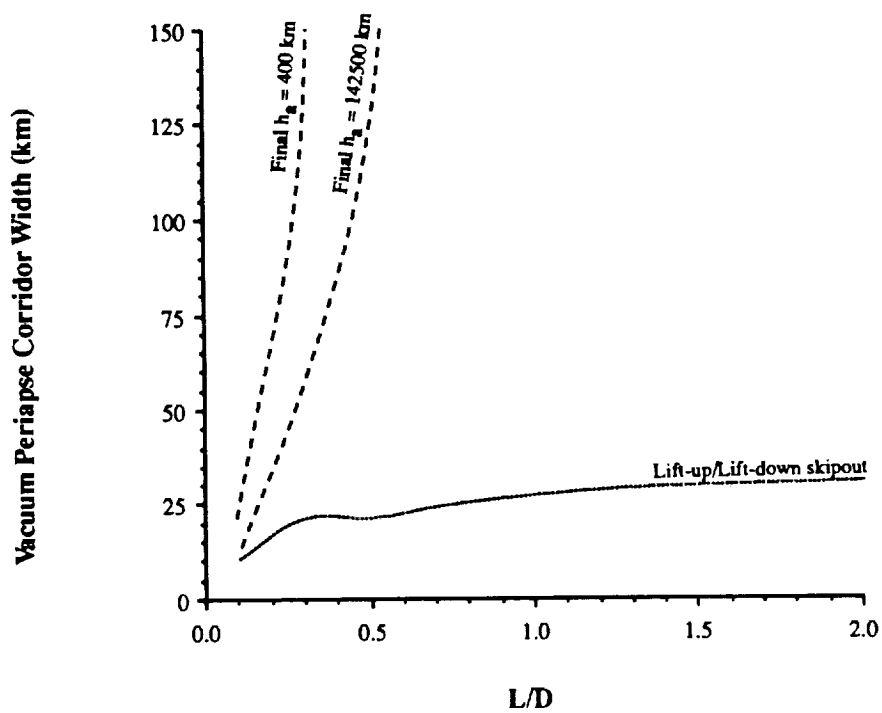


Figure 3-19. Earth:  $V_{\infty} = 18 \text{ km/s}$  with  $\pm 30$  percent atmosphere dispersions.

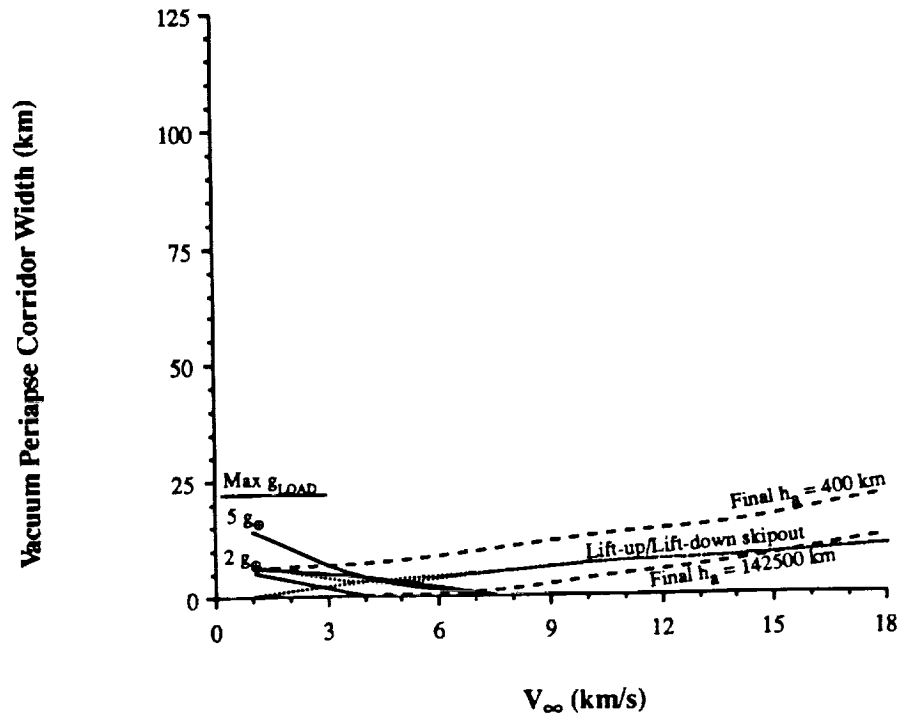


Figure 3-20. Earth:  $L/D = 0.1$  with  $\pm 30$  percent atmosphere dispersions.

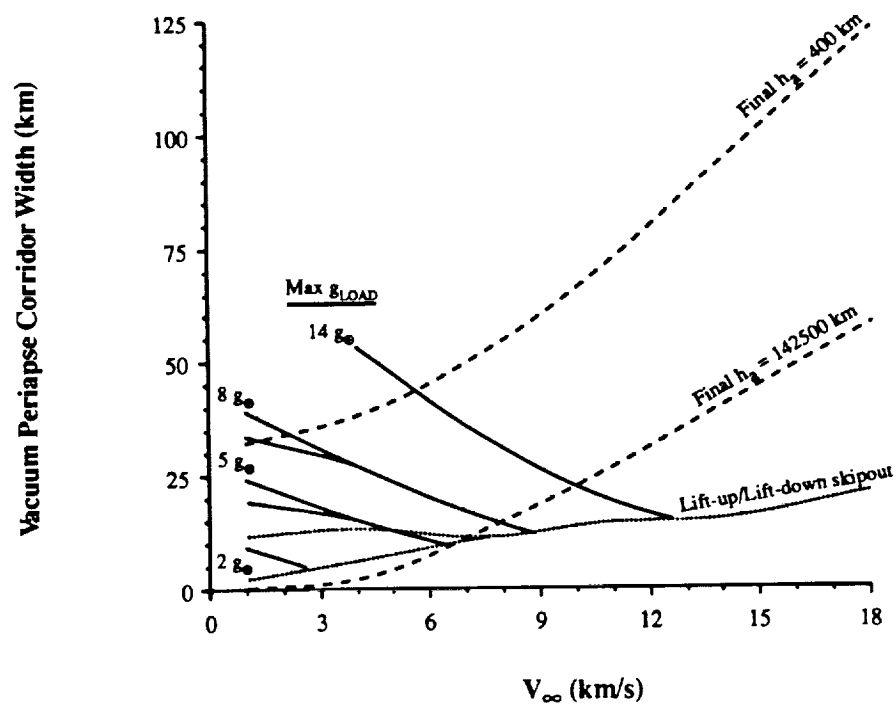


Figure 3-21. Earth:  $L/D = 0.3$  with  $\pm 30$  percent atmosphere dispersions.

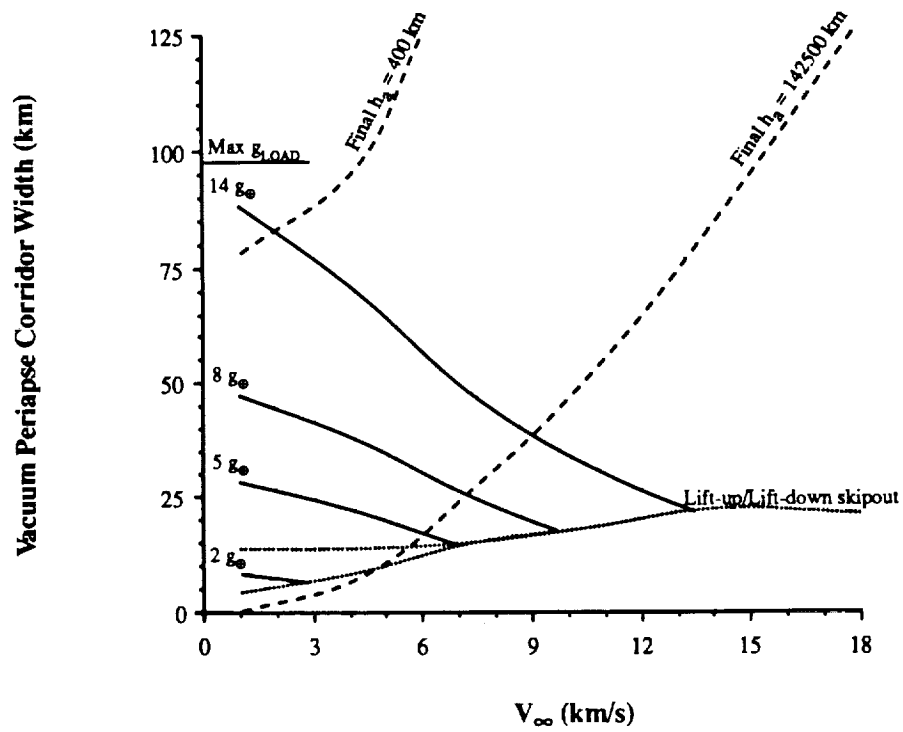


Figure 3-22. Earth:  $L/D = 0.5$  with  $\pm 30$  percent atmosphere dispersions.

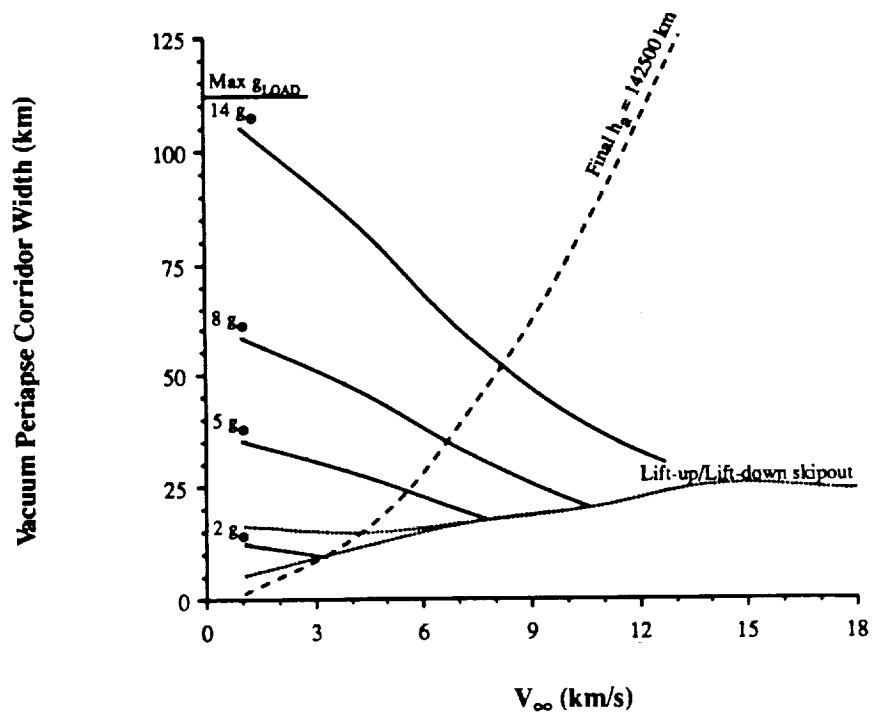


Figure 3-23. Earth:  $L/D = 0.7$  with  $\pm 30$  percent atmosphere dispersions.

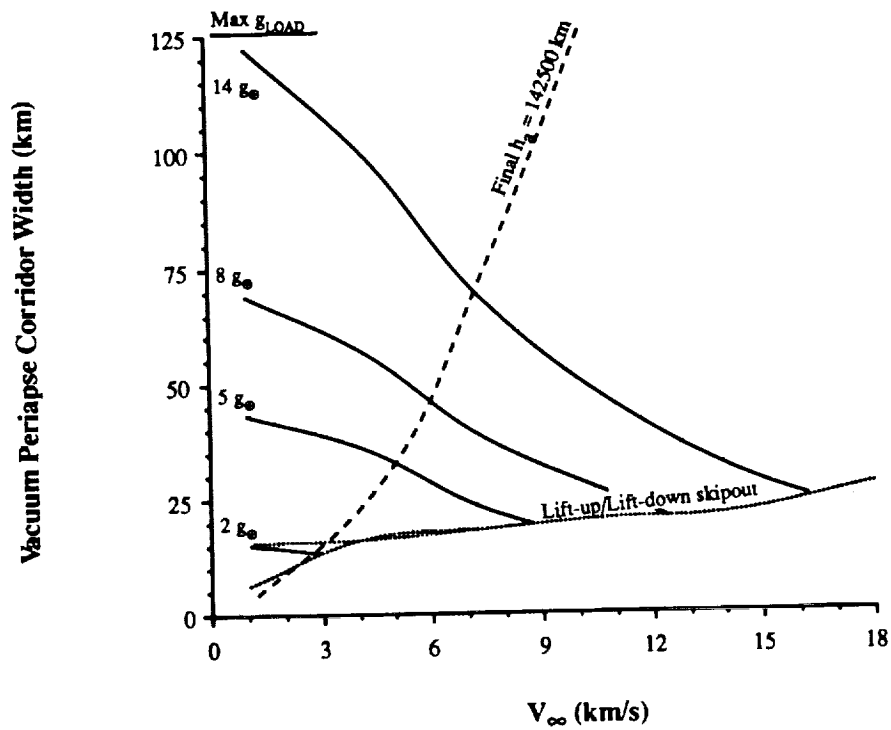


Figure 3-24. Earth:  $L/D = 1$  with  $\pm 30$  percent atmosphere dispersions.

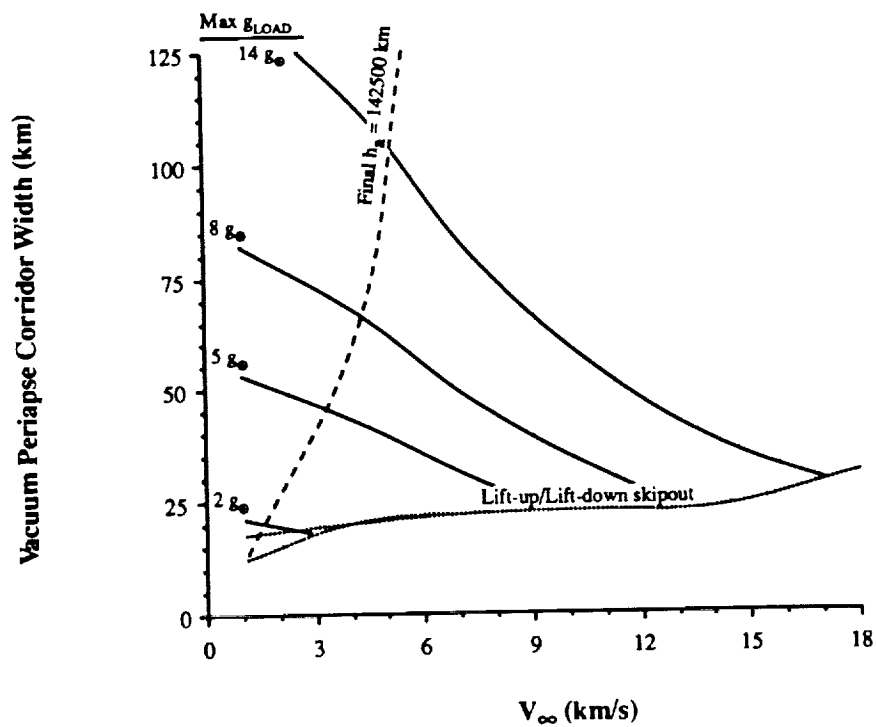


Figure 3-25. Earth:  $L/D = 2$  with  $\pm 30$  percent atmosphere dispersions.

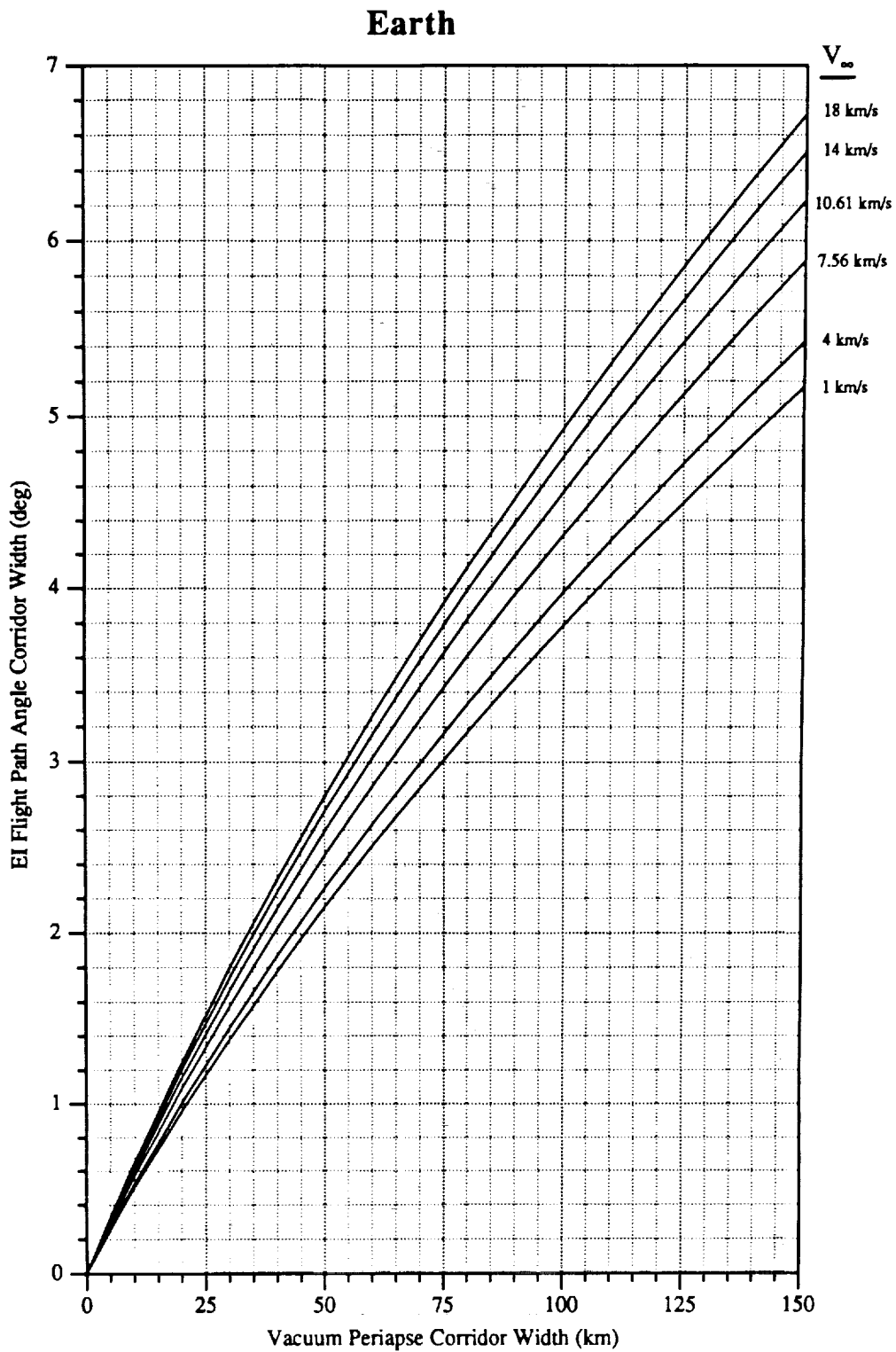


Figure 3-26. Earth: Vacuum periapse corridor width to El flight path angle corridor width conversion chart.

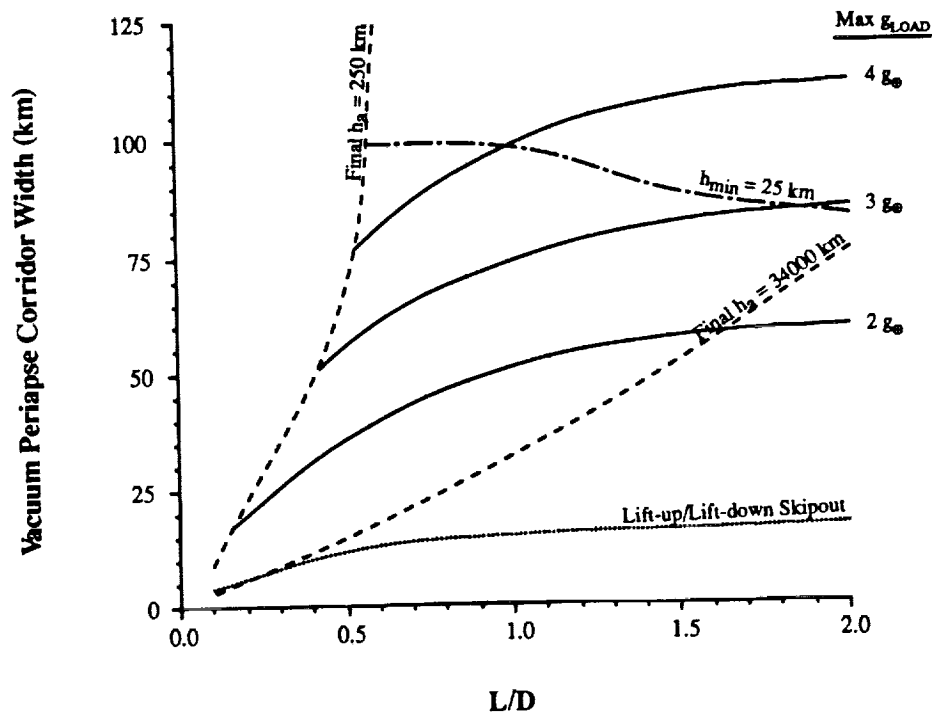


Figure 3-27. Mars:  $V_{\infty} = 2$  km/s with nominal atmosphere.

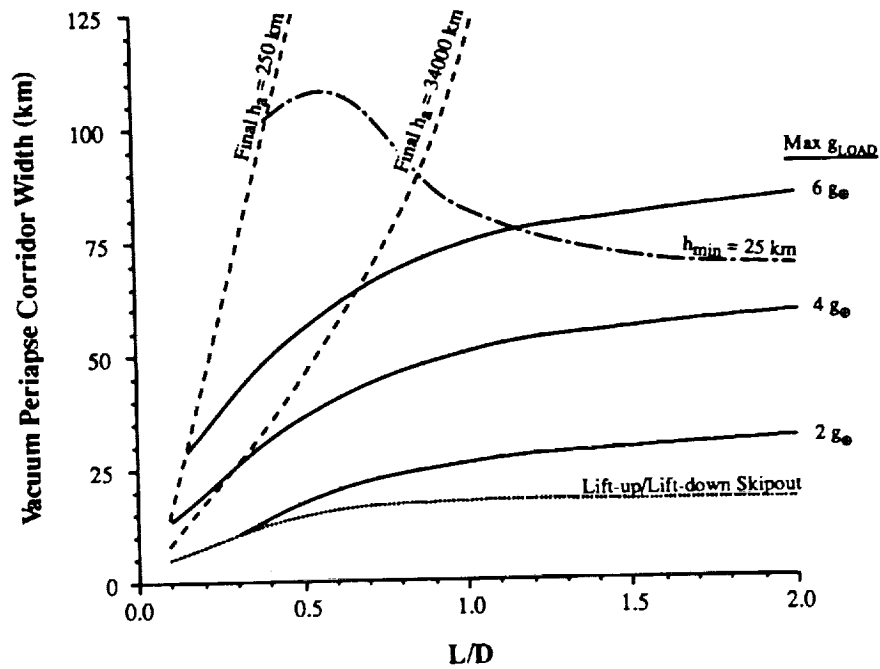


Figure 3-28. Mars  $V_{\infty} = 4.71$  km/s with nominal atmosphere.



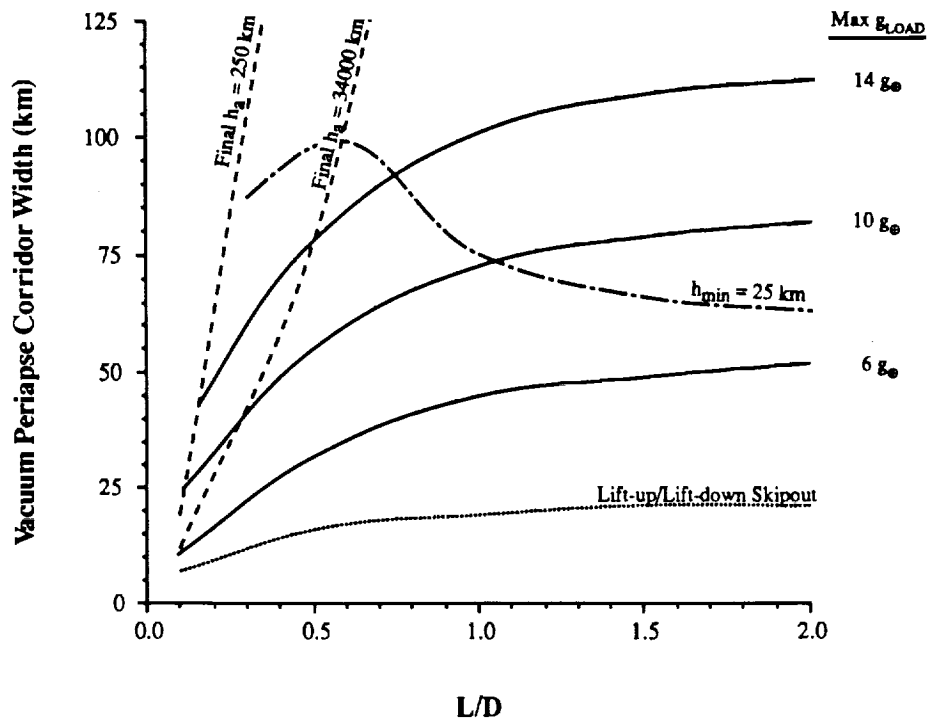


Figure 3-29. Mars:  $V_{\infty} = 6.97$  km/s with nominal atmosphere.

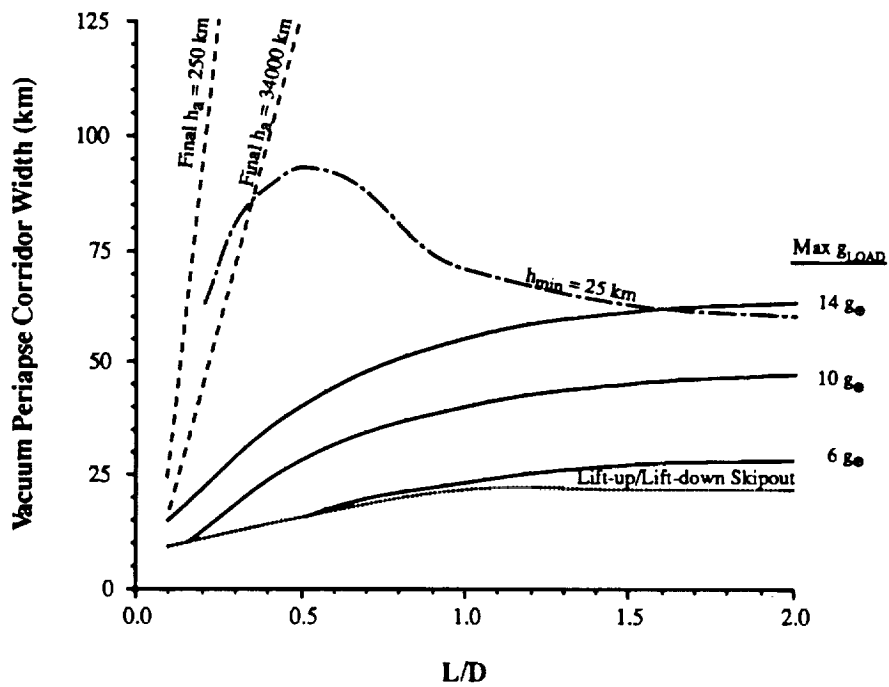


Figure 3-30. Mars:  $V_{\infty} = 10$  km/s with nominal atmosphere.

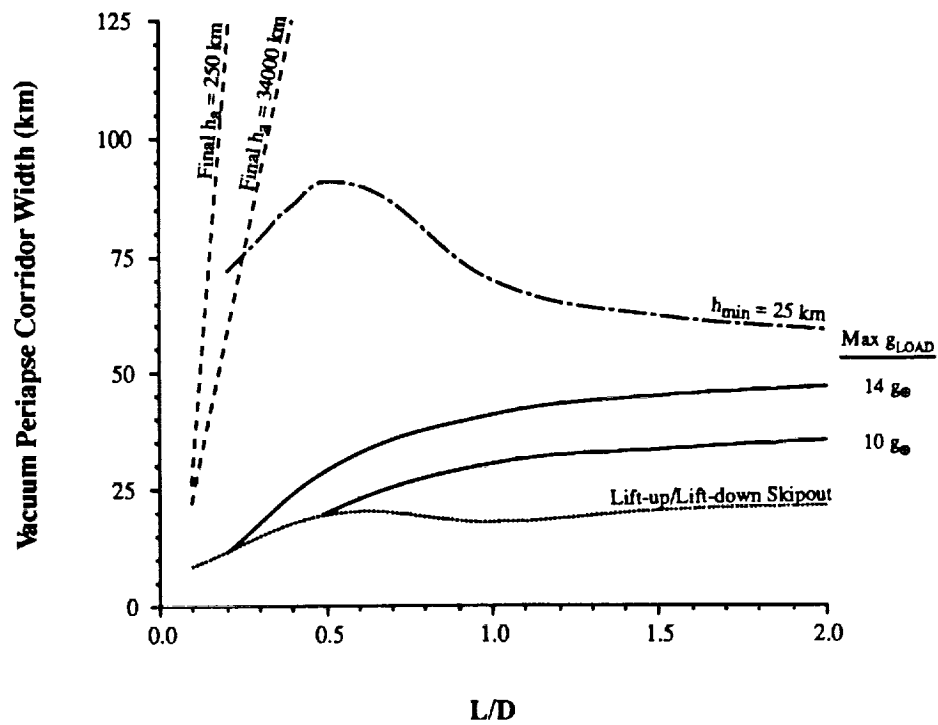


Figure 3-31. Mars:  $V_{\infty} = 12$  km/s with nominal atmosphere.

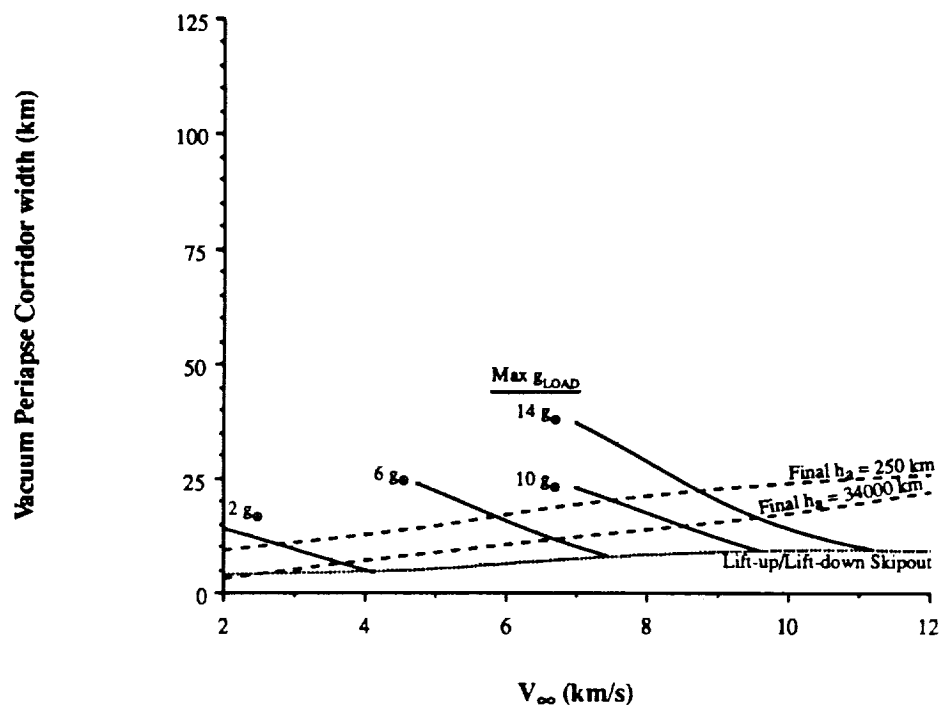


Figure 3-32. Mars:  $L/D = 0.1$  with nominal atmosphere.

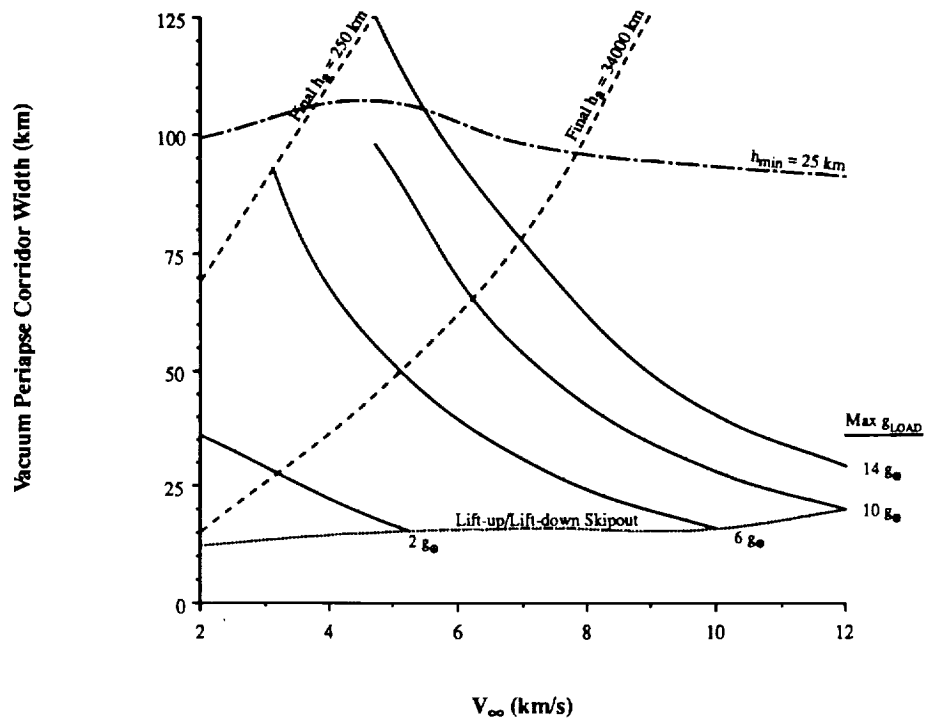


Figure 3-33. Mars:  $L/D = 0.5$  with nominal atmosphere.

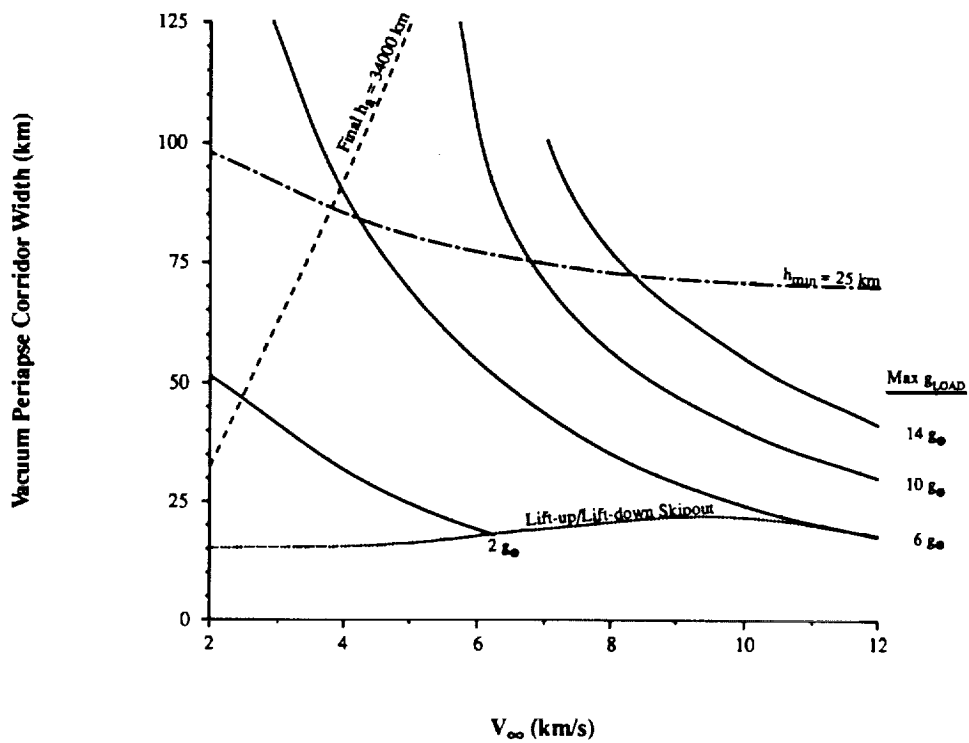


Figure 3-34. Mars:  $L/D = 1.0$  with nominal atmosphere.

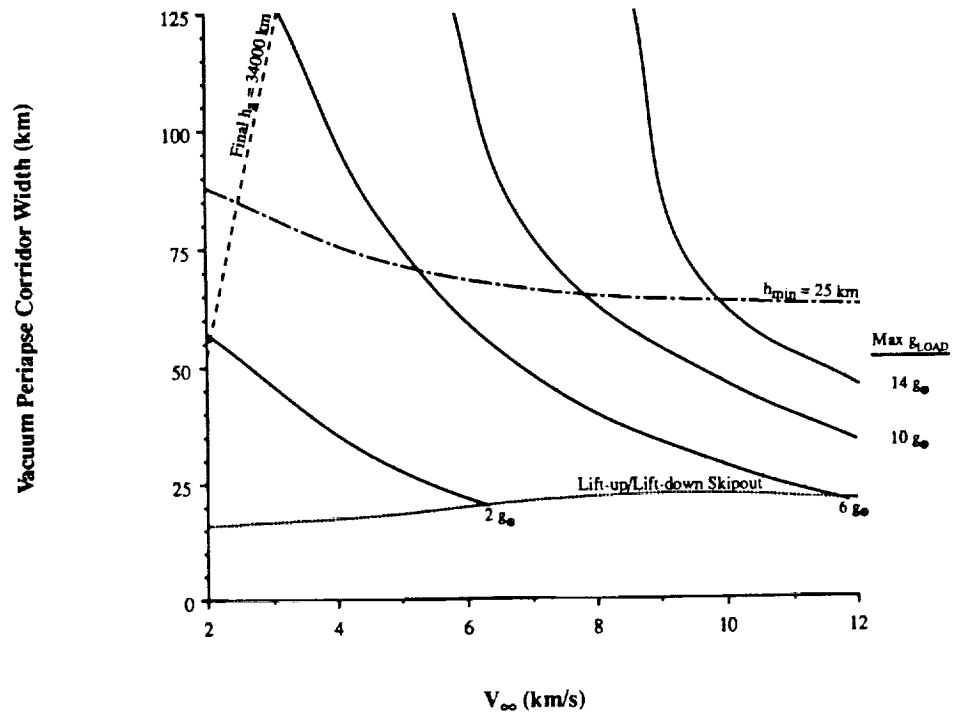


Figure 3-35. Mars:  $L/D = 1.5$  with nominal atmosphere.

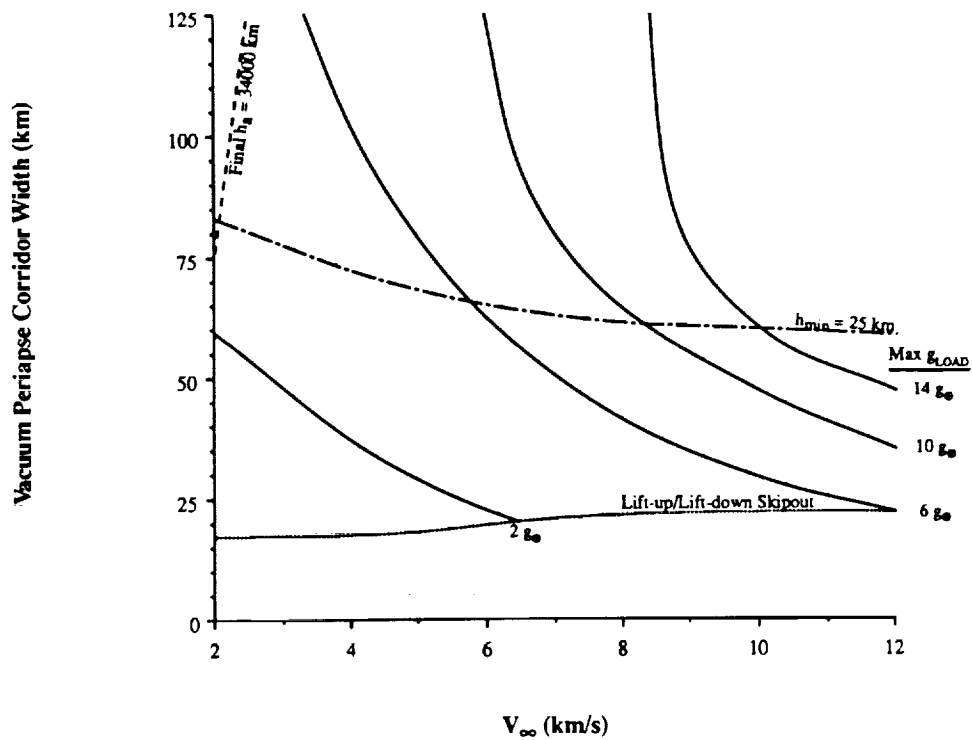


Figure 3-36. Mars:  $L/D = 2.0$  with nominal atmosphere.

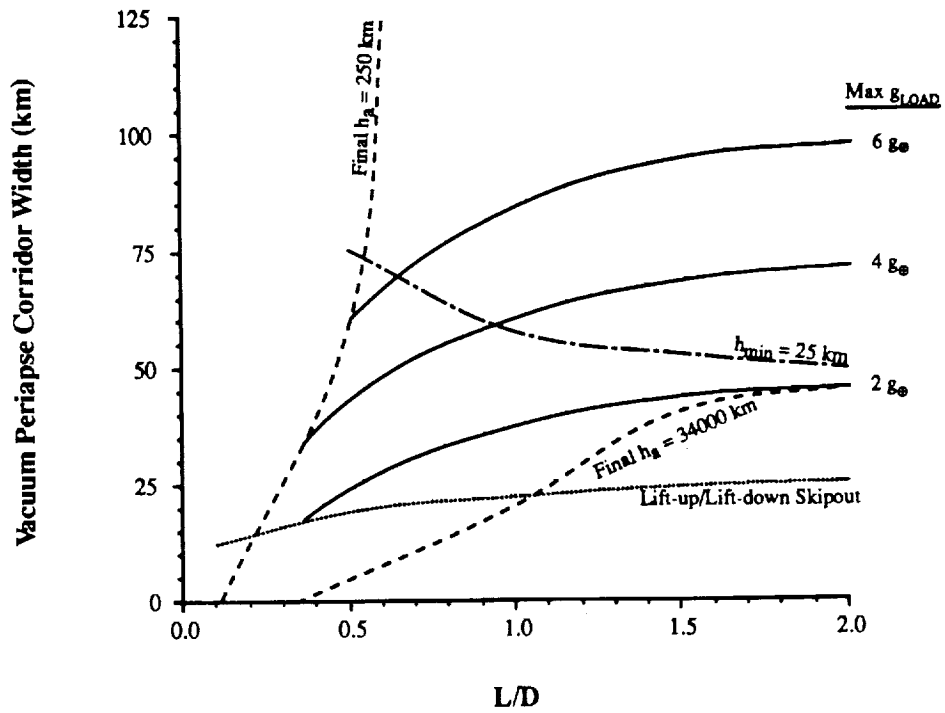


Figure 3-37. Mars:  $V_{\infty} = 2$  km/s with +100 percent and -50 percent atmosphere dispersions.

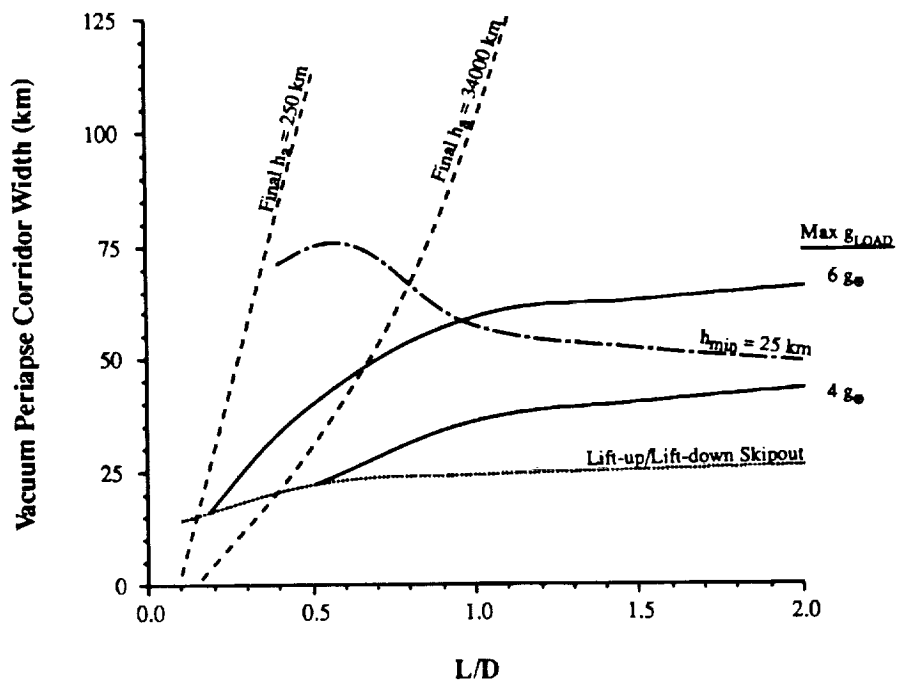


Figure 3-38. Mars:  $V_{\infty} = 4.71$  km/s with +100 percent and -50 percent atmosphere dispersions.

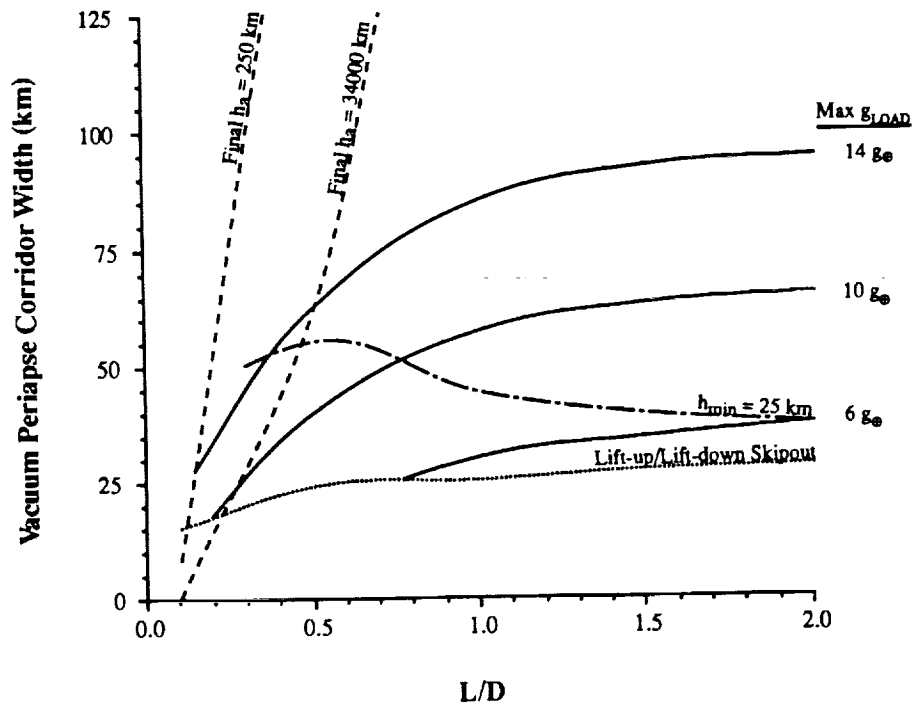


Figure 3-39. Mars:  $V_{\infty} = 6.97$  km/s with +100 percent and -50 percent atmosphere dispersions.

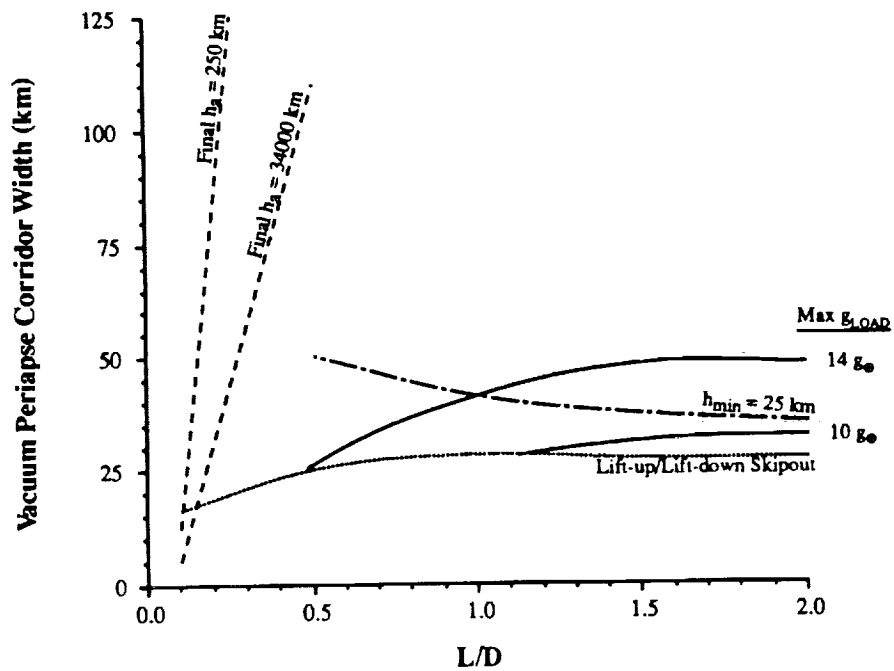


Figure 3-40. Mars  $V_{\infty} = 10$  km/s with +100 percent and -50 percent atmosphere dispersions.

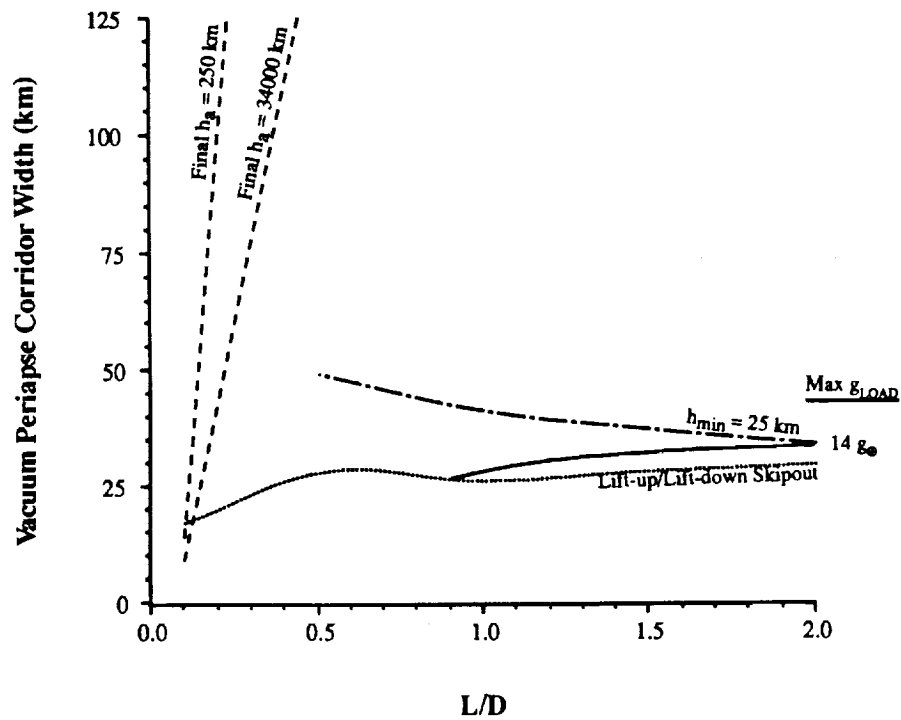


Figure 3-41. Mars:  $V_{\infty} = 12$  km/s with +100 percent and -50 percent atmosphere dispersions.

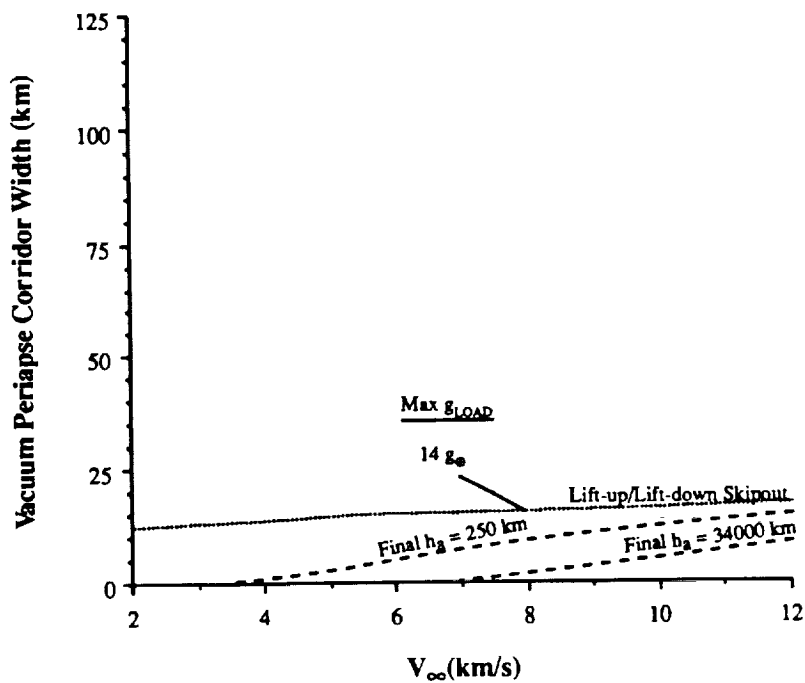


Figure 3-42. Mars:  $L/D = 0.1$  with +100 percent and -50 percent atmosphere dispersions.

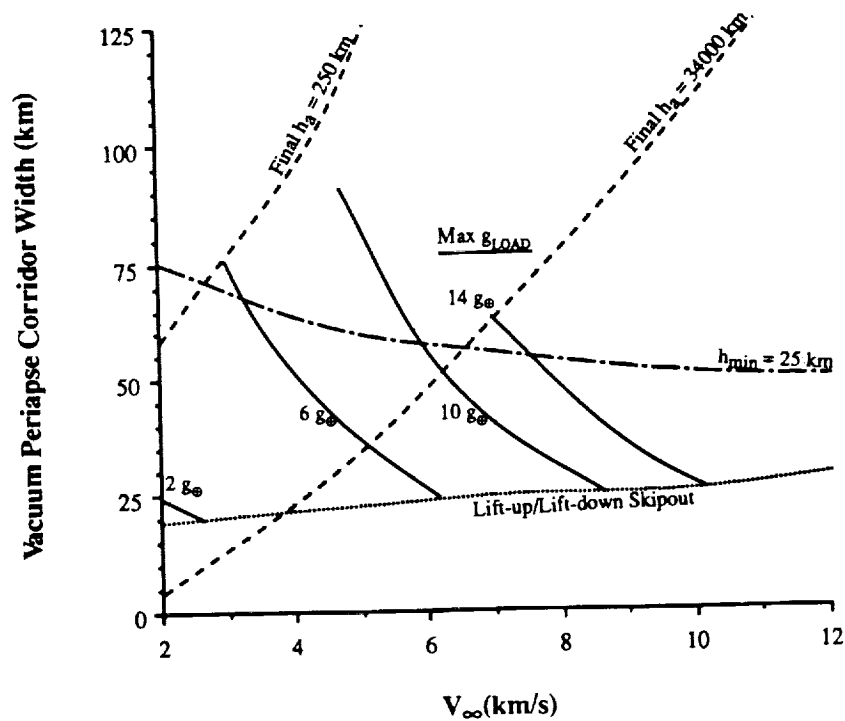


Figure 3-43. Mars:  $L/D = 0.5$  with +100 percent and -50 percent atmosphere dispersions.

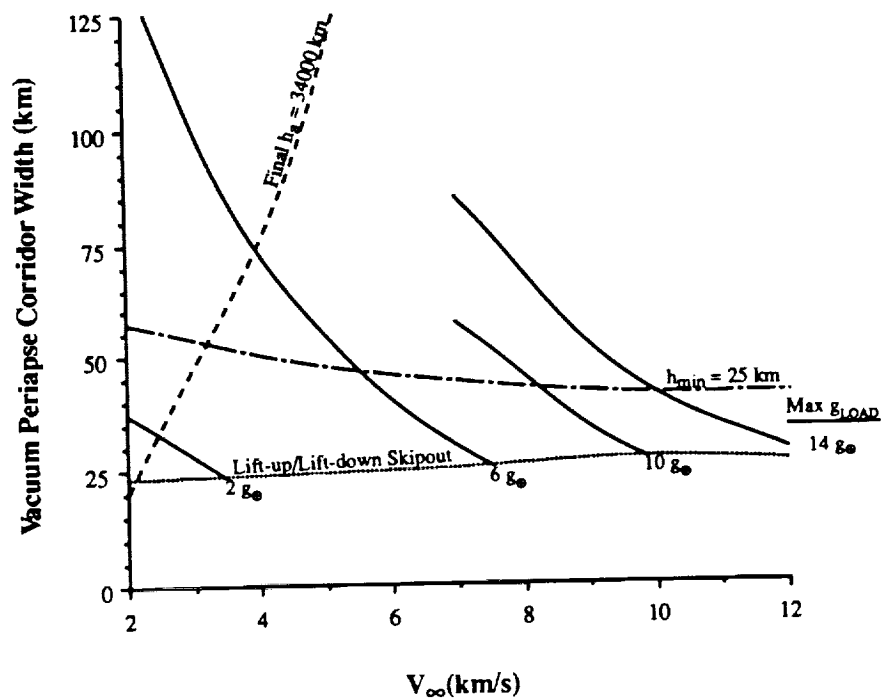


Figure 3-44. Mars:  $L/D = 1.0$  with +100 percent and -50 percent atmosphere dispersions.



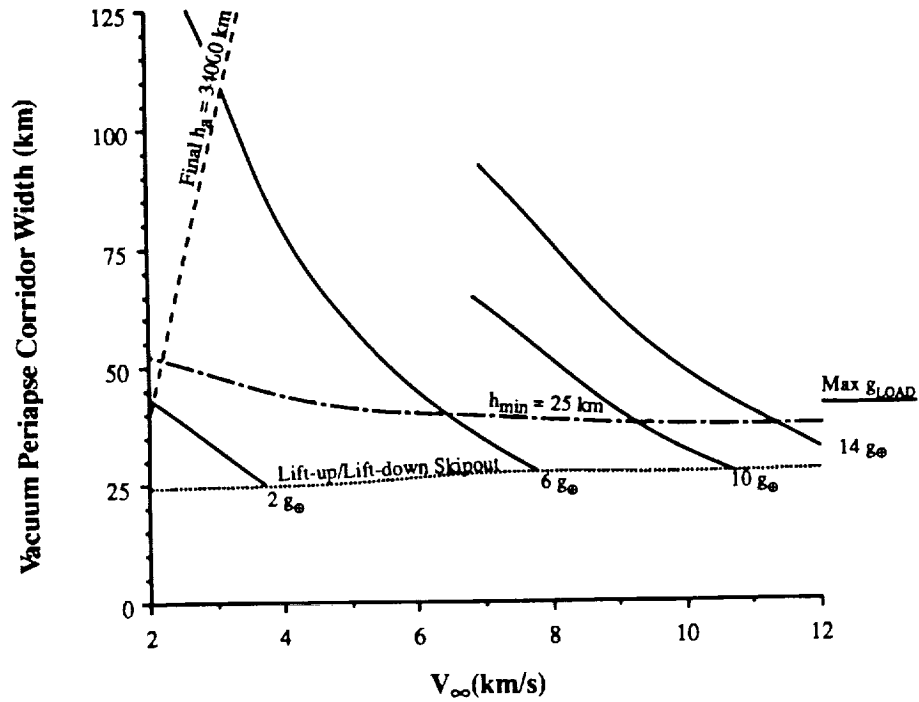


Figure 3-45. Mars:  $L/D = 1.5$  with +100 percent and -50 percent atmosphere dispersions.

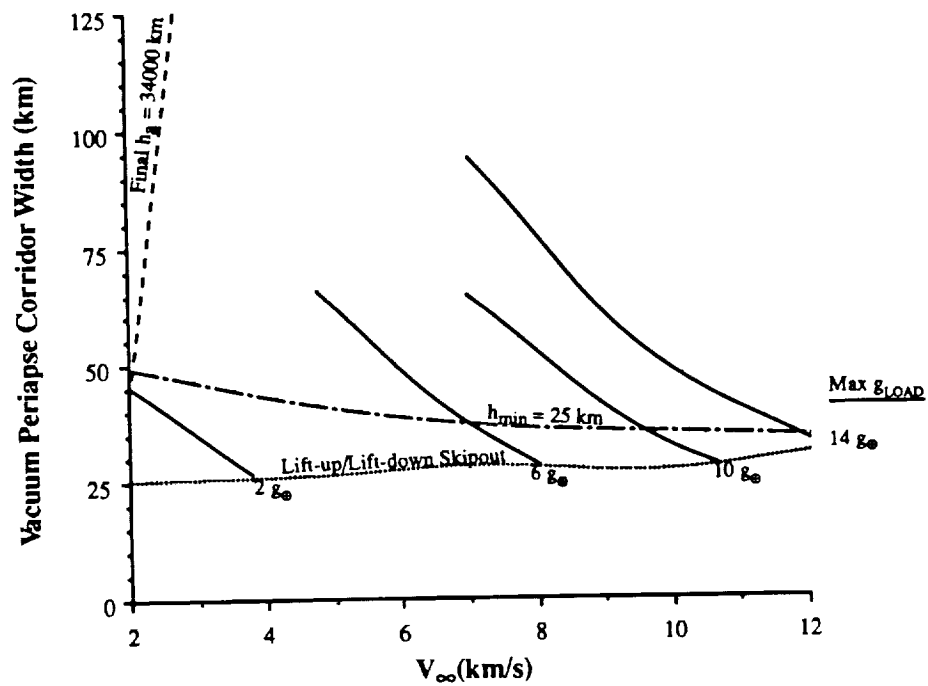


Figure 3-46. Mars:  $L/D = 2.0$  with +100 percent and -50 percent atmosphere dispersions.

# Mars

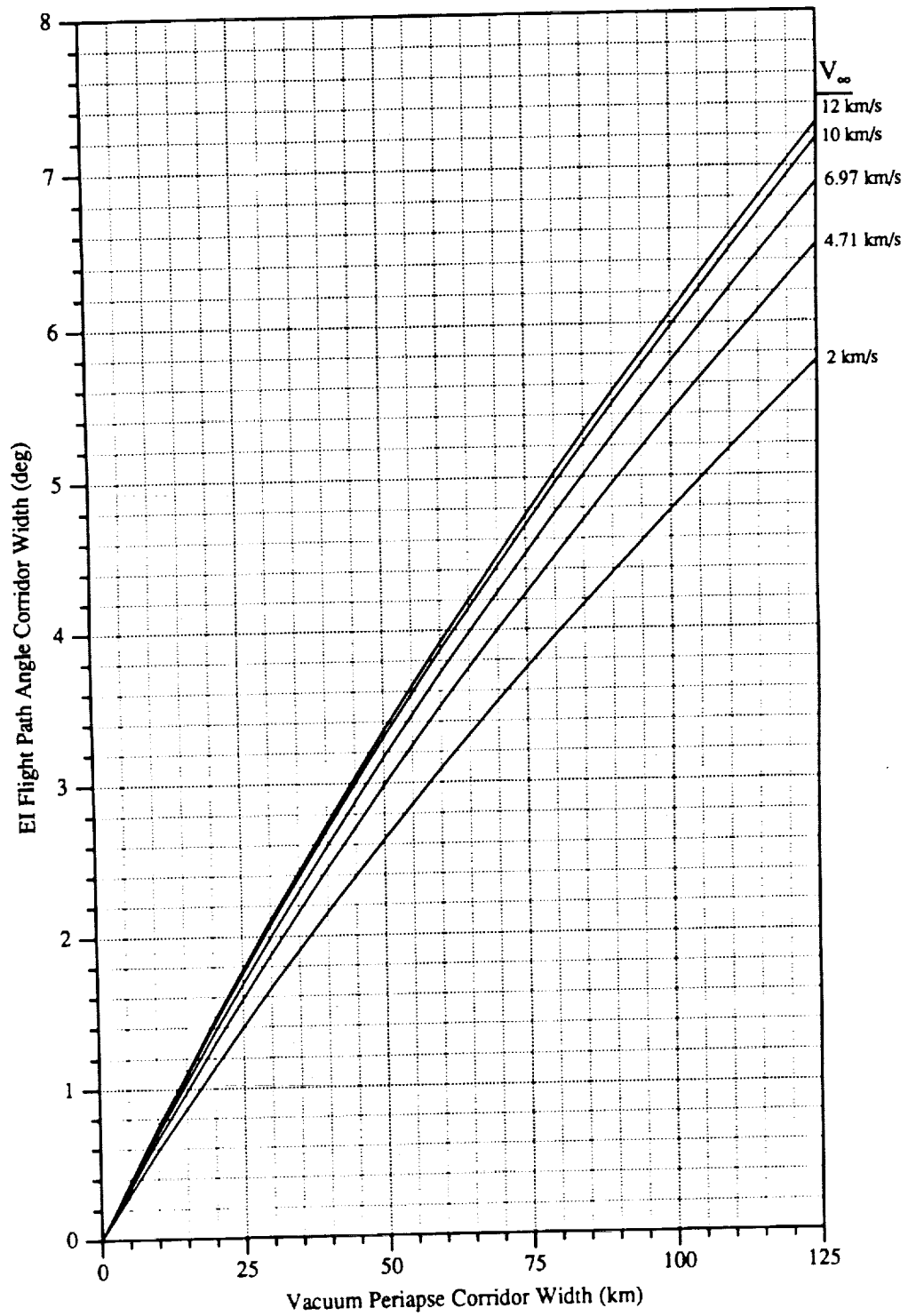


Figure 3-47. Mars: Vacuum periapse corridor width to EI flight path angle corridor width conversion chart.

## SECTION 4 CONCLUSIONS

A matrix of vacuum periapse corridors was determined for a wide range of manned and robotic vehicle constraints and mission requirements. Table 4-I summarizes the trend in the variations of the entry corridor widths to the mission constraints and requirements determined from the analyses in this report. The major results of this analyses are as follows:

- a. Vehicle corridor width increases with increasing vehicle  $L/D$ . This trend has greatest sensitivity with low vehicle  $L/D$  and decreases with higher  $L/D$  ( $> 1$ ). This is due to the contribution of lift acceleration to the total vehicle acceleration determining the steep-side corridor boundary.
- b. Increasing hyperbolic excess velocity ( $V_\infty$ ) decreases the available corridor width. This is because a neighboring trajectory that requires additional energy loss must target slightly steeper on the lift-up steep corridor boundary and will thus reach the g-load constraint boundary more quickly.
- c. An increase in the vehicle g-load limit results in an increased entry corridor. A greater g-load limit allows the vehicle to fly a steeper trajectory and therefore increases the corridor width.
- d. An entry corridor is decreased with margin for density bias where the upper boundary of the light atmosphere corridor and the lower boundary of the heavy atmosphere corridor are used to calculate the actual corridor width.
- e. An entry corridor is decreased with increasing exit orbit energy. The variation of the corridor width to exit orbit energy can be determined by examining the exit apoapse altitude curves on the plots since higher exit apoapse altitudes will yield exit orbits with higher energy. The upper boundary of the corridor is affected only slightly by the exit target altitude. For the lower boundary of the corridor, a lower exit target altitude allows a steeper trajectory to be flown and thus increases the corridor.
- f. Changes in the vehicle  $C_B$  have only slight effects on the entry corridor widths. An increase in the vehicle  $C_B$  slightly increased the corridor width in most of the cases analyzed. However, there were a few exceptions where an increase in the vehicle  $C_B$  actually decreased the corridor width. An increase in  $C_B$  can be caused by a decrease in  $C_D$ . This will result in a decrease in the drag acceleration which reduces the g-load.
- g. Additional constraints such as constraints in the minimum altitude, heating, or apsidal rotation may reduce the width of the entry corridor. The corridor width is reduced if the added constraint is violated before violating other constraints such as the g-load constraint.

TABLE 4-I. VARIATIONS IN ENTRY CORRIDOR WIDTH DUE TO INCREASED MISSION CONSTRAINTS AND REQUIREMENTS

Mission Constraints and Requirements (Parameters are increasing)	Variations in Entry Corridor Widths
L/D	↑
$V_{\infty}$	↓
g-load limit	↑
Atmosphere dispersion	↓
Exit orbit energy	↓
$C_B$	negligible
Minimum altitude constraint	↓
Heating constraint	↓
Rotation of line-of-apsides constraint	↓

Note: ↑ denotes an increase; ↓ denotes a decrease.

## SECTION 5 REFERENCES

1. Kliore, A., ed.: The Mars Reference Atmosphere. COSPAR, 1978.
2. Gamble, J. D.: JSC Pre-Phase A Study: Mars Rover Sample Return Mission Aerocapture, Entry, and Landing Element. JSC-23230, May 1, 1989.
3. Mars Rover/Sample Return (MRSR) Program Aerocapture, Entry, and Landing Conceptual Study Final Report. Lockheed Missiles & Space Company, Inc., Sunnyvale, California, 1988.
4. Gamber, R. T.: Mars Rover Sample Return (MRSR) Program Aerocapture, Entry, and Landing (AEL) Conceptual Study (Final Report). Martin Marietta Aerospace Group, Space Systems, Denver, Colorado, Sept. 1988.
5. Langan, M., et al.: Lunar and Mars Conceptual Flight Description: 90-Day Study Emplacement Phase Flights (Version 1.0). JSC-24433, Aug. 1990.
6. Ried, Robert C., et al.: Human Transportation Systems for Lunar/Mars Outposts: Initial Engineering Considerations. JSC-24155, May 1990.



## APPENDIX A

### USE OF AEROCAPTURE CORRIDORS AS A CONSTRAINT FOR APPROACH NAVIGATION

Errors in the planetary approach trajectory can have a significant impact on aerocapture performance. Trajectory errors imply that the vehicle is not precisely following the desired approach path and must compensate in some manner during the aeropass to assure successful aerocapture. There are two types of trajectory errors which will be present: known (or control) errors and unknown (or navigation) errors. Known errors are dispersions of which the onboard guidance and navigation systems are aware. These errors are easily compensated for if small enough since early action can be taken during the aeropass to lessen their impact. Navigation errors are errors in the knowledge of the trajectory; that is, the onboard guidance and navigation systems are unaware that the vehicle is on the incorrect approach path. As may be expected, aerocapture performance is much more sensitive to unknown errors than known errors since in this case trajectory control commands are based on erroneous estimates of the vehicle state. It is therefore very important to understand the sensitivity of the performance to these errors and ensure that planetary approach navigation is accurate enough to meet requirements.

Previous studies have examined the impact of in-plane navigation errors at atmospheric entry interface (EI) on aerocapture performance for use in the development of planetary approach navigation accuracy requirements at Mars.<sup>7</sup> The results of this study indicate that the approach navigation accuracy requirements problem is multidimensional; that is, the required navigation accuracy at EI must be specified as more than a one-dimensional parameter (such as vacuum periapse altitude error or EI flight path angle error). Note that this is different from the known error case, where the one-dimensional specification of vacuum periapse altitude or EI flight path angle is adequate. (The periapse corridors in this paper essentially show the tolerable range of known periapse altitude error variation.) Figure A-1, reproduced from reference 7 is an example of the full specification of an EI in-plane navigation accuracy requirements envelope for a specific mission and vehicle design. Note that in this case the requirements specification reduces from four (two position error components and two velocity error components) to two dimensions because of extremely strong correlations between state error components due to approach navigation. Superimposed upon the plot of figure A-1 are dashed lines representing constant unknown approach vacuum periapse altitude errors. Mapped onto the requirements envelope are two ellipsoids indicating the 3 $\sigma$  performance of an onboard optical navigation system utilizing line-of-sight measurements of the martian moon Deimos for two different cases. Plainly stated, if the navigation performance ellipsoid for a given scenario lies within the requirements envelope, then the navigation accuracy requirements are satisfied for all possible cases and the navigation performance is adequate. If the navigation performance ellipsoid extends outside of the envelope, then failed aerocapture will occur in those cases lying in the region external to the envelope.

Essentially, then, this means that the corridor width data presented in this paper cannot be used for the complete specification of navigation accuracy requirements or, alternatively, to determine if a given vehicle design provides sufficient capability to cover expected navigation errors resulting from a given approach navigation scheme. The one-dimensional aerocapture corridor data presented here can, however, be used to gain insight into the adequacy of a given approach navigation scheme and even bound the minimum accuracy required. For each navigation performance ellipsoid in figure A-1, there is a corresponding 3 $\sigma$  vacuum periapse altitude navigation error defined by the constant periapse altitude error lines. (For instance, the 3 $\sigma$  error for the "Deimos Worst Phasing" case in figure A-1 is  $\pm 20$  km.) This periapse altitude navigation error range can be compared with the vacuum periapse corridor width (as defined in this paper) for the given case. While we cannot state that the navigation accuracy requirements are fully satisfied if this range is less than the corridor width (remember that this is a multidimensional problem), we can say that the navigation

performance is inadequate if the error range is larger than the corridor width. In other words, if the error range is larger than the corridor width, there can potentially be navigation errors which place the actual approach trajectory outside of the corridor, thereby rendering it unflyable. Thus, in the specification of the aerocapture vacuum periapse corridor width we have in essence an upper bound on the allowable navigation uncertainty in this parameter.

An example should help to illustrate this concept. Figure A-2 shows some specific examples of Mars approach navigation performance based on the results seen in reference 7. The uncertainty in vacuum periapse altitude at EI is shown for three different scenarios: Deep Space Network (DSN) tracking terminating at 2 days prior to EI (see ref. 8 for further DSN performance study results), DSN tracking supplemented by onboard optical measurements of the line-of-sight to the moon Deimos starting 2 days prior to EI, and DSN tracking supplemented by onboard radio metric measurements with respect to an aerosynchronous Mars satellite starting 2 days prior to EI. The range of accuracies shown for the optical and radio measurement scenarios indicates the range of performance predicted based on varying measurement schedules, types, and accuracy assumptions. The accuracies predicted in this study range from approximately  $\pm 1$  km for the best-case radio metric navigation scenario to  $\pm 41$  km for the DSN-only scenario.

Consider a mission design which has an approach  $V_{\infty}$  of 6.97 km/s, a  $g_{LOAD}$  limit of  $6 g_0$ , and a vehicle  $L/D$  of 0.7. The vacuum periapse corridor width for this case is approximately 40 km (see fig. 3-29). Therefore, the selected approach navigation scheme must have an accuracy of at least  $\pm 20$  km in periapse altitude to prevent trajectories which lie outside the corridor limits. Thus, for this case, DSN tracking ( $\pm 41$  km accuracy) would definitely be inadequate, while the best-case optical measurement scenario ( $\pm 6$  km accuracy) may be adequate, depending on the results of a full-dimensional navigation accuracy requirements analysis.

## REFERENCES

7. Spratlin, K. M., et al: 1989 Lunar/Mars Initiative guidance, Navigation & Control Final Report. CSDL-P-2932, The Charles Stark Draper Laboratory, Inc., Cambridge, Massachusetts, Feb. 1990.
8. Konopliv, A.; and Wood, L.: High-Accuracy Mars Approach Navigation with Radio Metric and Optical Data. AIAA/AAS Astrodynamics Conference, AIAA paper AIAA-90-2907 (Portland, Oregon), Aug. 20-22, 1990.



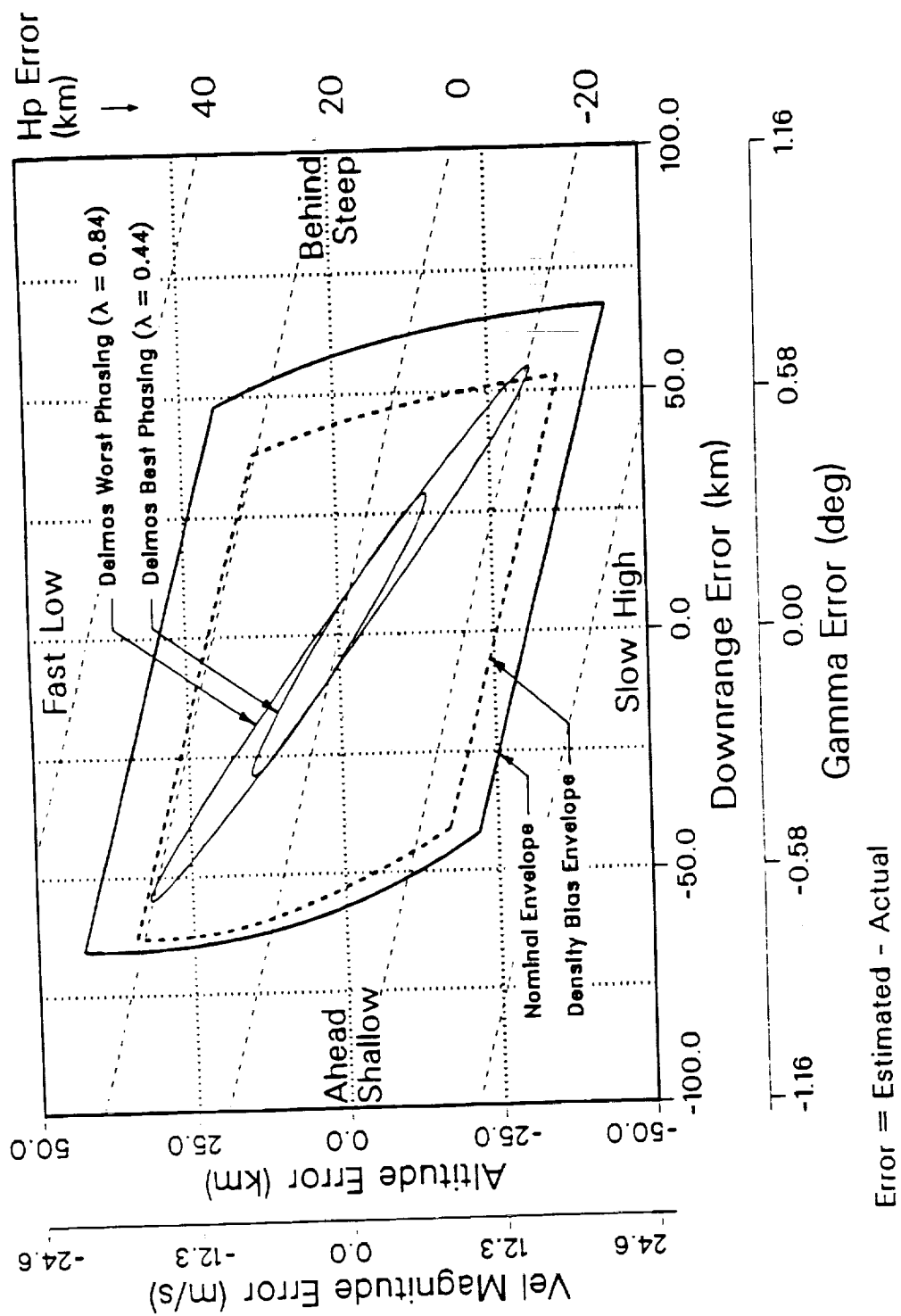


Figure A-1. Optical navigation performance at E1 (3 $\sigma$ ) - measurements suspended 1 hr prior to E1.

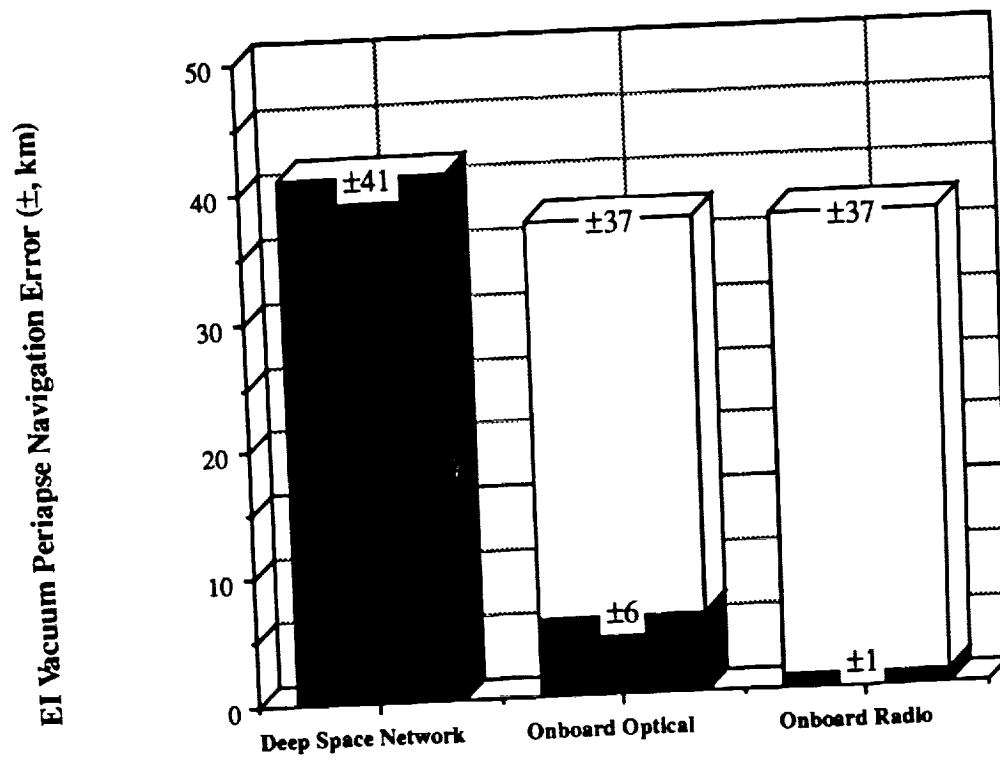


Figure A-2. Examples of Mars approach navigation performance.

## APPENDIX B

### EFFECT OF ADDED CONSTRAINTS ON AEROCAPTURE CORRIDOR WIDTH

The aerocapture corridors shown in this report are basically a function of energy only; that is, the assumption that aerocapture is primarily concerned with the removal of energy from the planetary approach orbit is inherent in the results. The constraints included in the corridor definition (no skip-out, g-load limit, and final apoapse altitude) basically bound the atmospheric entry conditions over which the necessary energy removal can occur assuming full use of the aerodynamic control capability of the vehicle for this purpose. In reality, additional requirements which could necessitate independent control and reduce the amount of vehicle lift available for the primary function of energy removal may be levied on the aerocapture maneuver. These additional requirements may include continuous constraints on the trajectory or additional targets affecting the desired end conditions. Such requirements essentially would decrease the corridor width for a given vehicle lift-to-drag ratio (L/D) or, equivalently, increase the L/D required for a given mission over the value predicted by the data shown in this report.

Aerodynamic heating is an additional factor which may require explicit control during the aeropass. A constraint on heating basically can be broken down into two factors: the maximum heating rate and the total integrated heat load. While the primary factor influencing aerodynamic heating is the vehicle ballistic coefficient (a design parameter), some control over vehicle heating can be obtained by using the lifting capability of the vehicle for trajectory shaping. For example, if minimization of the peak heat rate is desired on a steep trajectory, then a full lift-up trajectory would be flown until the vehicle was past the point of maximum heat rate. The imposition of heating limits may decrease the corridor width by shallowing the lower corridor boundary, and any active heating control will reduce the amount of aerodynamic control capability available for explicit orbital energy control.

Maximum convective heating rate data were generated for the entry corridor boundary trajectories examined for this study. Figures B-1 through B-6 show the maximum convective heating rate experienced on the full lift-up steep corridor boundary trajectory for each of the constraint boundaries examined for the Earth aerocapture cases with nominal atmospheric density, and figures B-7 through B-11 show the equivalent maximum heating rate data for the Mars aerocapture corridor boundary trajectories. (These plots correspond to the corridor width plots in figures 3-2 through 3-7 and 3-27 through 3-31 for Earth and Mars, respectively.) Note that these data essentially represent the maximum convective heating rate experienced over the entire corridor for a given case. Figures B-7 through B-11 also show the maximum convective heating rate experienced on the full lift-down shallow corridor boundary trajectory for each of the Mars cases. The convective heating rate was computed using Chapman's equation:

$$Q_{conv} = \frac{C}{\sqrt{R_n}} \sqrt{\frac{\rho}{\rho_0}} \left( \frac{V_{rel}}{V_c} \right)^m \quad (\text{in units of W/cm}^2)$$

where:

- $R_n$  = vehicle nose radius = 100 cm
- $\rho$  = atmospheric density (kg/m<sup>3</sup>)
- $V_{rel}$  = relative velocity (km/s)
- $\rho_0$  = reference density (kg/m<sup>3</sup>)
- $V_c$  = reference circular velocity (km/s)

For Earth,

$$\begin{aligned}C &= 110\,328 \text{ W/cm}^{3/2} \\ \rho_0 &= 1.226 \text{ kg/m}^3 \\ V_c &= 7.9248 \text{ km/s} \\ m &= 3.15\end{aligned}$$

and for Mars,

$$\begin{aligned}C &= 2853 \text{ W/cm}^{3/2} \\ \rho_0 &= 0.0995 \text{ kg/m}^3 \\ V_c &= 3.5475 \text{ km/s} \\ m &= 3.0\end{aligned}$$

Several observations may be made concerning these data. For a given  $V_\infty$ , there is a large variation in the maximum convective heating rate with entry periape altitude. For example, figure B-2 (Earth,  $V_\infty = 4 \text{ km/s}$ ) indicates that there is a variation of over  $600 \text{ W/cm}^2$  in the maximum heat rate on the lift-up steep corridor boundary trajectory as the  $g_{LOAD}$  limit varies from  $2g_\oplus$  to  $14g_\oplus$  for an  $L/D$  of 2.0. (This corresponds to a steepening of approximately 100 km in the steep corridor boundary vacuum periape altitude). As would be expected, there is also a large variation with  $V_\infty$ . Note that for the Earth data shown, the maximum heating rate varies from under one hundred up to several thousand watts per square centimeter as  $V_\infty$  varies from 1 to 18 km/s (see figs. B-1 and B-6).

The variation in maximum convective heating rate over the entry corridor width for a given case can be observed in figures B-7 through B-11 for Mars aerocapture. Note the significant range of heating which can occur between the shallow full lift-down boundary trajectory and the steep full lift-up boundary trajectory. For example, figure B-9 (Mars,  $V_\infty = 6.97 \text{ km/s}$ ) shows a variation of almost  $400 \text{ W/cm}^2$  between the skipout and  $14g_\oplus$  boundaries for an  $L/D$  of 2.0. These data indicate the significant impact that both vehicle and trajectory designs have on the heating experienced during aerocapture, and the fact that imposition of heating rate constraints may decrease the corridor width for a given design.

Further constraints on the final orbit will also impact the corridor width and, therefore, the required  $L/D$ . Additional targets may include the orientation of the final orbit plane (specified by parameters such as the longitude of the ascending node and inclination) or the orientation of the line-of-apsides in the case of elliptical targets.

Orbit plane orientation control is performed using the out-of-plane component of the lift vector. While minimal out-of-plane lift is required to maintain the orbit plane at the entry interface orientation, substantial additional lift may be necessary if rotation of the orbital plane is nominally required during the aeropass. In this case, the full lifting capability would not be available for energy control since some component of the lift vector would need to be reserved for orbit plane steering. Once again, this would decrease the width of the flyable entry corridor and increase the vehicle  $L/D$  required for a given mission.

In case of elliptical target orbits, control over the final orientation of the line-of-apsides may be required in order to assure proper orbital alignment with respect to the planet surface or the hyperbolic planetary departure orbit asymptote. Substantial rotation of the line-of-apsides can occur due to the aerodynamic forces generated during the aeropass, and correction using propulsive methods is expensive. Figures B-12 and B-13 illustrate the apsidal rotation which occurs during the aeropass in two of the cases examined in this report. The apsidal rotation is shown over the corridor boundary trajectories (i.e., the full lift-down skipout boundary trajectory and the full lift-up max  $g$ -load trajec-

tories) for the  $V_{\infty} = 7.56$  km/s (Earth) and for the  $V_{\infty} = 10$  km/s (Mars) cases. For these cases, rotations of up to approximately  $20^\circ$  are seen. Since apsidal rotation is closely tied to the vertical (or in-plane) component of the lift vector, active control of this parameter could seriously detract from the control authority available for orbital energy control.

In a similar manner, other constraints and requirements levied on the aerocapture maneuver will increase vehicle L/D requirements over those shown in this report. While the corridor data presented here provide a preliminary mission design and evaluation tool, final determination of corridor width and vehicle performance requirements needs to take into account any additional mission requirements and constraints which impact performance.

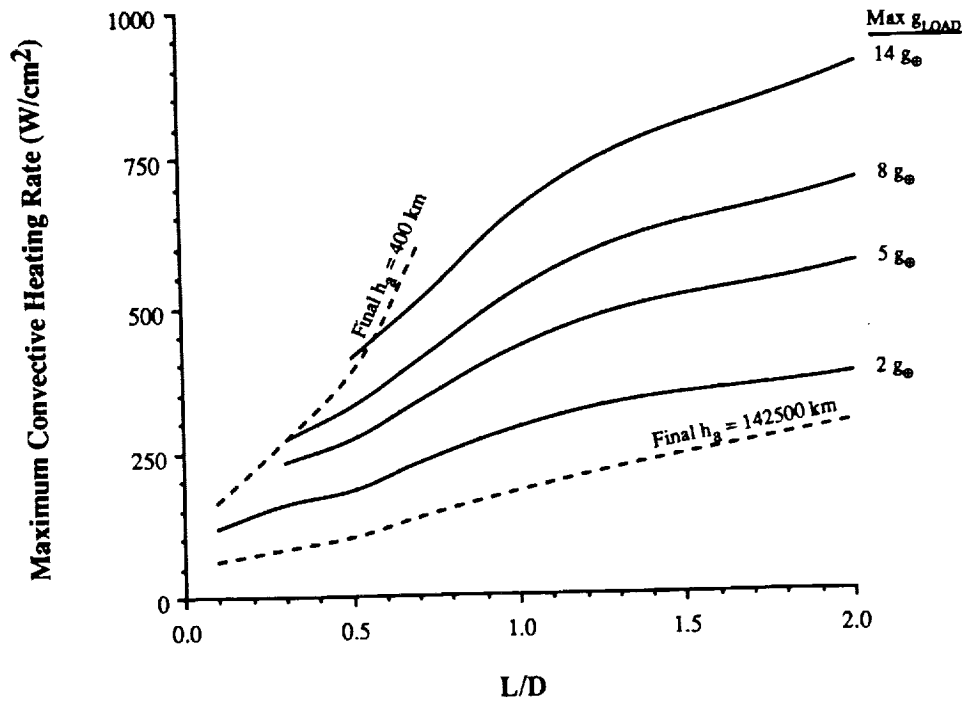


Figure B-1. Earth: Maximum convective heating rate for  $V_\infty = 1$  km/s.

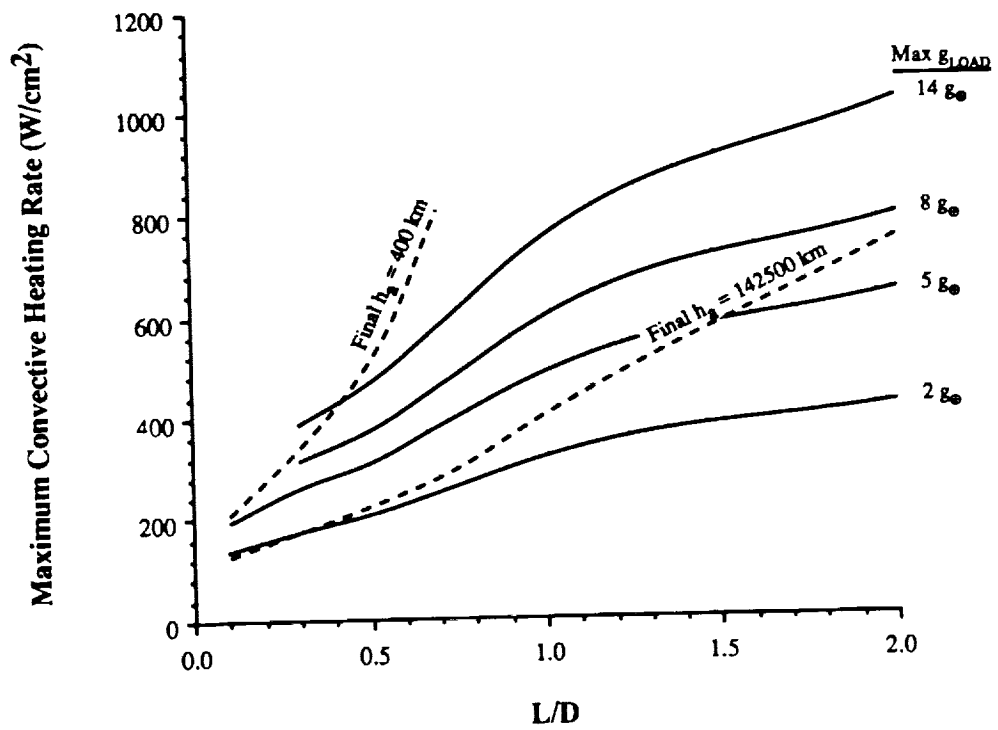


Figure B-2. Earth: Maximum convective heating rate for  $V_\infty = 4$  km/s.

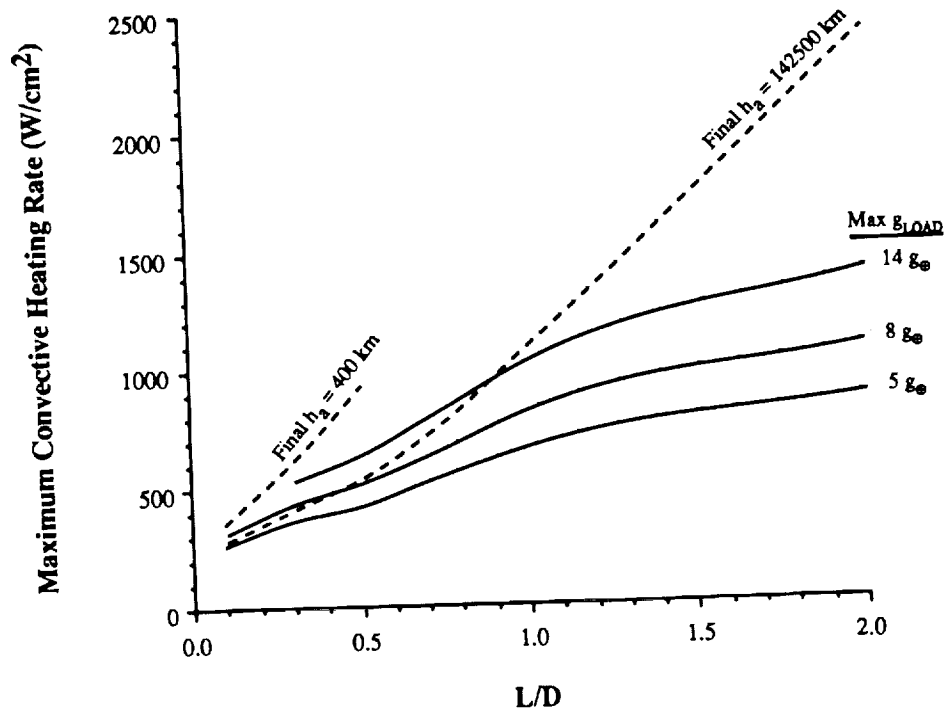


Figure B-3. Earth: Maximum convective heating rate for  $V_\infty = 7.56 \text{ km/s}$ .

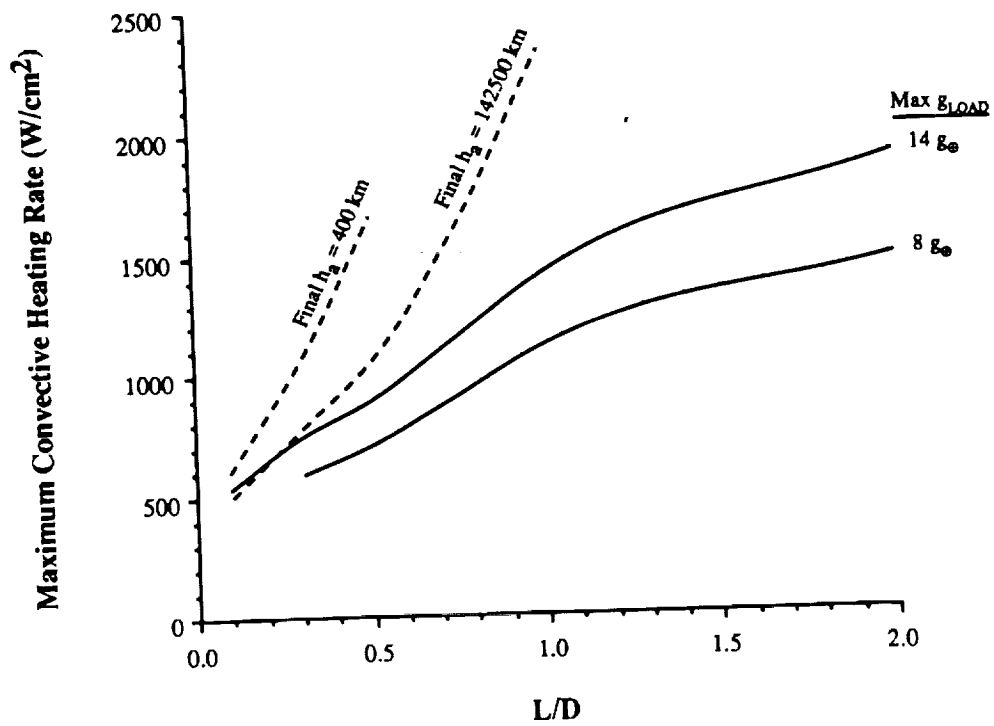


Figure B-4. Earth: Maximum convective heating rate for  $V_\infty = 10.61 \text{ km/s}$ .

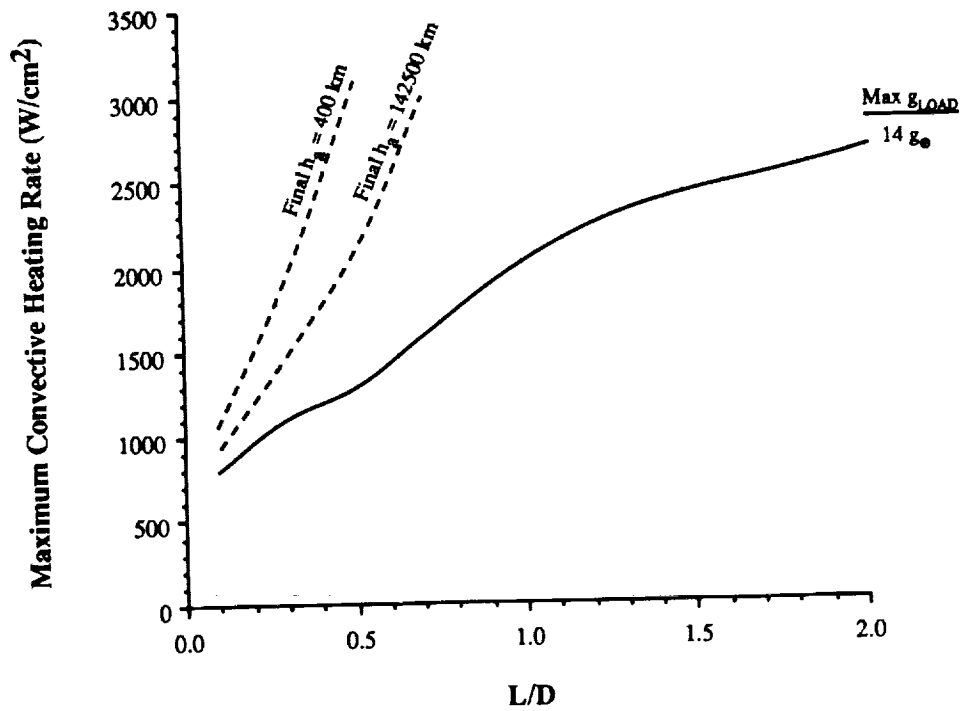


Figure B-5. Earth: Maximum convective heating rate for  $V_\infty = 14$  km/s.

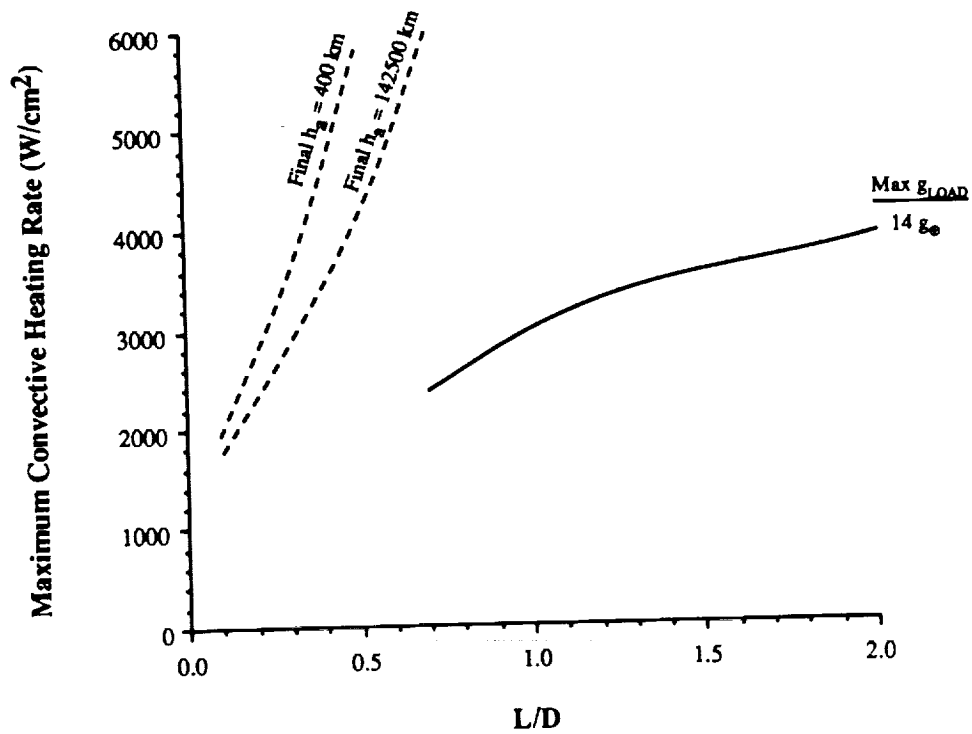


Figure B-6. Earth: Maximum convective heating rate for  $V_\infty = 18$  km/s.



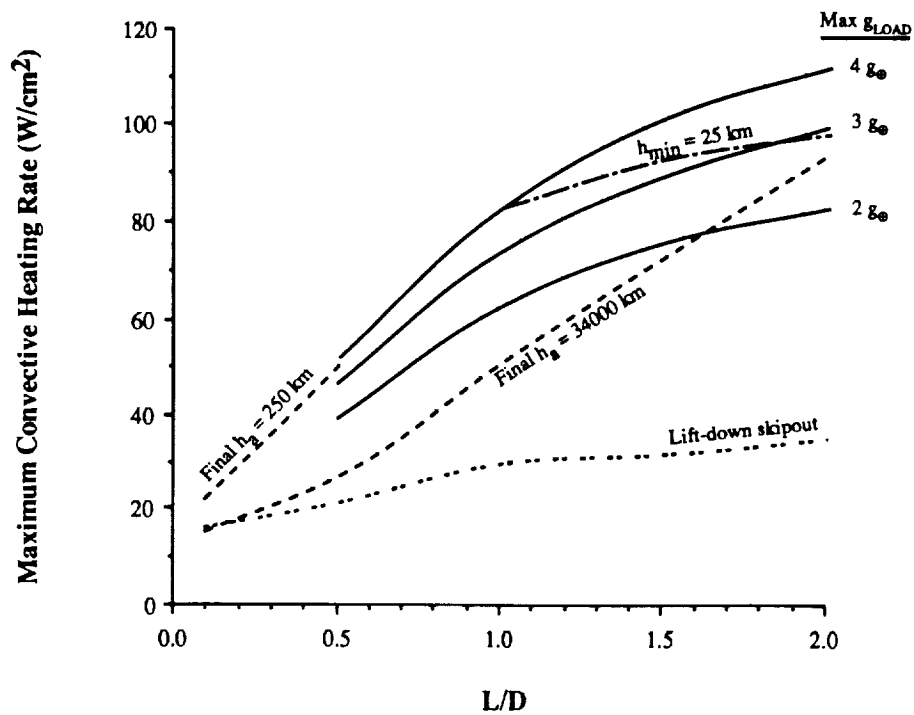


Figure B-7. Mars: Maximum convective heating rate for  $V_{\infty} = 2$  km/s.

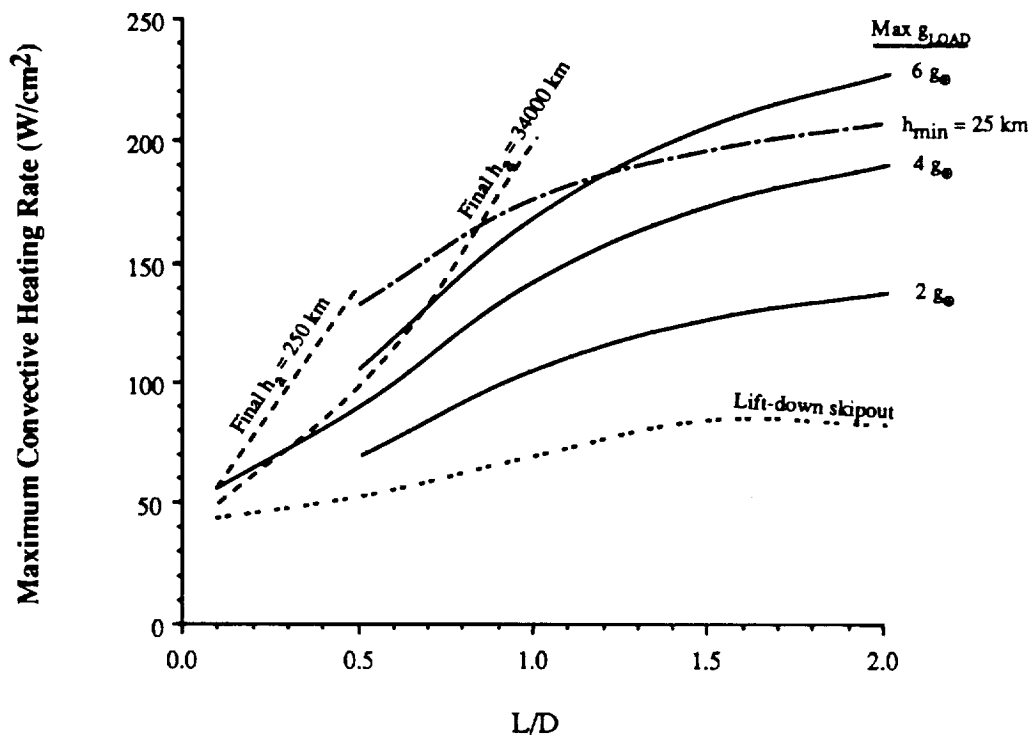


Figure B-8. Mars: Maximum convective heating rate for  $V_{\infty} = 4.71$  km/s.

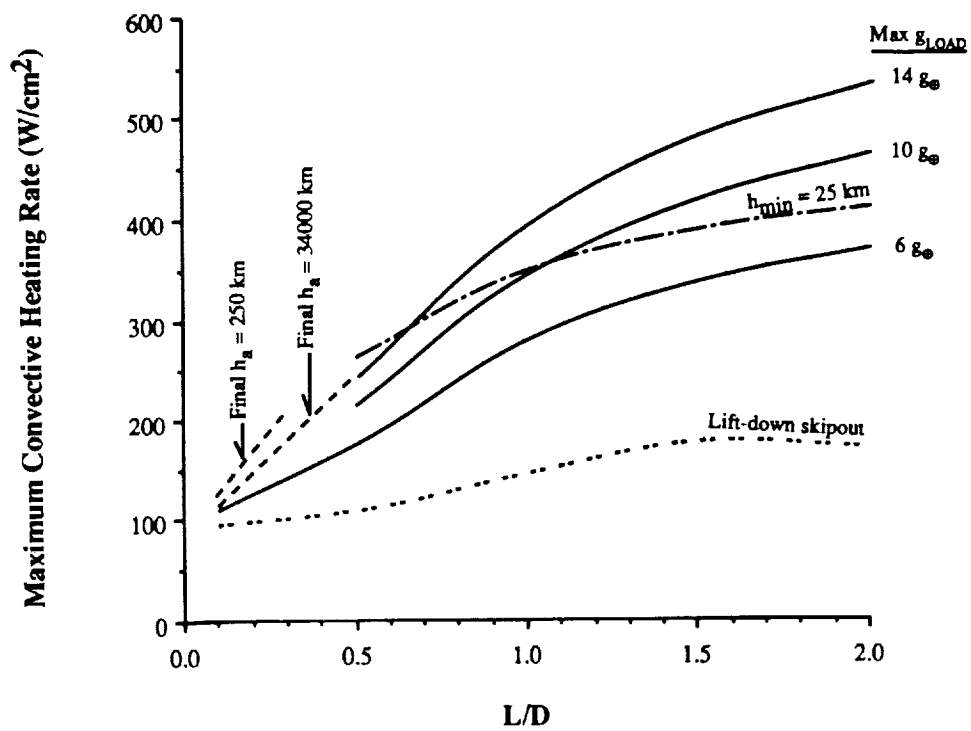


Figure B-9. Mars: Maximum convective heating rate for  $V_\infty = 6.97$  km/s.

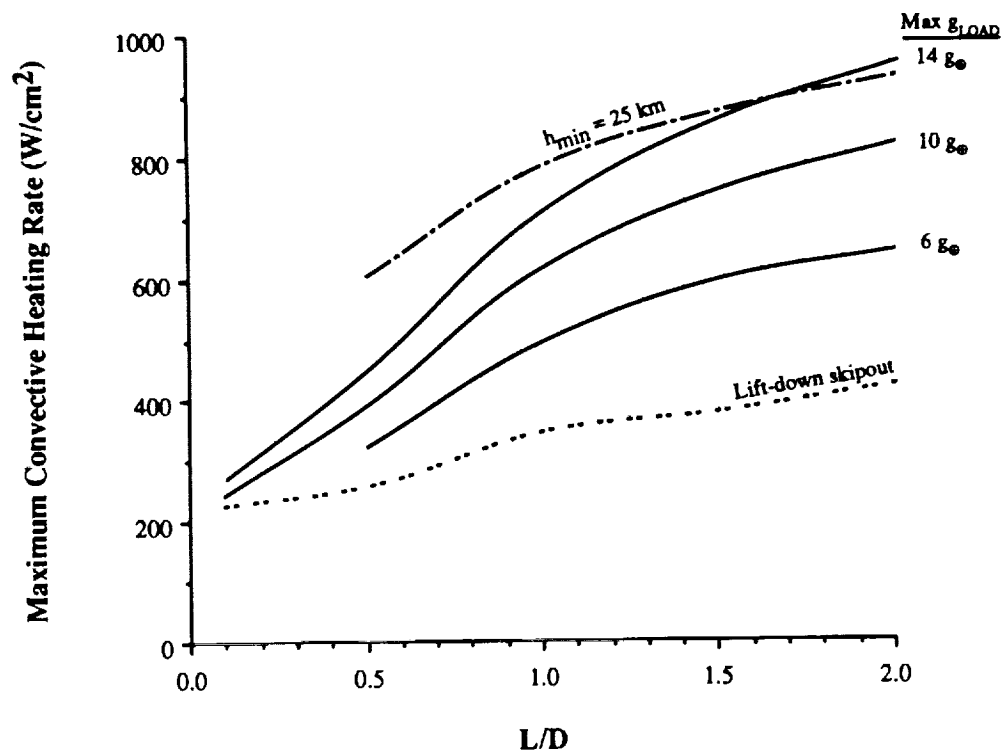


Figure B-10. Mars: Maximum convective heating rate for  $V_\infty = 10$  km/s.

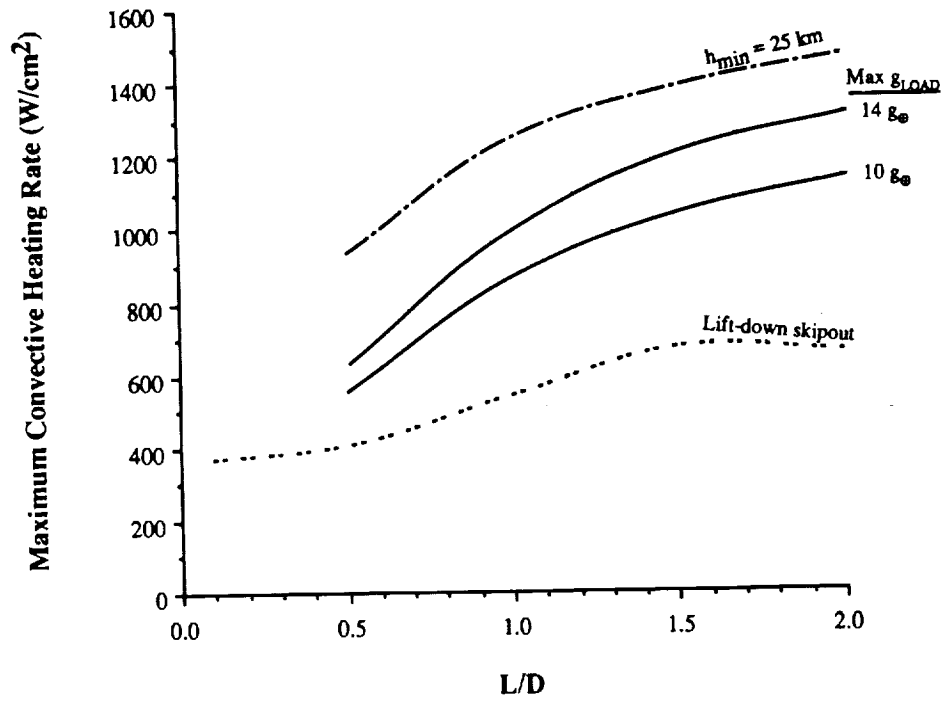


Figure B-11. Mars: Maximum convective heating rate for  $V_{\infty} = 12$  km/s.

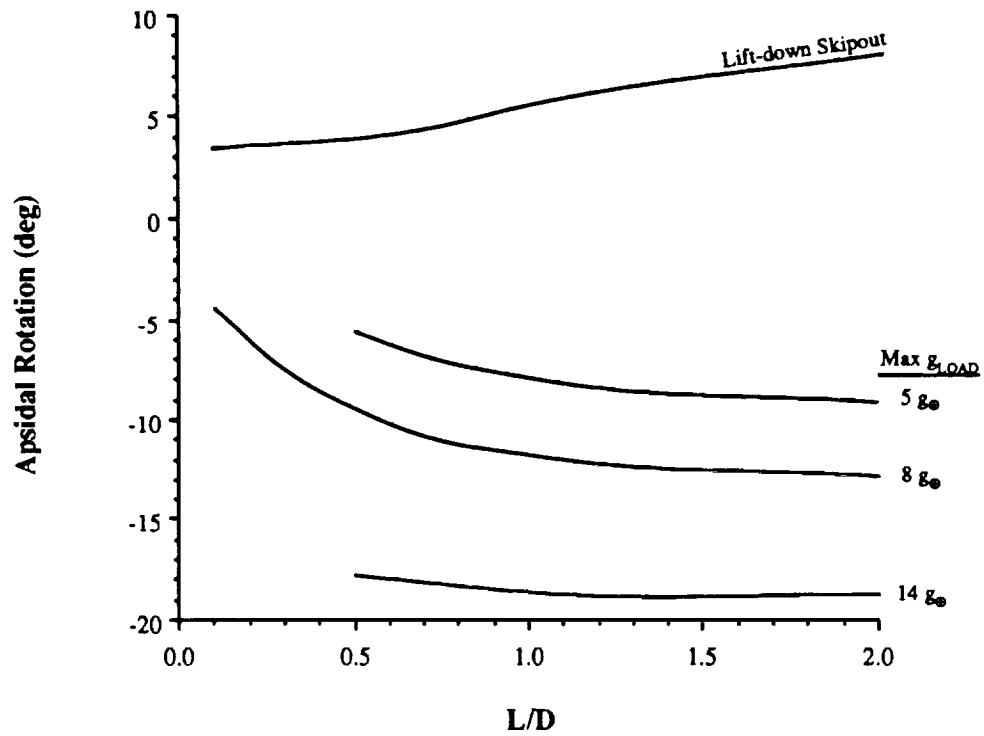


Figure B-12. Earth: Apsidal rotation for  $V_{\infty} = 7.56$  km/s.

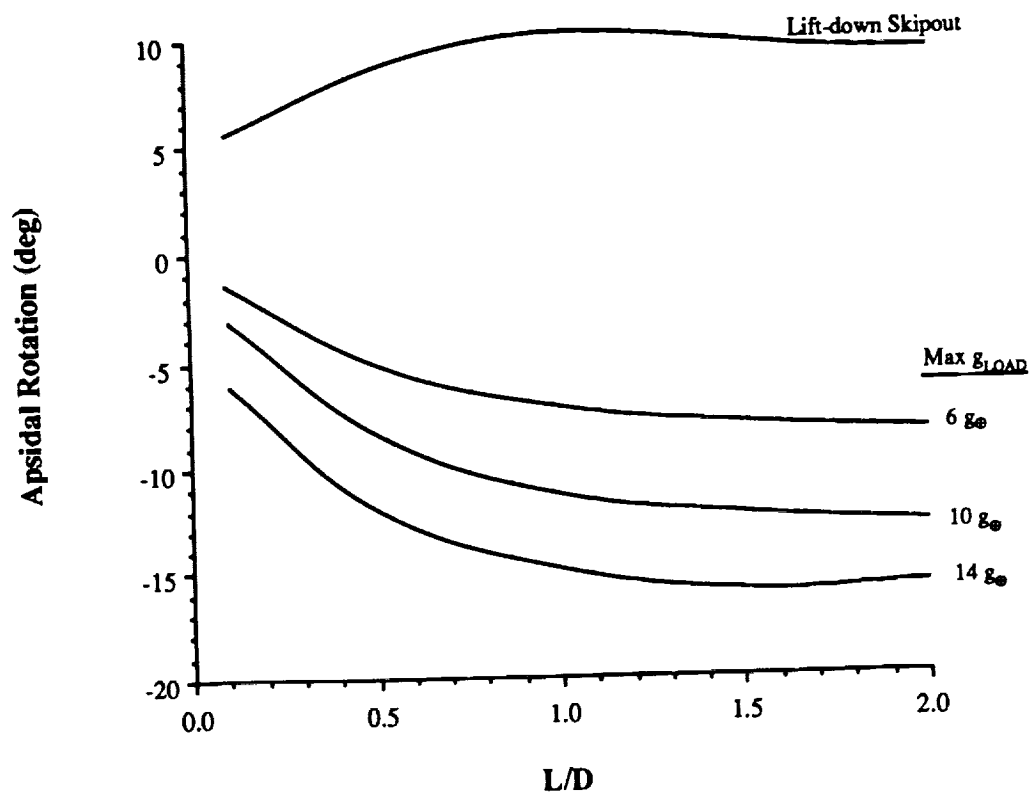


Figure B-13. Mars: Apsidal rotation for  $V_\infty = 10$  km/s.

## APPENDIX C

### EFFECT OF VEHICLE BALLISTIC COEFFICIENT ON AEROCAPTURE CORRIDOR WIDTH

The vehicle model used in this study consisted of two parameters, the lift-to-drag ratio ( $L/D$ ) and ballistic coefficient ( $C_B$ ), both assumed to be constant. While  $L/D$  was varied parametrically, a specific ballistic coefficient was computed for each value based on historical or proposed spacecraft data. Since the  $C_B$  of a vehicle design with a given  $L/D$  can vary over a wide range, especially due to differences in design mass, it is of interest to discuss what effect variations in the  $C_B$  values used in this study have on the corridor width data presented.

In order to illustrate the impact of  $C_B$  on corridor width, a specific case is examined. Figure C-1 is the corridor width plot for aerocapture into Earth for  $V_\infty = 7.56$  km/s. Superimposed on the corridor width curves for the nominal  $C_B$  values are the corresponding curves for vehicles with  $C_B$ 's which are half and double the nominal values. It is immediately apparent that the impact of this parameter on corridor width is very small (the largest variation seen from the nominal case is approximately 5 km). This indicates that vehicle  $L/D$  is the principle vehicle parameter influencing aerocapture corridor width, with  $C_B$  having a second-order effect. While the impact on corridor width is small, the vertical location of the corridor in the atmosphere is significantly shifted. This can be explained by the fact that the corridor is mostly a function of vehicle deceleration. In the case of the vehicle with the reduced  $C_B$ , the drag on the vehicle is larger than the nominal case and, therefore, the vehicle experiences higher deceleration and slows down more quickly and at higher altitudes. The resulting corridor is therefore shifted higher in the atmosphere than the nominal case. Likewise, the vehicle with a higher  $C_B$  experiences lower drag than the nominal case, thereby causing it to penetrate to lower altitudes. The resulting corridor is lower in the atmosphere than the nominal corridor.

While  $C_B$  has only a second-order effect on the entry corridor width, it has a major impact on the aerodynamic heating experienced by the vehicle. This is due to the fact that heating is strongly a function of the velocity and atmospheric density. Since the vehicle with higher  $C_B$  decelerates less quickly and penetrates deeper into the atmosphere, it will experience higher density and, therefore, higher heating than the lower  $C_B$  vehicle. Thus, while a specific vehicle design  $L/D$  may provide adequate corridor width to support aerocapture, the  $C_B$  may be too large depending on the constraints on heating.

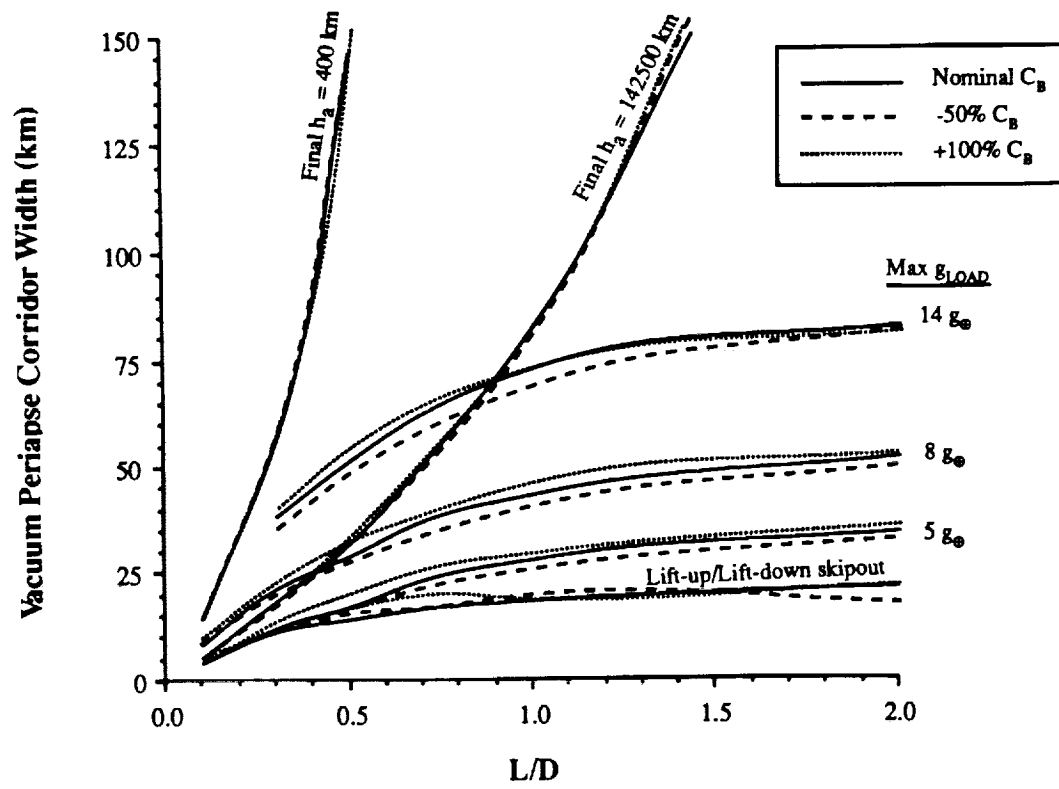


Figure C-1. Earth: Ballistic coefficient sensitivity with  $V_\infty = 7.56\ km/s$ .

## APPENDIX D

### G-LIMITS FOR ZERO CORRIDOR WIDTHS

For an aerobraking vehicle with a given  $L/D$  and  $V_\infty$ , it can be seen in the plots given in section 3 that the entry corridor will be reduced as the g-limit is lowered. The g-limit can be lowered to a point where the corridor width closes down to zero. At zero corridor width, the vehicle would be required to fly with perfect knowledge of the atmosphere, aerodynamics, and navigation, with no margins left for any dispersion. This vehicle design, in terms of  $L/D$ ,  $V_\infty$ , and g-limit, defines the very edge of acceptable conditions. Therefore, for the given vehicle to have a greater-than-zero corridor width, its maximum allowable g-load must be greater than the g-limit for the zero corridor width.

The g-limit at zero corridor width defines the minimum g-limit for a given vehicle. This minimum g-limit is the g-limit obtained at the upper/shallow corridor boundary at full lift-down. It was mentioned in section 2.2 that the lift-up/lift-down skipout line defines the minimum allowable g-load level for successful aerocaptures at full lift-up till peak loading. That is, g-loads less than this value are not adequate for the lift-up/max g-load side of the corridor width, since these trajectories would skip out. However, this is not the absolute minimum g-limit for zero corridor width, since a lift-down/shallow trajectory will pull a lower g-load and still achieve exit energy requirements. Therefore, to have zero corridor width the appropriate minimum g-load to choose is the lift-down shallow g-load value.

The g-limits for zero corridor widths are given in figures D-1 to D-6 for Earth aerocapture and in figures D-7 to D-11 for Mars aerocapture. The curves drawn on these plots are simple interpolations of the data points. It can be seen in several of the plots (i.e., figs. D-1 and D-2) that the curves are not "smooth." This is due to the fact that all corridor boundaries in this study were found to the nearest kilometer in approach periapse altitude. The maximum g-load is very sensitive to the approach periapse altitude for full lift-down trajectories. Therefore, the curves would become smooth if the corridor boundaries were found with higher accuracy in the approach periapse altitude. For example, figure D-9 for Mars aerocapture at  $V_\infty = 6.97$  km/s shows a "hill" for 1.0 to 2.0  $L/D$ . At 1.0  $L/D$ , the maximum g-load was 1.42 g at an approach periapse altitude of 50 km. If the approach periapse altitude were found with a higher accuracy to be 49.13 km (a difference of only 0.87 km), the maximum g-load would increase to 1.86 g. Using a 1.86 g for an  $L/D$  of 1.0 would then smooth out the curve in figure D-9. Therefore, in utilizing the figures given in this section, it is important to keep in mind that the data were found only to the nearest kilometer in approach periapse altitude.

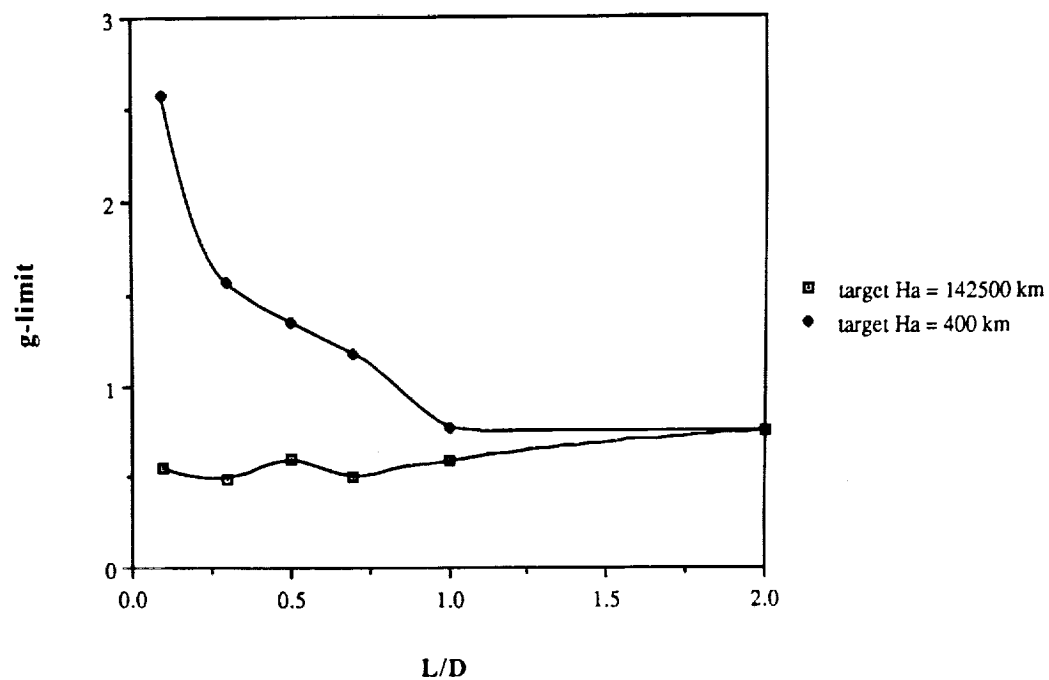


Figure D-1. Earth: g-limits for 0° corridors at  $V_\infty = 1$  km/s.

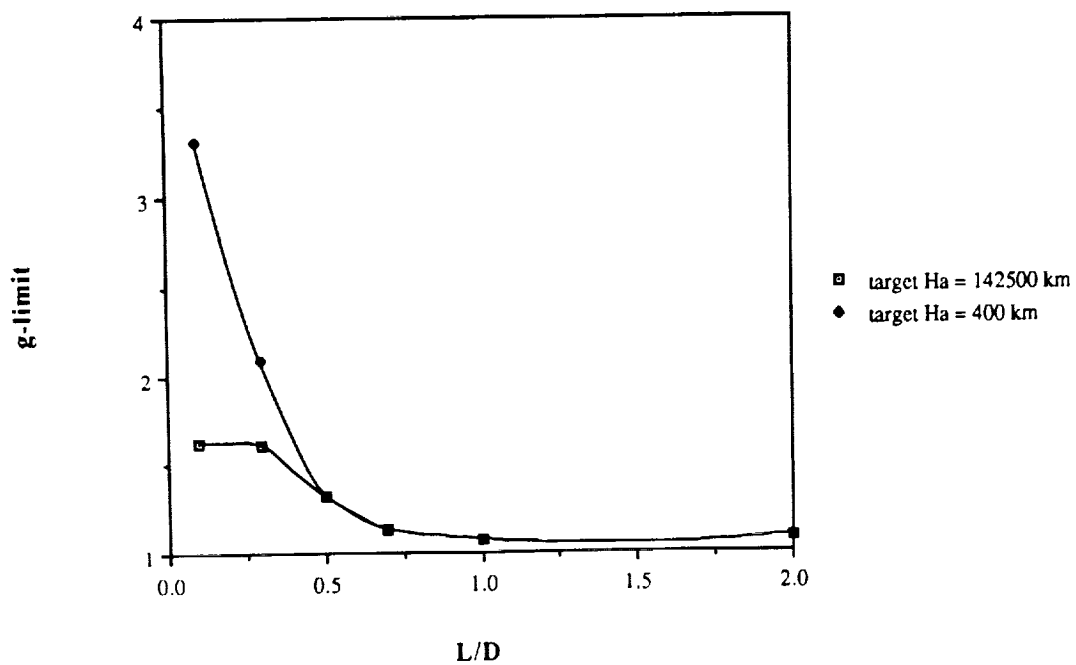


Figure D-2. Earth: g-limits for 0° corridors at  $V_\infty = 4$  km/s.



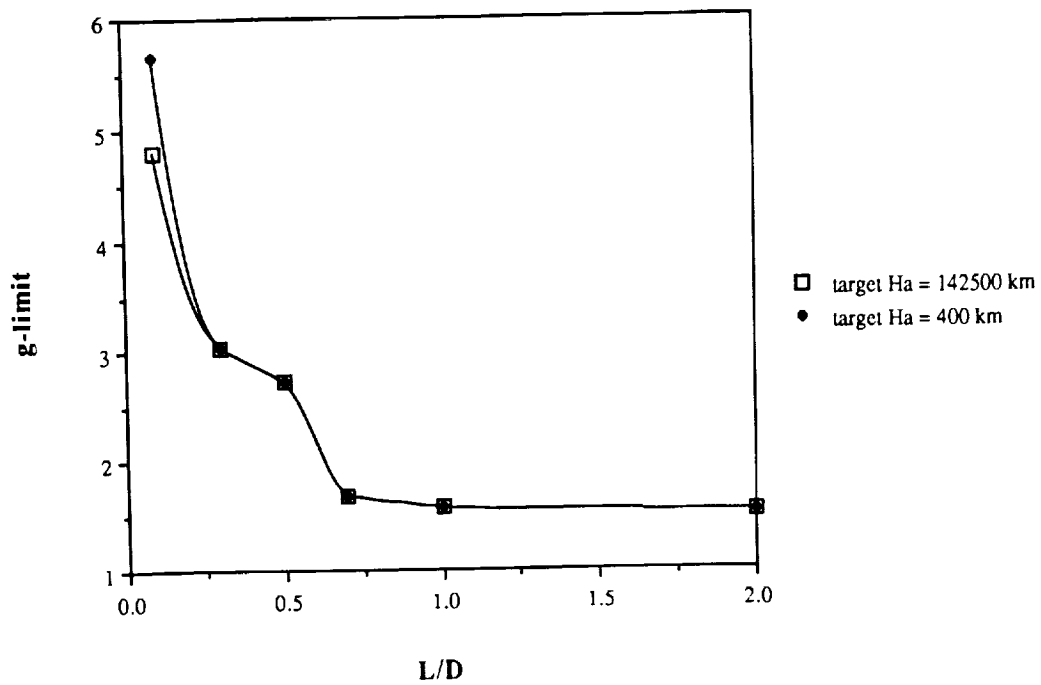


Figure D-3. Earth: g-limits for  $0^\circ$  corridors at  $V_{\infty} = 7.56$  km/s.

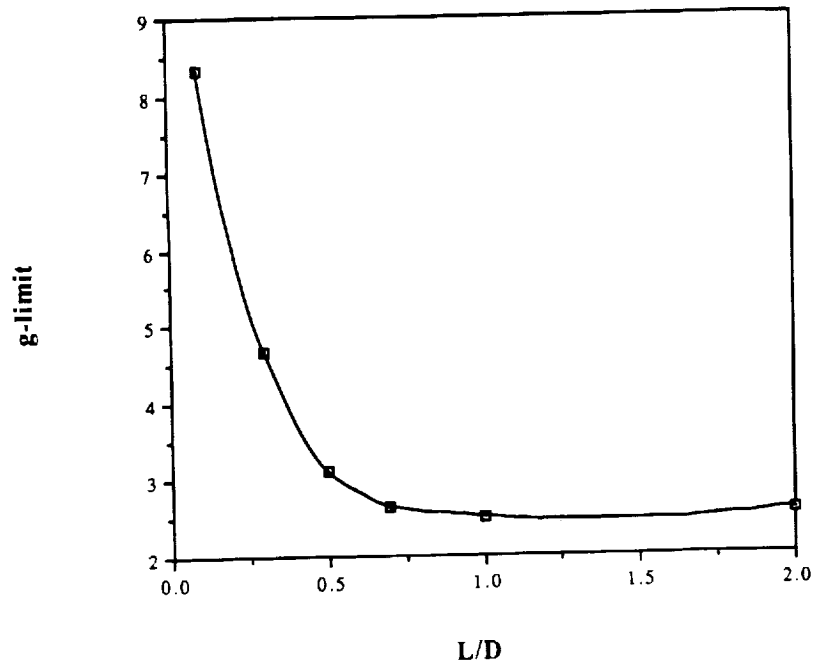


Figure D-4. Earth: g-limits for  $0^\circ$  corridors at  $V_{\infty} = 10.61$  km/s.

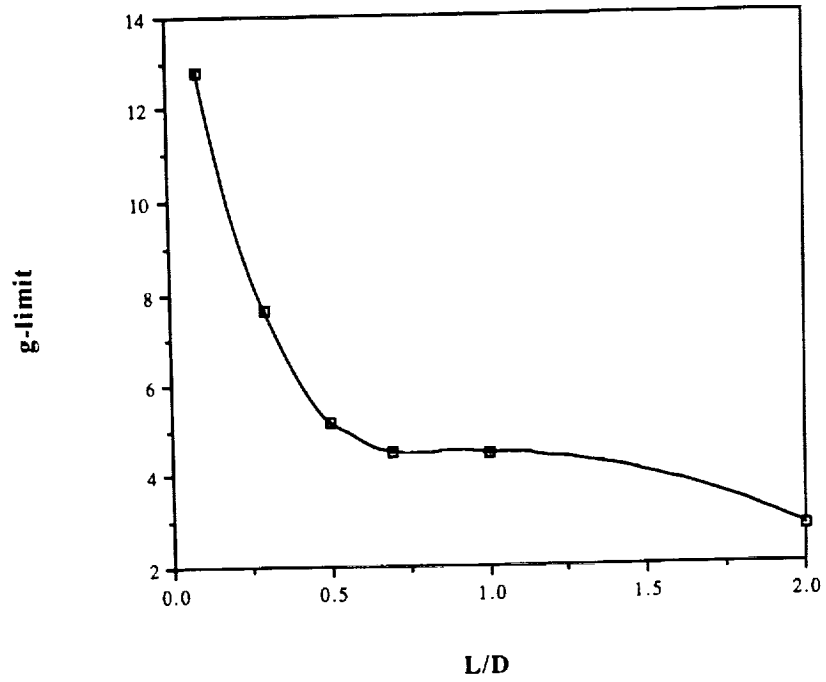


Figure D-5. Earth: g-limits for  $0^{\circ}$  corridors at  $V_{\infty} = 14$  km/s.

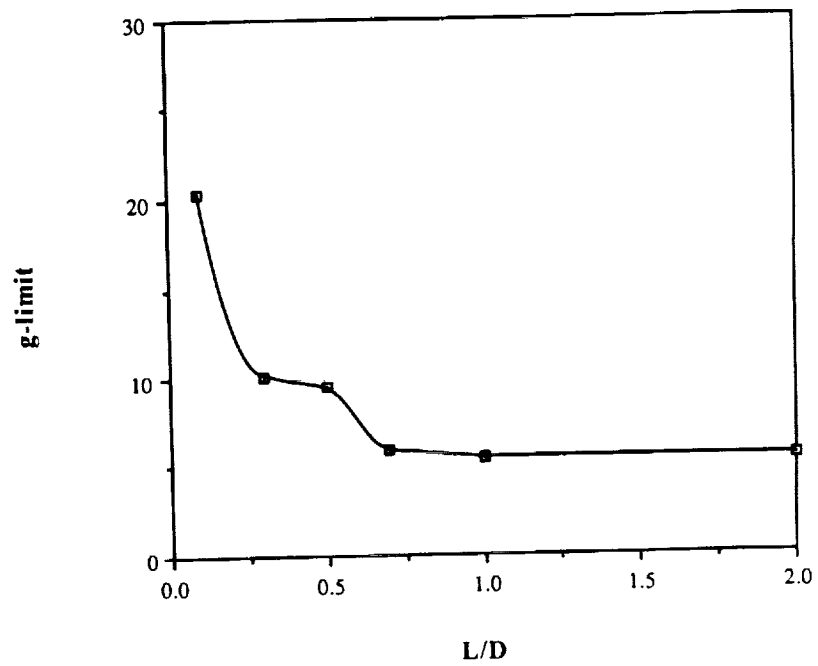


Figure D-6. Earth: g-limits for  $0^{\circ}$  corridors at  $V_{\infty} = 18$  km/s.

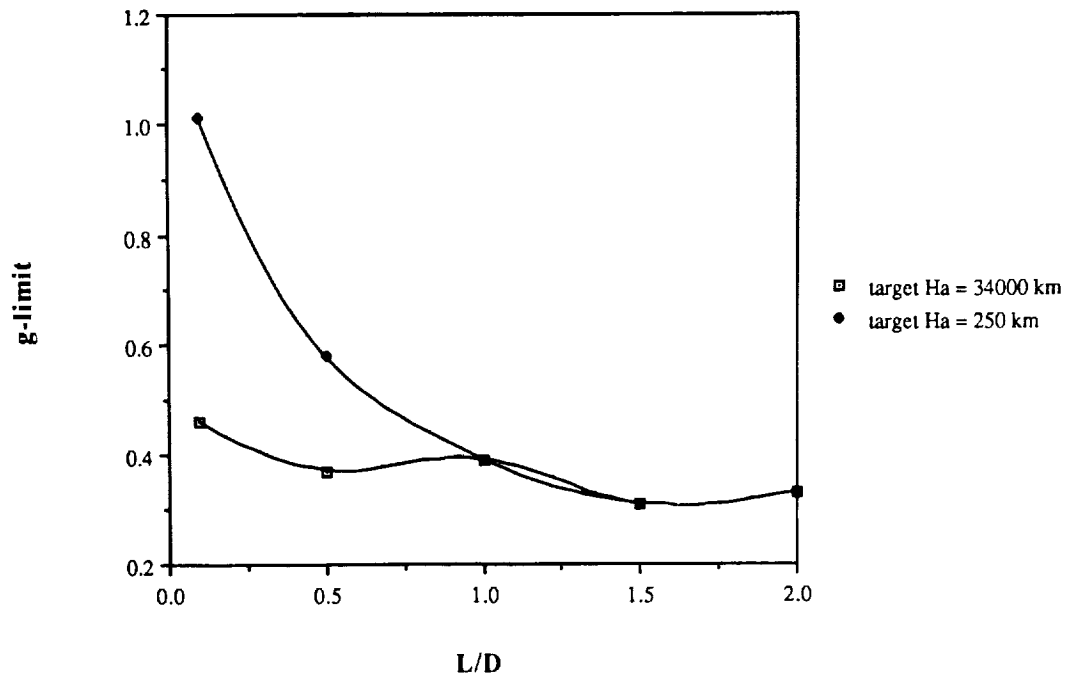


Figure D-7. Mars: g-limits for  $0^\circ$  corridors at  $V_\infty = 2$  km/s.

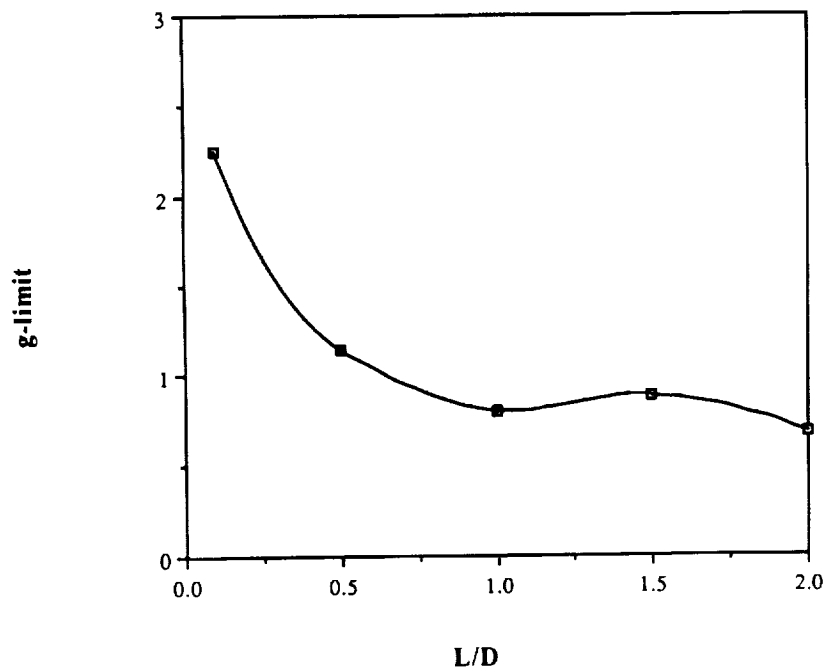


Figure D-8. Mars: g-limits for  $0^\circ$  corridors at  $V_\infty = 4.71$  km/s.

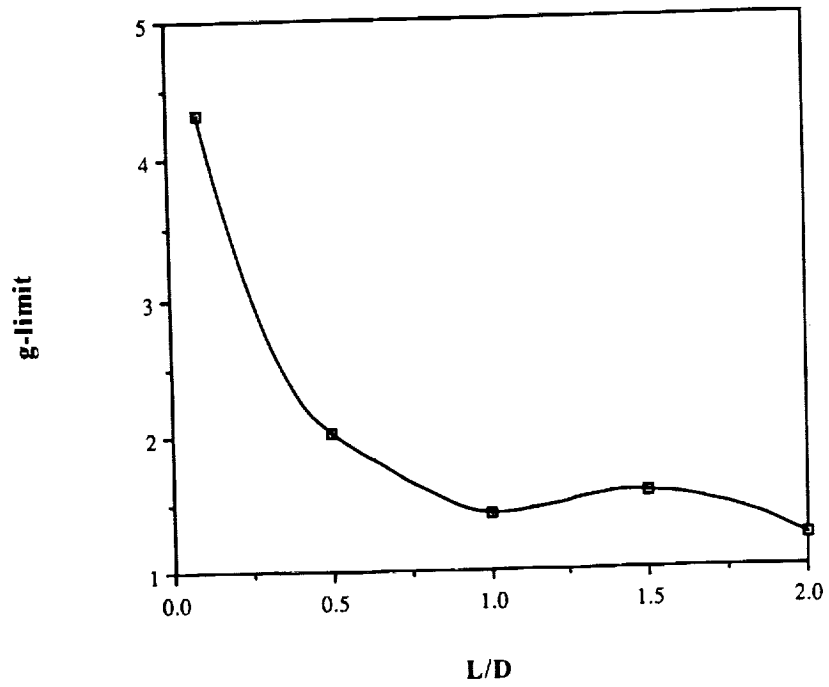


Figure D-9. Mars: g-limits for  $0^\circ$  corridors at  $V_\infty = 6.97$  km/s.

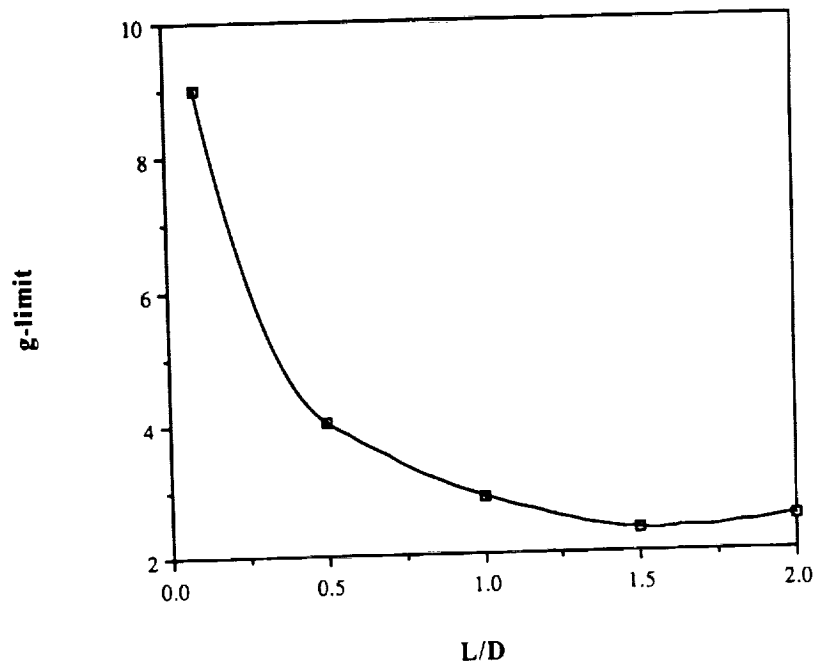


Figure D-10. Mars: g-limits for  $0^\circ$  corridors at  $V_\infty = 10$  km/s.

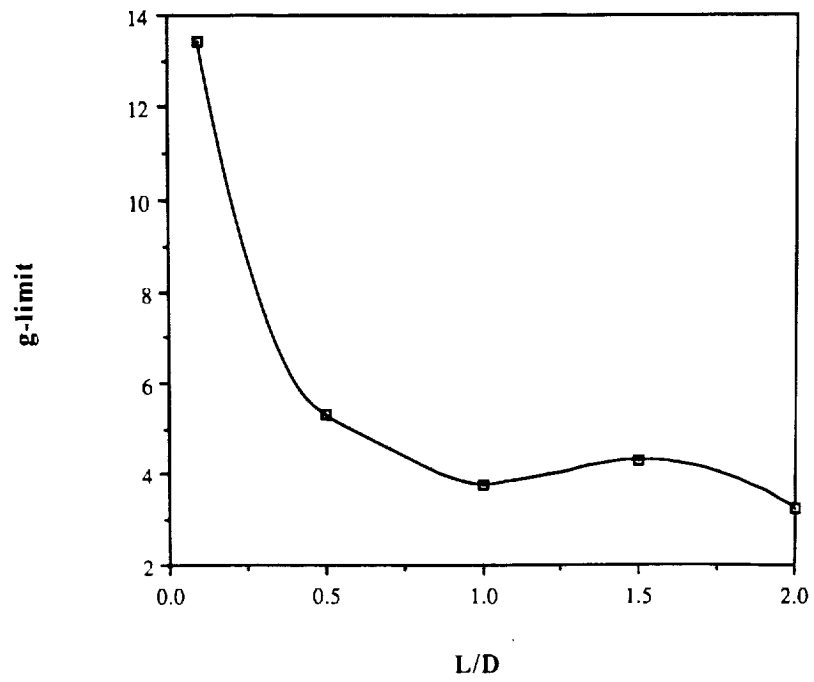


Figure D-11. Mars: g-limits for  $0^\circ$  corridors at  $V_\infty = 12$  km/s.





National Aeronautics and  
Space Administration

## REPORT DOCUMENTATION PAGE

1. Report No. TM102178		2. Government Accession No.		3. Recipient's Catalog No.	
4. Title and Subtitle  Parametric Entry Corridors for Lunar/Mars Aerocapture Missions				5. Report Date January 22, 1991	
				6. Performing Organization Code ET4	
7. Author(s) Lisa M. Ling Franco M. Baseggio * Douglas P. Fuhry *				8. Performing Organization Report No. S-628	
9. Performing Organization Name and Address  NASA/Johnson Space Center ET4/Performance Analysis Branch Houston, TX 77058				10. Work Unit No.	
				11. Contract or Grant No.	
12. Sponsoring Agency Name and Address  NASA/Johnson Space Center ET4/Performance Analysis Branch Houston, TX 77058				13. Type of Report and Period Covered Technical Memorandum	
				14. Sponsoring Agency Code	
15. Supplementary Notes  * Charles Stark Draper Laboratory, Inc.					
16. Abstract This report presents parametric atmospheric entry corridor data for Earth and Mars aerocapture. Parameter ranges for this study were dictated by the range of mission designs currently envisioned as possibilities for the Human Exploration Initiative (HEI). This data, while not providing a means for exhaustive evaluation of aerocapture performance, should prove to be a useful aid for preliminary mission design and evaluation. Entry corridors are expressed as ranges of allowable vacuum periape altitude of the planetary approach hyperbolic orbit, with charts provided for conversion to an approximate flight path angle corridor at entry interface (EI, 125 km altitude). The corridor boundaries are defined by open-loop aerocapture trajectories which satisfy boundary constraints while utilizing the full aerodynamic control capability of the vehicle (i.e., full lift-up or full lift-down). Parameters examined were limited to those of greatest importance from an aerocapture trajectory performance standpoint, including the approach orbit hyperbolic excess velocity ( $V_{\infty}$ ), the vehicle lift-to-drag ratio (L/D), maximum aerodynamic load factor limit, and the apoapse of the target orbit. The impacts of atmospheric density bias uncertainties are also included.  The corridor data is presented in graphical format, and examples of the utilization of these graphs for mission design and evaluation are included.					
17. Key Words (Suggested by Author(s)) Aerobrake Aerocapture Corridor Lunar/Mars			18. Distribution Statement Unlimited - Unclassified Subject Category - 12		
19. Security Classification (of this report)  Unclassified		20. Security Classification (of this page)  Unclassified		22. Price	

For sale by the National Technical Information Service Springfield VA 22161-2171

